

Design of actively controllable two-dimensional phononic waveguides  
based on valley topological phononic band engineering

September 2023

**Md. Shuzon Ali**

Graduate School of  
Natural Science and Technology  
(Doctor's Course)

OKAYAMA UNIVERSITY, JAPAN



# DOCTORAL THESIS

---

Design of actively controllable two-dimensional phononic waveguides  
based on valley topological phononic band engineering

---

Author:

Md. Shuzon Ali

Supervisor:

Prof. Kenji Tsuruta

Co-Supervisor:

Prof. Yasuyuki Nogami

Associate Prof. Kazuhiro Fujimori

*A dissertation submitted to*

*Okayama University*

*In fulfilment of the requirements for the degree of*

*Doctor of Philosophy in Engineering*

*in the*

*Graduate School of Natural Science and Technology*

*August 28, 2023*

TO WHOM IT MAY CONCERN

---

We hereby certify that this is a typical copy of the original Doctoral  
dissertation of

Md. Shuzon Ali

Student ID:51502754

Thesis Title:

Design of actively controllable two-dimensional phononic waveguides  
based on valley topological phononic band engineering

---

Seal of Supervisor

Official Seal

Professor Kenji Tsuruta

Graduate School of

Natural Science and Technology

---

## **Declaration of Authorship**

This dissertation and the work presented here for doctoral studies were conducted under the supervision of Professor Kenji TSURUTA. I, Md. Shuzon Ali, declare that this thesis title, “Design of actively controllable two-dimensional phononic waveguides based on valley topological phononic band engineering” and the work presented in it are my own. I confirm that:

Signed: Md. Shuzon Ali

Student number: 51502754

---

Date: August 28, 2023

---

# Abstract

Md. Shuzon Ali

Design of actively controllable two-dimensional phononic waveguides based on valley topological phononic band engineering

Phononic crystals are defined as having an artificial periodic structure, and the essential features of the dispersion properties can be described by the "phononic band" of the structure. The present outcomes have been achieved by taking advantage of topological protection in certain phononic bands. The topologically protected eigenmodes can be identified by finding topological phase transitions in their dispersion [1] during the rotation of the unit-cell structure with  $C_{3v}$  symmetry. Also, the Berry curvature has been found to be important in explaining the topological phase transition of the band in the unit cell. Acoustic waveguides based on phononic crystals [2-11] have been attracting increasing attention for controlling wave transmission along designed paths at desired operating frequencies [12-15] using a band-engineering scheme similar to the electronic structure design in semiconductors.

For real-world device applications, however, acoustic waveguides are necessary to be more efficient and robust against defects and bending. Besides, the waveguide structure must be reconfigurable considering the active control of its functionality to use a topological waveguide in an integrated device. Some examples of such a reconfigurable structure for topological photonic waveguides can be found in recent literature. Zhang et al. demonstrated topologically protected sound propagation in a reconfigurable manner by rotating three-legged unit cells without altering their lattice structure [16]. This study adopted the mechanical rotation of the unit cell orientation. However, this report required specific mechanisms for the reconfiguration of waveguide structures without losing their robustness.

The objective of this thesis is to design a topological acoustic waveguide aimed at the development of highly integrated switchable acoustic devices. The first approach is to propose a method to achieve reconfigurability. In the approach, we adopted a unit cell composed of a circular rod in a  $C_{3v}$  symmetric structure embedded in water. By shifting one rod in all layers below an interface to construct an oppositely oriented rod array in

the lower layer using continuous translation [17], while the properties are theoretically determined by pressure acoustic frequency analyses. The topological phase transition in this construction is monitored through the Berry curvature. Such an approach toward dynamical adjustability and reconfigurability is highly desired for integrated switchable acoustic devices. We constructed the reconfigurable supercell as well as the waveguide to compare the phase transition and transmission properties with those of other waveguides. We observed efficient (85%) transmission along the path of the reconfigurable waveguide interface [17, 18].

On the other hand, in many situations, however, the consideration of loss, termed a non-Hermite system, can be in line with the energy dissipation in the real world. Recently, the artificial arrangement of gain and loss in a system represents a unique class of non-Hermite system, also known as the parity-time symmetric system, and is proven to hold unique phenomena such as an exceptional point, where two or more eigenstates emerge in the real part of frequency while they start to diverge in the imaginary part, as well as an induced unidirectional wave propagation [19]. In a topological waveguide, the transmission of an acoustic waveguide was approximately 5% lower than that of a straight waveguide [20]. Most of the previous efforts to improve transmission efficiency have been devoted to finding ways to reduce material and/or structural losses effectively in waveguides. In the present study, we propose the opposite. By increasing the losses rather extremely, we demonstrated that propagation losses mainly due to localized modes can be effectively avoided [21]. We prepared a two-dimensional hexagonal lattice composed of three air-filled circular holes in polydimethylsiloxane, wherein localized modes appeared within the phononic band gaps; these modes coupled with the propagating modes (edge modes) that emerged at the interface between neighboring crystalline phases with different band topologies. As the non-Hermiticity parameter ( $\gamma$ ) is introduced to modify the phononic band structures, its imaginary parts also emerge, thus leading to possible control of the propagation losses appearing due to the coupling between the propagating and the lossy localized modes. Our present research demonstrates a simple method for designing a topological acoustic waveguide aimed at a switchable wave transmission device based on large variations of the non-Hermiticity parameter.

## **Declaration of Originality**

The work presented in this thesis was performed under the supervision of Prof. Dr. Kenji Tsuruta in the Department of Electrical and Electronic Engineering at Okayama University, Japan. I declare that the work presented in the thesis is my own, except where specific references are made.

## **Acknowledgements**

First, I would like to express my gratitude and thanks to the most merciful almighty Allah for giving me the strength, knowledge, patience, and ability to complete my PhD thesis successfully.

During my thesis work, I have been lucky enough to have the cooperation of many people from whom I have learned many things. I want to express my full acknowledgement to them for their valuable advice, cordial support, and so on.

I would like to express my deepest gratitude to my esteemed supervisor, Professor Kenji Tsuruta, Department of Electrical and Electronic Engineering, Okayama University, Japan, for his continuous support, constant inspiration, scholastic guidance, cordial behavior, motivation, invaluable suggestions, feedback, and patience during the whole period of my PhD research work. His immense knowledge and plentiful experience have encouraged me throughout my academic research and have had a significant impact on my daily life. I am grateful to his intellectual and potential supervision. Actually, I am grateful to my respected supervisor for giving me the opportunity to work in the Multiscale Device Design Tsuruta Laboratory. I could not have imagined having a better supervisor and mentor for my PhD study.

I would like to thank Assistant Professor Masaaki Misawa (former), Department of Electrical and Electronic Engineering, Okayama University, Japan, for providing me with all kinds of departmental support during my thesis period.

I am extremely grateful to my doctoral course Co-supervisors, Professor Yasuyuke Nogami, and Associate Professor Kazuhiro Fujimori, for their valuable time to read my research work during my PhD thesis period.

I would like to thank JST (Japan Science and Technology) for their moral support on my successful application to Monbukagakusho (MEXT) through the Sakura Science Exchange (SSC) program. Thanks to MEXT, Japan, for the scholarship that fulfilled my dream to pursue doctoral study in Japan. I sincerely acknowledge all the funds that



allowed me to join several national and international conferences and conduct research activities.

I am also grateful to all administrative officers of the Faculty of Engineering who directly or indirectly made an impact on my doctoral course studies. I would like to thank all of my lab mates and friends in the laboratory for creating a great work atmosphere and for their generous support. Thanks to the pairing team members in my lab who are some of the brightest minds I've worked with. Also, I would like to thank **JSPS** (the Japan Society for the Promotion of Science) as part of KAKENHI Grant Numbers 21H05020 and 21K18877 for their financial support that also provided me with complete academic freedom in this research.

At last, I wish to express gratitude to my parents, my wife (her sacrifices and cordial supports), and other members of my family for their inspiration, trust, and support that enabled me to pursue this PhD study.

**September 2023**

**The Author**

<b>Contents</b>	<b>Page No.</b>
<b>Declaration of Authorship</b>	<b>iv</b>
<b>Abstract</b>	<b>v</b>
<b>Declaration of Originality</b>	<b>vi</b>
<b>Acknowledgements</b>	<b>vii-viii</b>
<b>Contents</b>	<b>x-xii</b>
<b>List of Figures</b>	<b>xiii-xvii</b>
<b>List of Tables</b>	<b>xviii</b>
<b>Nomenclature</b>	<b>xix</b>
<b>Research Activities</b>	
<b>1. Introduction</b>	<b>01-18</b>
1.1 Introduction	01-05
1.2 Crystal Structure	05-06
1.3 Photonic Crystal, and Phononic Crystal	06-07
1.4 Crystal Lattice, and Reciprocal Lattice	07-08
1.5 Unit Cell, Super Cell	08-10
1.6 Brillouin Zone, and Irreducible Brillouin Zone	10-12
1.7 Bloch's Theorem, Band Gap, and Dispersion Relation	13-14
1.8 Berry Phase, Berry Connection, and Berry Curvature	15-18
<b>2. Modeling and Characterization</b>	<b>19-27</b>
2.1 Introduction	19-20
2.2 Model Equations	20-21
2.3 Phononic Band Analysis	21-25
2.4 Topological Phase Transition via Application of Berry Curvature	25-27

### **3. Theoretical Approach for Topological Phononic $C_{3v}$ Symmetric Supercell and Reconfigurable Waveguide Design** **28-50**

3.1 Introduction	28-29
3.2 Symmetry, and Different Type of Symmetry	29-30
3.3 Topological Phononic Waveguide, and Reconfigurable Waveguide	30-31
3.4 Transmission Coefficient, and Transmission Loss	31-32
3.5 Translational Shift of Rod Array for Symmetry Transformation	32-33
3.6 Interface Band Properties of Supercell	33-38
3.7 Transmission Properties of Topological Waveguide	38-42
3.8 Straight Waveguide	42-43
3.9 Reconfigurable Straight Waveguide	43-44
3.10 Transformation to $C_{2v}$ Symmetric Interface	44-45
3.11 Z- Shaped Waveguide	46-49
3.12 Z- Shaped Reconfigurable Waveguide	49-50

### **4. Active Control of Localized Mode and Transmission in Valley Z-Shaped Topological Phononic Waveguides by Non-Hermitian Modulation**

**51-68**

4.1 Introduction	51-52
4.2 Hermitian System, and Non-Hermitian System	52-54
4.3 Parity-Time (PT), and Symmetric, and Exponential Point (EP)	54
4.4 Evanescent Wave	54-55
4.5 Dispersion Relation and Topological Transition	55-57
4.6 Extinction of Lossy Localized States in Unit Cell	57-59
4.7 Extinction of Lossy Localized States in Interface Supercell	60-61
4.8 Switching On/Off of Loss Effects on Z-Shaped Waveguides	61-62
4.9 Transmission of Z-Shaped Waveguides	63

4.10 Evanescent Wave Transmission	64
4.10.1 Uniform Waveguide	64-65
4.10.2 Straight Waveguide	65-67
4.10.3 Z-Shaped Waveguide	68
<b>5. Conclusions and Future Work</b>	<b>69-71</b>
<b>References</b>	<b>72-82</b>
<b>Biography</b>	<b>83</b>

## List of Figures

Serial No.	Figure Description	Page No.
01	<b>Fig.(i):</b> The crystal structure is formed by the addition of the basis (b) to every lattice point of the space lattice (a). By looking at (c), one can recognize the basis and then one can abstract the space lattice.	6
02	<b>Fig.(ii):</b> The crystal structure with translational vectors.	7
03	<b>Fig.(iii):</b> (a) Unit cell of the two-dimensional phononic crystal, and (b) Primitive unit cell.	9
04	<b>Fig.(iv):</b> Supercell with differently oriented unit cell $\alpha = 30^\circ$ and $\alpha = -30^\circ$ layers have defined to distinguish by a topological interface ( <b>Adopted from M.S. Ali et al. Jpn. J. Appl. Phys, 2023</b> ).	10
05	<b>Fig.(v):</b> The first Brillouin zone for a two-dimensional square lattice.	11
06	<b>Fig.(vi):</b> The first irreducible Brillouin zone for the periodic composites with (a) square lattice: $\Gamma(kx, ky) = (0,0)$ , $X(kx, ky) = \left(\frac{\pi}{a}, 0\right)$ , and $M(kx, ky) = \left(\frac{\pi}{a}, \frac{\pi}{a}\right)$ , and (b) hexagonal lattice: $\Gamma(kx, ky) = (0,0)$ , $K(kx, ky) = \left(\frac{4\pi}{3a}, 0\right)$ , and $M(kx, ky) = \left(\frac{\pi}{a}, \frac{\pi}{\sqrt{3}a}\right)$ .	12
07	<b>Fig.(vii):</b> The parametric position of $\vec{R}(t)$ along a path.	15
08	<b>Fig.(viii):</b> Two dimensional (2D) Hexagonal structure.	21
09	<b>Fig.1:</b> (a) Hexagonal unit cell with $C_{3v}$ symmetry, and band structures (b) for the unit cell with $\alpha = 30^\circ$ , (c) for the unit cell with partially shifted rod, (d) for the unit cell with intermediate shift, and (e) for the unit cell with $\alpha = -30^\circ$ .	22-24

10	<b>Fig.2:</b> Berry curvatures of the lower and upper bands in the reciprocal space near the K+ and K- valleys (a) for the unit cell with $\alpha = 30^\circ$ , (b) for the unit cell with partially shifted rod array, (c) for the unit cell with intermediate shift, (d) for the unit cell with $\alpha = -30^\circ$ . Insets show pressure fields (color) and acoustic-intensity distributions (arrow) of the mode at K+ and K- points, and (e) Hexagonal Brillouin zone, where the arrow line (highlighted by red color) represents the direction of the path of K- to K+ points.	25-27
11	<b>Fig.3:</b> Schematic arrangement of reconfigurable structure from a uniform crystal $C_{3v}$ symmetry structure.	31
12	<b>Fig.4:</b> Transmission efficiency of reconfigurable structure from a crystal $C_{3v}$ symmetry structure.	32
13	<b>Fig.5:</b> (a) Schematic of continuous translation of a rod array in a single phononic crystal, and (b) waveguide structure constructed after the transformation illustrated in (a) ( <b>Adopted from M.S. Ali et al. Jpn. J. Appl. Phys, 2023</b> ).	33
14	<b>Fig.6:</b> (a) Supercell structure and band diagrams of (a) a valley PnC with $\alpha = 30^\circ$ and $\alpha = -30^\circ$ , (b) a PnC of uniform $C_{3v}$ unit cells with $\alpha = 30^\circ$ , (c) supercell structure with partially shifted unit cells, (d) supercell with an interface between $\alpha = 30^\circ$ and $\alpha = -30^\circ$ reconfigured from the structure in (b) leaving a dimer array, (e) a PnC of uniform $C_{3v}$ unit cells with $\alpha = 30^\circ$ with dimer array inserted, and (f) supercell with an interface between two oppositely oriented ( $\alpha = 30^\circ$ and $-30^\circ$ ) $C_{2v}$ unit cells (generated by vertical shift with 0.3 mm) ( <b>Adopted from M.S. Ali et al. Jpn. J. Appl. Phys, 2023</b> ).	35-37

15	<b>Fig.7:</b> (a-b)) Normalized pressure field and transmission in valley phononic straight waveguide, (c-d) Normalized pressure field at 400 kHz and transmission for a uniform phononic waveguide, (e-f) Normalized pressure field at 370 kHz and transmission for a $C_{2v}$ breaking symmetric (partial translation) waveguide, (g-h) Normalized pressure field at 400 kHz and transmission in reconfigurable phononic waveguide, and (i-j) Normalized pressure field at 400 kHz and transmission for a uniform structure waveguide due to localized mode effect(Adopted from M.S. Ali et al. Jpn. J. Appl. Phys, 2023).	38-42
16	<b>Fig.8:</b> (a) Normalized pressure field at 400 kHz, and (b) transmission for broken $C_{2v}$ symmetry (when $\alpha = 30^\circ$ and $\alpha = -30^\circ$ ) waveguide (Adopted from M.S. Ali et al. Jpn. J. Appl. Phys, 2023).	45
17	<b>Fig.9:</b> (a) Normalized pressure fields in a valley phononic Z-shape waveguide (WG), (b) transmission spectrum in valley phononic Z-shaped, (c-d) Normalized pressure fields and transmission spectrum in uniform phononic crystal WG at 400 kHz, and (e-f) Normalized pressure fields and transmission spectrum for partially translation of rod waveguide, and (g-h) Normalized pressure fields and transmission spectrum in reconfigured Z-shaped WG (Adopted from M.S. Ali et al. Jpn. J. Appl. Phys, 2023).	47-49
18	<b>Fig.10:</b> (a) Hexagonal unit cell at the orientation $\alpha = 30^\circ$ . Phononic band gap for Hermitian system at the orientations (b) $\alpha = -30^\circ$ , (c) $\alpha = 30^\circ$ , (d) $\alpha = 0^\circ$ . The pressure field distributoins indicated by the red arrows show propagating dispersive modes at 435.32 kHz, and 551.09 kHz, respectively, and those indicated by black arrows depict localized modes at 476.5 kHz, 494.42 kHz, and 505.25 kHz,	56-57

	respectively, and (e) the Berry correction and integration of path for the valley Chern index ( <b>Adopted from M.S. Ali et al. Applied Physics Express, 2023</b> ).	
<b>19</b>	<b>Fig.11:</b> (a) The variation of the real eigenfrequency as a function of $\gamma$ , where the localized mode highlighted by black color, (b) The pressure field of three symmetric localized mode (when $\gamma = +1$ ) with complex eigenfrequency 476.77+476.62i kHz, and 477.16+477.06i kHz, and 477.31+477.21i kHz, respectively, (c) the acoustic pressure intensity via the non-Hermitian modulation, (d) the corresponding pressure field of (c) with complex eigenfrequency that indicating the localized mode appears near the holes, (e) localized mode disappears for $\gamma = 5$ , and (f-g) the localized mode appears in the bulk band gap frequency through unit cell when non-Hermitian lossy $\gamma = 2$ , and (h-i) the localized mode disappears in the bulk band gap frequency through unit cell when non-Hermitian lossy $\gamma = 10$ ( <b>Adopted from M.S. Ali et al. Applied Physics Express, 2023</b> ).	<b>58-59</b>
<b>20</b>	<b>Fig.12:</b> The pressure field distributions and the valley interface band diagrams of $C_{3v}$ symmetric supercell structure with different orientations ( $\alpha = 30^\circ$ and $\alpha = -30^\circ$ ) of the unit-cell layers for (a) Hermitian and (b) non-Hermitian lossy systems, respectively ( <b>Adopted from M.S. Ali et al. Applied Physics Express, 2023</b> ).	<b>61</b>
<b>21</b>	<b>Fig.13:</b> Normalized total acoustic pressure in a Z-shaped waveguide interface at 476 kHz in (a) Hermitian ( $\gamma = 0$ ) and non-Hermitian lossy systems with (b) $\gamma = 2$ and (c) $\gamma = 10$ . (d) Pressure distribution (enlarge) of the Z-shaped waveguide depicted in (b) and (c). (White circles in (b) and	<b>62</b>



	(c) highlight the positions of the circular holes depicted in (d)) (Adopted from M.S. Ali et al. <b>Applied Physics Express</b> , 2023).	
<b>22</b>	<b>Fig.14:</b> The transmission spectrum of the Z-shaped waveguide interface in Fig.13(a-c) (the lower graph) and its magnified view (the upper graph) in the vicinity of the localized mode frequency (476kHz) indicated by the dashed vertical black line (Adopted from M.S. Ali et al. <b>Applied Physics Express</b> , 2023).	<b>63</b>
<b>23</b>	<b>Fig.15:</b> The normalized total acoustic pressure in a uniform waveguide at 476 kHz (a) Hermitian regime, when $\gamma = 0$ , and non-Hermitian regime (b) when $\gamma = 10$ , (c) when $\gamma = 50$ , and (d) when $\gamma = 100$ , respectively.	<b>65</b>
<b>24</b>	<b>Fig.16:</b> The normalized total acoustic pressure in a valley straight phononic waveguide with differently oriented $C_{3v}$ symmetry unit cell $\alpha = 30^\circ$ and $\alpha = -30^\circ$ respectively, and separated by an interface (the dashed horizontal line highlighted by yellow color) (a) in Hermitian system. Comparisons of the normalized total acoustic pressure in non-Hermitian system with $\gamma = 0.5, 50$ , and $100$ respectively, (b-d) when the location of interface is very closer from the input channel (the dashed horizontal line highlighted by white color) (e-g) when the location of interface is center, (h-j) when the location of interface is far away from the input channel (the dashed horizontal line highlighted by blue color).	<b>67</b>
<b>25</b>	<b>Fig.17:</b> Comparisons of the total acoustic pressure at 476 kHz in valley phononic Z-shaped waveguide (a) in Harmitian system, and (b-d) in non-Hermitian system (balanced with air loss, and air gain) with $\gamma = 0.5, 50$ , and $100$ , respectively, where the location of interface is at center.	<b>68</b>

## List of Tables

<b>Serial No.</b>	<b>Description</b>	<b>Page No.</b>
<b>01</b>	The two-dimensional hexagonal unit cell with six vertex A ( $X_1, Y_1$ ), B ( $X_2, Y_2$ ), C ( $X_3, Y_3$ ), D ( $X_4, Y_4$ ), E ( $X_5, Y_5$ ), and F ( $X_6, Y_6$ ), respectively.	<b>21</b>
<b>02</b>	The variable parameters that represent the transmission coefficient, and transmission loss.	<b>44</b>
<b>03</b>	Input pressure field for valley straight and reconfigurable straight waveguide.	<b>45</b>
<b>04</b>	Output pressure field for valley straight and reconfigurable straight waveguide.	<b>45</b>
<b>04</b>	Input pressure field for valley Z-shaped and reconfigurable Z-shaped waveguide.	<b>54</b>
<b>05</b>	Output pressure field for valley Z-shaped and reconfigurable Z-shaped waveguide.	<b>54</b>

## Nomenclature

PnC	Phononic Crystal
2D	Two - Dimensional
BG	Band Gap
BZ	Brillouin Zone
IBZ	Irreducible Brillouin Zone
TIs	Topological Insulators
AHE	Anomalous Hall Effect
QH	Quantum Hall
QSH	Quantum Spin Hall
QVHE	Quantum Valley Hall effect
GaAs	Gallium Arsenide
$\vec{T}$	Translational Vector
$\vec{T}_{partial}$	Partial Translation Vector
$\delta\vec{T}$	Continuous Translational Vector
$\gamma_n$	Berry Phase
$\vec{A}_n(\vec{k})$	Berry Connection
$\Omega(\vec{k})$	Berry Curvature
T	Transmission Coefficient
TL	Transmission Loss
EP	Exceptional Point
PT	Parity-Time

**Dedicated**  
**To My**  
**Beloved Parents Who Brought Me to This Universe,**  
**My Wife, and Children Who Sacrificed the Most**  
**During My Ph.D. Journey**

## Research Activities (Publications)

During the PhD research work, I presented international and domestic conferences, and published the following papers.

### Peer-Reviewed Journal Paper

[1] **Md. Shuzon Ali**, Motoki Kataoka, Masaaki Misawa, and Kenji Tsuruta\*. **Reconfigurable waveguide based on valley topological phononic crystals with local symmetry inversion via continuous translation**, Jpn. J. Appl. Phys. 62 (SJ1002-SJ1009), 2023.

[2] **Md. Shuzon Ali**, Yusuke Hata, and Kenji Tsuruta\*. **Active control of localized mode and transmission in phononic waveguide by non-Hermitian modulation**, Applied Physics Express (APEX), 2023. DOI 10.35848/1882-0786/acf1ef

[3] **Md. Shuzon Ali**, Yusuke Hata, Motoki Kataoka, Masaaki Misawa, and Kenji Tsuruta\*. **Robust and Reconfigurable Waveguide Design in Valley-Topological Phononic Crystals**. Materials Science Forum, 2023.

### Conference Paper

[1] **Md. Shuzon Ali**†, Motoki Kataoka, Masaaki Misawa, and Kenji Tsuruta. **Reconfigurable Waveguide Design in Valley-Topological Phononic Crystal**. Proceedings of Symposium on Ultrasonic Electronics (USE 2022) Vol. 43, 1Pal-3 (2 pages) (2022).

[2] Motoki Kataoka, **Md. Shuzon Ali**, Masaaki Misawa, Kenji Tsuruta. **Design of continuously deformable topological phononic structures and their application to elastic waveguides**. Proceedings of the 35<sup>th</sup> Computational Conference of the Japan Society of Mechanical Engineers (JSME) Vol. 2022.35, 20-01(3pages) (2022).

### Oral and Poster Presentation

- [1] **Md. Shuzon Ali**, Masaaki Misawa, and Kenji Tsuruta. “**Continuous translation of local  $C_{3v}$  symmetry for robust reconfigurable waveguide based on valley-topological phononic crystal**”. The 29<sup>th</sup> International Conference on Low Temperature Physics, Localisation 2022 (2022.08/26-30), Hokkaido University, Japan.
- [2] **Md. Shuzon Ali**, Motoki Kataoka, Masaaki Misawa, and Kenji Tsuruta, “**Reconfigurable Waveguide Design in Valley-Topological Phononic Crystal**”. The 43rd Symposium on Ultrasonic Electronics (USE 2022, 2022.11.07-09, Doshisha University, Muromachi Campus, Kyoto, Japan).
- [3] Kenji Tsuruta, **Md. Shuzon Ali**, Yusuke Hata, Motoki Kataoka, and Masaaki Misawa. “**Robust and Reconfigurable Waveguide Design in Valley-topological Phononic Crystals**”. The 12<sup>th</sup> International Conference on Processing & Manufacturing of Advanced Materials, 2023 (2023.07/02-07), Vienna University of Technology, Vienna, Austria.
-

# Chapter 1

## Introduction

### 1.1 Introduction

#### Background and Previous Work

Topologically protected wave mechanics in solids have become a new research topic in regarding energy and/or information transfer via various carriers of quantum and classical matter, such as photons represented by optical waves [1-2] and phonons represented by acoustic or elastic waves [3]. Essentially, the same phenomenon has been identified in quasi-two-dimensional PnC with a finite thickness, referred to as a phononic crystal plate [4-5]. Immunization against defects in topological phononic and photonic systems is of great interest because of their ability to confine or guide waves, which is desirable in various applications, such as wave filters [6-8], waveguides [9-10], and sensors [11-12]. The waveguide structure must be reconfigurable considering the active control of its functionality to use a topological waveguide in an integrated device. Some examples of such a reconfigurable structure for topological photonic waveguides can be found in recent literature. For example, the dynamic control of topological edge states in photonic crystals for robust energy transport has been demonstrated through the modification of the refractive index of a liquid crystal background medium [13]. Another type of topological photonic crystal has also been proposed based on a prototypical phase-change material  $\text{Ge}_2\text{Sb}_2\text{Te}_5$  (GST225) at a particular frequency and reversibly switched between “on” and “off” by transiting the GST225 structural state [14]. Additionally, another type of reconfigurability in a topological elastic wave insulator has been proposed and experimentally demonstrated [15]. This study adopted mainly the filling/draining liquid into holes. Tian et al. [16] presented a tunable valley PnC composed of hybrid channel-cavity cells with three tunable parameters. Zhuang et al. [17] presented a methodology for the inverse design of reconfigurable topological insulators for flexural waves in plate-like structures. Feng et al. [18] and Laude et al. [19] proposed two-dimensional reconfigurable PnC that supports topologically protected edge

states for Lamb waves.

Recently, the Berry curvature have been found to be important in explaining the topological phase transition of the band in a unit cell. Additionally, the chirality of the acoustic field intensity arises from the Berry curvature of the Dirac band. A tunable phononic crystal plate with Y-shaped prisms is designed to support valley transport of elastic waves, in which elastic valley pseudospin states exhibit opposite chirality similar to electronic spin states, based on the analogy of the quantum valley Hall effect [20]. The presence of topological states is because of the non-trivial topological character of bulk electronic bands called the bulk-edge correspondence [21-22] and has been shown even in the case of a weak disorder. The quantization of the Hall conductance due to the edge states becomes stable because they are chiral. However, more versatile designs are necessary for quantum Hall (QH), quantum spin Hall (QSH), and quantum valley Hall effect (QVHE) to achieve non-trivial topological phononic bandgaps. For example, additional active components, such as rotating gyroscopes or application of an external field, are needed to break the time reversal symmetry in QH systems [23-28], where the Berry curvature clearly reveals the chiral character of the edge mode. However, QSH systems require a Double-Dirac cone achieved by the zone folding method [29-31] for high-symmetry points. They also demonstrated the possibility of a topologically protected edge state. In 2018, Mei et al. [32] also investigated the non-trivial band topology phase transition for Lamb waves in a thin phononic crystal plate to realize the valley Hall effect in the low-frequency regime. In 2019, Kim et al. [33] proposed a GaAs-based valley PnC and demonstrated the control of the chiral characteristics of the bulk valley modes by rotating triangular holes in the unit cell through topological phase transition. In addition, they showed that topologically protected edge states at multiple frequency ranges can be characterized using the signs and distributions of the Berry curvature. These systems are commonly assumed to be Hermitian, despite non-Hermiticity naturally existing in a wide range of systems. Actually, in many situations, however, the systems are not more conservative because of their interactions with the environment that result in gain or loss; these are known as non-Hermitian systems [34-37]. The non-Hermitian represents a unique class of non-Hermitian system formed by balanced gain and loss [38-39], also known



as the parity-time (PT) symmetric system [40]. But the consideration of total-loss non-Hermitian system can be in line with the energy dissipation in real world [41-42], avoiding the introduction of gain [43-45], and making the actual implementation of non-Hermitian topology simpler. Xue et al. [46] reported the experimental realization of passive-symmetric quantum dynamics for single photons by temporally alternating photon losses in the quantum walk interferometers. Miri et al. [47] reviewed the recent developments in theoretical and experimental research based on non-Hermiticity, and examined future opportunities from basic science to applied technology. Acoustics can be regarded as a feasible and versatile platform to verify non-Hermitian concepts [48-53], which not only provides a better understanding but also brings non-Hermitian physics closer to real applications.

## **Motivation**

However, previously waveguide has been shown to be complicated for edge mode transmission. Thus, hampering the realization of integrated switchable acoustic device. Actually, these reports required specific mechanisms for the reconfiguration of waveguide structures without losing their robustness. Considering the implementation of integrated devices, a simpler but versatile approach to control the structural changes in the reconfiguration is needed. Moreover, it is desirable to have quantitative indices to characterize and/or optimize the waveguide structure during the reconfiguration. On the other hand, the practical realization of both gain and loss in acoustic systems remains a critical issue. Several proposals on the effective non-Hermite Hamiltonian have described coupled acoustic systems with well-designed sound leakages or additional losses [48,54]. Gu et al. [55] explained the basic concepts and mathematical tools required to deal with non-Hermite acoustics by studying pedagogical examples and demonstrated the superior abilities of non-Hermitian modulation for wave manipulation. But most of the previous efforts to improve the transmission efficiency have been devoted to find ways to reduce the material losses and/or structural defects effectively in waveguides.

## Objectives and outline of this thesis

A reconfigurable valley topological acoustic waveguide constructed using a 2D phononic crystal (PnC) with  $C_{3v}$  symmetric arrangement of three rods in the unit cell has been focused on this thesis. Structural reconfiguration was introduced by the continuous translation of rod arrays in the PnCs [56]. The topological phase transition in this translational change was quantitatively identified by the change in the Berry curvature. An interface between two types of PnCs with differently oriented unit cells exhibits high robustness of the valley transport of acoustic waves via the topologically protected state. The translation of the rods leaves a dimer array at the interface, creating a localized/defective mode along the waveguide. Despite the presence of the localized mode, the acoustic wave can propagate along the reconfigurable waveguide the same as the original waveguide. The continuous translation of a rod array can be used to turn on and off the bandgap. This can be a new approach to design a robust acoustic device with a high reconfigurability in Hermitian system. Secondly, I demonstrated that the introduction of strong loss effects leads to the extinction of localized modes in a non-Hermitian system. This mechanism can be understood as analogous to the bound-to-unbound transition in non-Hermitian quantum systems. This result suggests that large variations of non-Hermitian modulation can be used for active control of edge mode propagation along topological interfaces. The analyses are performed based on finite-element calculations and simulations by using a general-purpose software package (COMSOL Multiphysics) [57].

The organization of the thesis is the following. After the discussions of background, motivation, and objectives of the present thesis as well as the basic concept of “topological physics” in **Chap.1**, I have first described the pressure acoustic model that focuses the unit cell Brillouin Zone, and the model geometry of my research in **Chap.2**. Secondly, the phononic band and the Berry curvature to characterize the modes in terms of the symmetry of the unit cell have been highlighted. In **Chap.3**, I have described the translational shift of metallic rod from the initial position to reconfigured position. I have explained the theoretical approach for phononic band properties of different types of interfaces. Also, we have

designed reconfigured waveguides and have examined their transmission properties through the comparisons with other waveguide structures. **In Chap.4**, a novel approach to active control of localized mode and transmission in Z-shaped valley topological phononic waveguide has been proposed by introducing non-Hermitian modulation. Finally, we draw some conclusions in **Chap. 5**.

## **1.2 Crystal Structure**

Topological phonon physics is one of the crucial research topics based on the microscopic structure that leads to particular acoustic phenomena. The properties of the topological materials emerge from patterns which can be used the further development of optical or acoustic/ elastic device information technology. Now a days, the crystal structure is important because they are stacked together with each other. As for example, the graphite is composed of carbon atoms that forms loosely bonded sheets in their crystal structure. The term “crystal” is derived from the Greek *krystallos* (meaning “ice”) and was first used in connection with rock crystals. A crystal or graphical solid is a solid material whose constituents (such as atoms, molecules, or ions) are arranged in a highly ordered microscopic structure, forming a crystal lattice that extends in all direction. An ideal crystal is constructed by the infinite repetition of identical groups of atoms. A group is called the basis. The set of mathematical points to which the basis is attached called the lattice. The periodic structure of an ideal crystal is most easily described by a lattice.

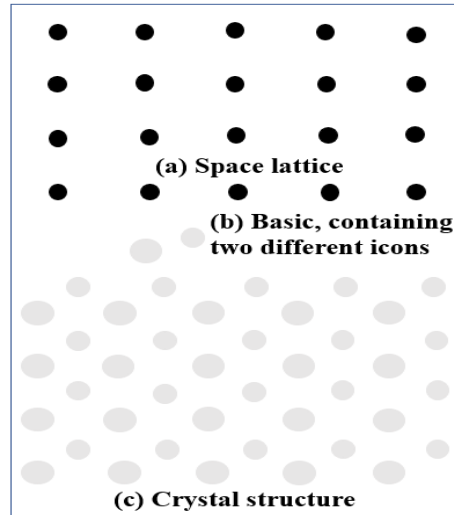


**Fig. (i):** The crystal structure is formed by the addition of the basis (b) to every lattice point of the space lattice (a). By looking at (c), one can recognize the basis and then one can abstract the space lattice.

### 1.3 Photonic Crystal, and Phononic Crystal

#### Photonic Crystal

Photonic crystals are periodic dielectric structures that are designed to form the energy band structure for photons, which either allows or forbids the propagation of electromagnetic waves of certain frequency ranges, making them ideal for light-harvesting applications (Source: Semiconductors and Semimetals, Maka et al.,2003).

#### Phononic Crystal

Phononic crystals (PCs) are usually defined as artificial materials made of periodic arrangement of scatters embedded in a matrix (A.-C. Hladky-Hennion, Applications of ATILA FEM Software to Smart Materials, 2013). An acoustic metamaterial, sonic crystal, or phononic crystal is a material designed to control, direct, and manipulate sound waves or

phonons in gases, liquids, and solids (crystal lattices). Actually, these type of material exhibits efficiently the flow of sound, acoustic waves, or elastic waves.

### 1.4 Reciprocal Lattice

The crystal lattice is the array of points of the atoms at the corners of all the unit cells in the crystal structure. In crystallography, the description of the ordered arrangement of atoms, ions, or molecules in a crystalline material is known as crystal structure. In physics, the reciprocal lattice represents the Fourier transform of another lattice (usually a Bravais lattice). A reciprocal lattice is the periodic set of the wave vectors  $\mathbf{k}$  in reciprocal space that make up the Fourier series of any function whose periodicity is compatible with that of an initial direct lattice in real space.

Let us consider, the fundamental translational lattice vectors of a two-dimensional (2D) hexagonal phononic are

$$\vec{a}_1 = a(1,0), \vec{a}_2 = a\left(-\frac{1}{2}, \frac{\sqrt{3}}{2}\right) \quad (\text{i})$$

or,

$$\vec{a}_1 = 2.2 * (1,0) = (2.2,0) \text{ and } \vec{a}_2 = 2.2 * \left(-\frac{1}{2}, \frac{\sqrt{3}}{2}\right) = (-1.1, 1.9)$$

where,  $a = 2.2$  mm is the lattice constant

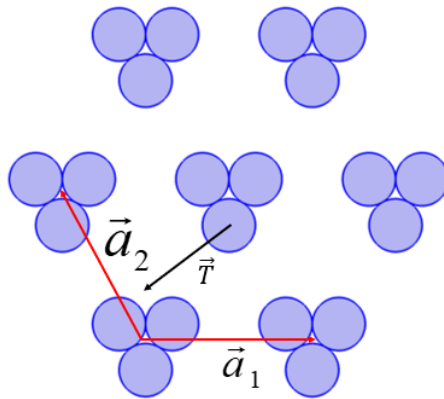


**Fig. (ii):** The crystal structure with translational vectors.

The two-dimensional reciprocal lattice is the set of vectors  $\vec{G}$  in Fourier space that satisfy the following requirement

$$\vec{G} \cdot \vec{T} = 2\pi \times \text{integer for any translation } (\vec{T})$$

$$\text{where } \vec{G} = m_1 \vec{b}_1 + m_2 \vec{b}_2$$

The primitive translation reciprocal lattice vector  $(\vec{b}_i, i=1,2)$  and  $\vec{b}_2$  are related to the primitive real space lattice vectors  $\vec{a}_1$  and  $\vec{a}_2$  by

$$\begin{cases} \vec{b}_1 = 2\pi \frac{\vec{a}_2 \times \hat{n}}{|\vec{a}_1 \times \vec{a}_2|} \\ \vec{b}_2 = 2\pi \frac{\hat{n} \times \vec{a}_1}{|\vec{a}_1 \times \vec{a}_2|} \end{cases} \quad (\text{ii})$$

where  $\hat{n}$  is outwardly directed unit vector normal to the surface and  $|\vec{a}_1 \times \vec{a}_2|$  is the area of the unit mesh. The mesh vectors have the following properties

$$\begin{aligned} \vec{b}_1 \cdot \vec{a}_1 &= \vec{b}_2 \cdot \vec{a}_2 = 2\pi \\ \vec{b}_1 \cdot \vec{a}_2 &= \vec{b}_2 \cdot \vec{a}_1 = 0 \end{aligned}$$

or briefly,

$$\vec{b}_i \cdot \vec{a}_j = 2\pi \delta_{ij} \begin{cases} \delta_{ij} = 1, \text{ if } i = j \\ = 0, \text{ if } i \neq j \end{cases} \quad (\text{iii})$$

where  $\delta_{ij}$  is Kronecker delta. The fundamental vectors of the reciprocal lattice are

$$\vec{b}_1 = \frac{2\pi}{a} (1,0), \vec{b}_2 = \frac{2\pi}{a} \left(-1, \frac{1}{\sqrt{3}}\right) \quad (\text{iv})$$

## 1.5 Unit Cell, Super Cell

### Unit Cell

The smallest representation of the entire crystal which is made up from the lattice points at each of the corners is known as unit cell. A Wigner–Seitz (WS) cell is a special primitive cell

that contains one lattice point. Actually, A primitive unit cell is the smallest area or volume which serves as the basic building block of the lattice.

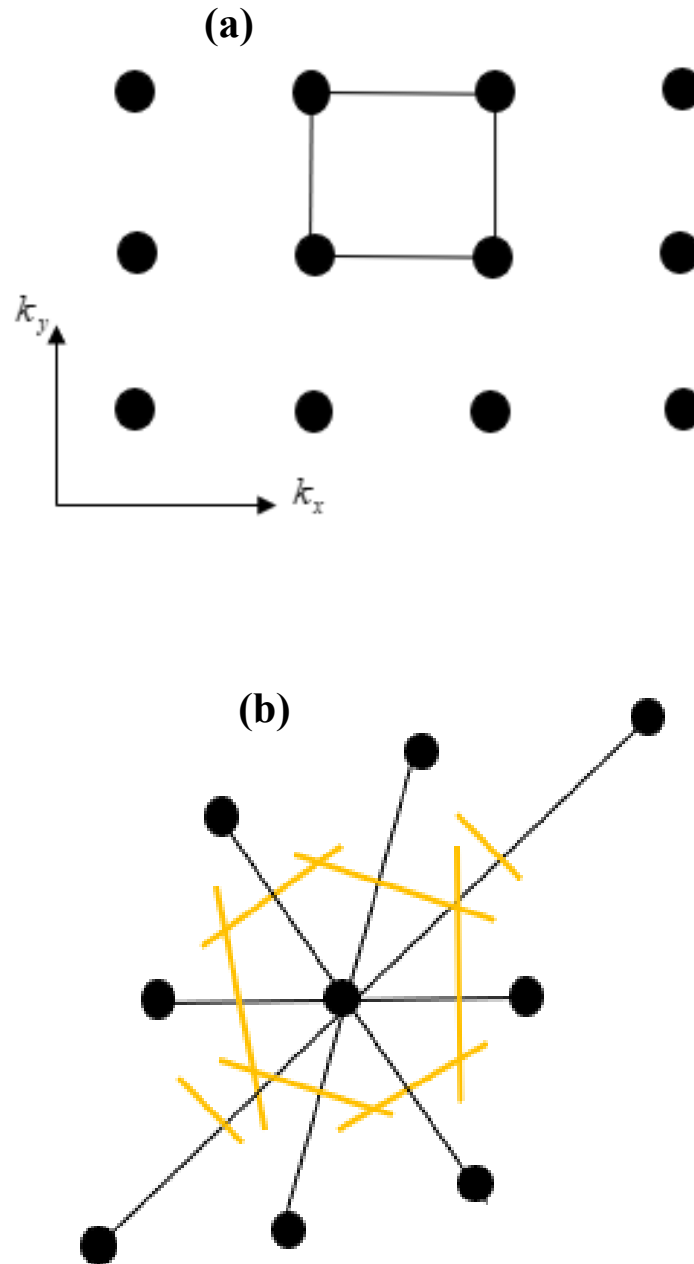


**Fig.(iii):** (a) Unit cell of the two-dimensional phononic crystal, and (b) Primitive unit cell.

## Super Cell

The periodical arrangement of the unit cell which describes the same crystal is called super cell. In Chap 2, we explained the phononic band properties in a supercell, where each unit cell is composed of three circular rods in a  $C_{3v}$  symmetry structure with  $\alpha = 30^\circ$  and  $\alpha = -30^\circ$  oriented, and separated by an interface.

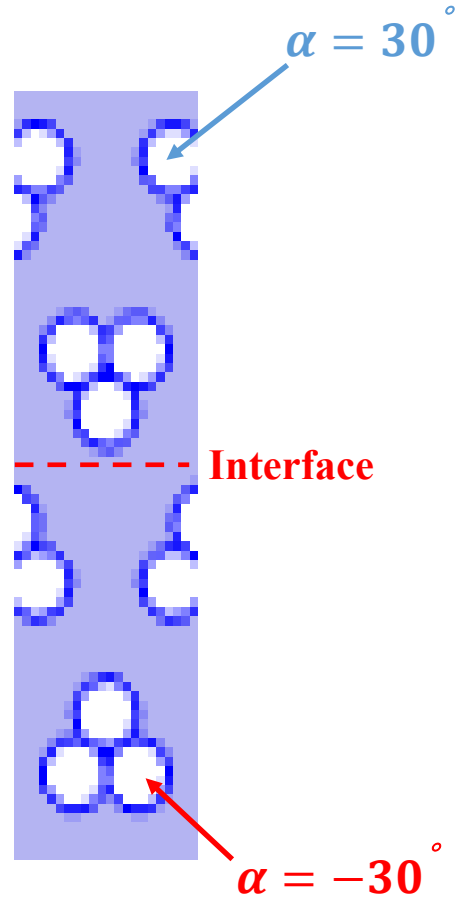


**Fig.(iv):** Supercell with differently oriented unit cell  $\alpha = 30^\circ$  and  $\alpha = -30^\circ$  layers have defined to distinguish by a topological interface (Adopted from M.S. Ali et al. Jpn. J. Appl. Phys, 2023).

## 1.6 Brillouin Zone, and Irreducible Brillouin Zone



## Brillouin Zone

The concept of Brillouin zone is particularly important in the consideration of the electronic structure of solids. A Brillouin zone is defined as a Wigner-Seitz primitive cell in the reciprocal lattice. The first Brillouin zone is the smallest volume entirely enclosed by planes that are the perpendicular bisectors of the reciprocal lattice vectors drawn from the origin. There are also second, third, *etc.*, Brillouin zones, corresponding to a sequence of disjoint regions (all with the same volume) at increasing distances from the origin, but these are used more rarely. As a result, the first Brillouin zone is often called simply the Brillouin zone.

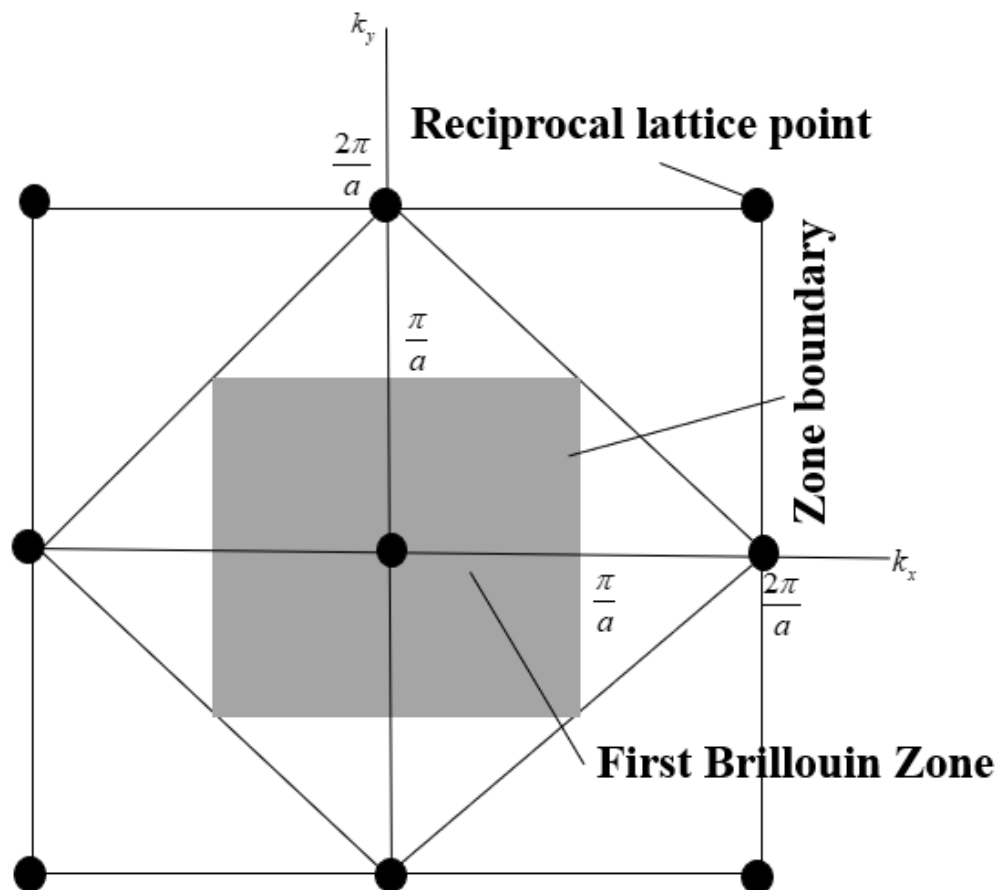


**Fig.(v):** The first Brillouin zone for a two-dimensional square lattice.

### Irreducible Brillouin Zone

The smallest volume of space within the Brillouin zone that completely characterizes the periodic structure is called the irreducible Brillouin zone (IBZ).

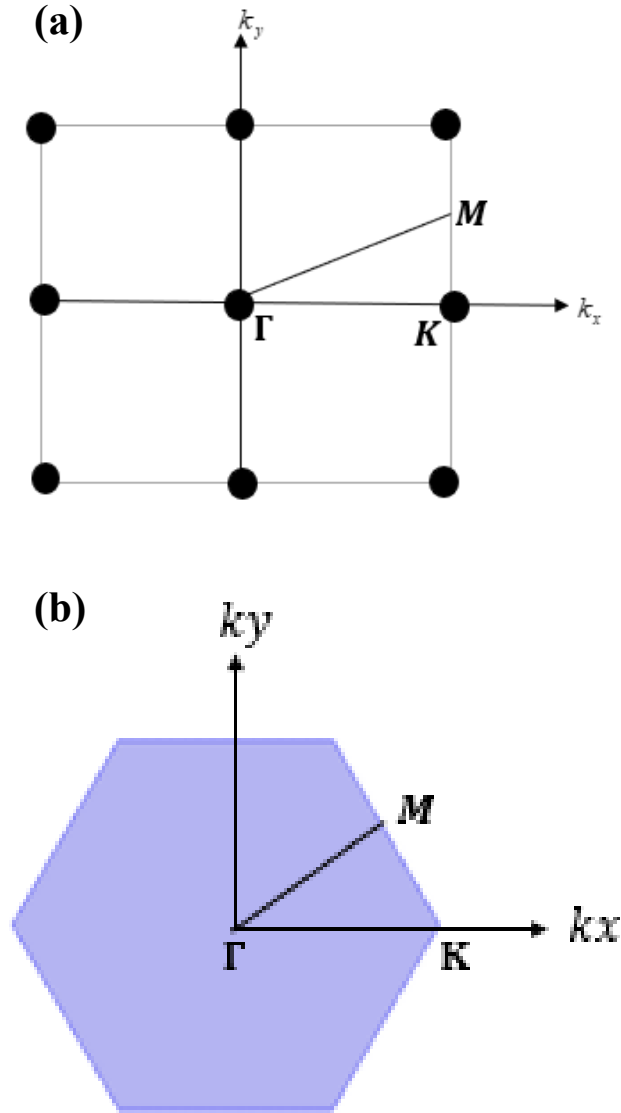


**Fig.(vi):** The first irreducible Brillouin zone for the periodic composites with (a) square lattice:  $\Gamma(kx, ky) = (0,0)$  ,  $X(kx, ky) = \left(\frac{\pi}{a}, 0\right)$  , and  $M(kx, ky) = \left(\frac{\pi}{a}, \frac{\pi}{a}\right)$  , and (b) hexagonal lattice:  $\Gamma(kx, ky) = (0,0)$ ,  $K(kx, ky) = \left(\frac{4\pi}{3a}, 0\right)$ , and  $M(kx, ky) = \left(\frac{\pi}{a}, \frac{\pi}{\sqrt{3}a}\right)$ .

## 1.7 Bloch's Theorem, Band Gap, and Dispersion Relation

### Bloch's Theorem

The theorem is named after the Swiss physicist Felix Bloch, who discovered in 1929. Bloch's theorem states that, in a periodic medium, the Eigen functions of a Hermitian eigenvalue problem can be written as the product of plane wave  $e^{i\vec{k} \cdot \vec{r}}$  and a periodic function  $u(\vec{r})$  that has the same periodicity with the lattice vector  $\vec{R}$ .

$$\vec{H}_k(\vec{r}) = e^{i\vec{k} \cdot \vec{r}} \vec{u}_k = e^{i\vec{k} \cdot \vec{r}} \vec{u}_k(\vec{R} + \vec{r})$$

where the parameter  $u$  represents displacement at the nodes,  $\vec{r}$  is located on the periodic boundary nodes,  $\vec{k} = (k_x, k_y)$  represents the two-dimensional wave vector in the irreducible Brillouin zone. The above equation provides the eigenvectors as well as the corresponding Eigen frequencies.

### Band Gap

In solid-state physics, a band gap is a frequency gap where no electronic state exists between the valence band and the conductance band in a solid. Actually, it represents the energy difference between the valence band and conductance band.

Actually, photonic crystals are periodically structured electromagnetic media, generally possessing photonic band gaps: range of frequency in which light cannot propagate through the structure. Similarly, phononic band gaps are range of frequencies in which elastic/phonon waves are not allowed to propagate.

### Dispersion Relation

Dispersion is defined as the variation of a propagating wave's wavelength  $\lambda$  with frequency  $f$ . For convenience, dispersion is also frequently represented as the variation of the propagating wave's wavenumber  $k = \frac{2\pi}{\lambda}$  with angular frequency  $\omega = 2\pi f$ .

Consider the one-dimensional scalar wave equation

$$\frac{\partial^2 u}{\partial t^2} = c^2 \frac{\partial^2 u}{\partial x^2}; \text{ where } u = u(x, t) \quad (\text{vi})$$

Also consider a continuous sinusoidal traveling-wave solution of (vi) written in phasor form

$$u(x, t) = e^{i(\omega t - kx)} \quad (\text{vii})$$

where  $\omega$  and  $k$  are defined above, and  $i = \sqrt{-1}$ . Substituting into the equation (vi) and factoring out the complex exponential to both sides, we obtain

$$-\omega^2 = c^2(-k^2)$$

or,

$$\begin{aligned} \omega^2 &= c^2 k^2 \\ \therefore k &= \pm \frac{\omega}{c} \end{aligned} \quad (\text{viii})$$

This represents the dispersion relation for the one-dimensional scalar wave equation. The plus sign designates +x directed wave propagation, while the minus sign designates -x directed wave propagation.

We can obtain an expression for the wave phase velocity, classically defined as  $v_p = \frac{\omega}{k} = \pm c$ .

The phase velocity is seen to be  $\pm c$ , a constant regardless of frequency. Differentiate equation (viii) with respect to wave number  $k$  to obtain the wave group velocity, classically

defined as  $v_g = \frac{d\omega}{dk}$ . This yields

$$\begin{aligned} 2\omega \frac{d\omega}{dk} &= c^2 \cdot 2k \quad \text{or,} \quad \frac{d\omega}{dk} = \frac{k}{\omega} c^2 \quad \text{or,} \quad \frac{d\omega}{dk} = \frac{c^2}{\omega} \left( \pm \frac{\omega}{c} \right) \\ \therefore v_g &= \pm c \end{aligned}$$

This shows that the group velocity is also independent of the frequency (**Source: Allen Taflov, and Susan C. Hagness, Computational Electrodynamics the finite- difference time domain method, 2005**).

## 1.8 Berry Phase, Berry Connection, and Berry Curvature

In physics, the Berry curvature is related with Berry connection, as a local gauge potential and gauge field associated with the Berry phase or geometric phase. The concept of Berry curvature was first introduced by S. Pancharatnam as geometric phase and later elaborately explained and popularized by Michael Berry in a paper published in 1984 emphasizing how geometric phases provide a powerful unifying concept in several branches of classical and quantum physics.

We consider a physical system which described by a Hamiltonian in Hermitian regime that depends only on time through a set of parameters, defined by  $\vec{R} = (R_1, R_2, \dots, R_N)$ . So, we can write,

$$H = H(\vec{R}), \text{ and } \vec{R} = \vec{R}(t)$$

Let  $\vec{R}(t)$  moves along a path in the adiabatic system. It will be useful to introduce an instantaneous orthonormal basis from the eigenstates of  $H(\vec{R})$  at each value of the parameter  $\vec{R}$  . i.e.,

$$H(\vec{R})u_n(\vec{R}) = \varepsilon_n(\vec{R})u_n(\vec{R})$$

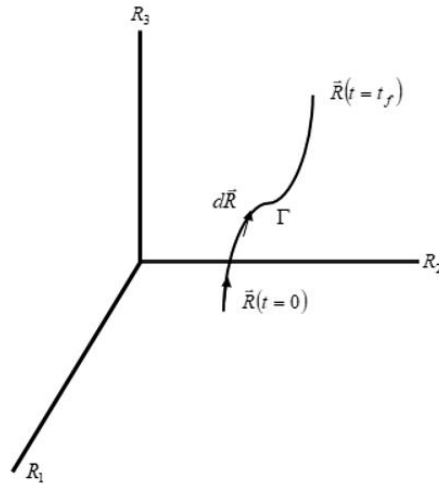


**Fig.(vii):** The parametric position of  $\vec{R}(t)$  along a path.

where an arbitrary  $\vec{R}$  still dependent on the phase factor of  $|u_n(\vec{R})\rangle$ . To remove this arbitrary phase factor, one can make a phase choice, also known as a gauge.

Let us suppose a state at time  $t$  as the following form

$$|u_n(t)\rangle = e^{i\gamma_n(t)} e^{-\frac{i}{\hbar} \int_0^t dt' \varepsilon_n(\vec{R}(t'))} |u_n(\vec{R}(t))\rangle$$

where the second exponential is known as the dynamical phase factor. Inserting the above equation into the time-dependent Schrödinger equation

$$i\hbar \frac{\partial}{\partial t} |u_n(t)\rangle = H(\vec{R}(t)) |u_n(t)\rangle$$

Multiplying it from the left by  $\langle u_n(\vec{R}(t)) |$ , one finds that  $\gamma_n$  can be expressed as a path integral in the parameter space

$$\gamma_n = \int_C \vec{\Lambda}_n(\vec{R}) \cdot d\vec{R} \quad (\text{ix})$$

where the single-valued function  $\vec{\Lambda}_n(\vec{R})$  is known as Berry connection or Berry vector potential, and  $\vec{\Lambda}_n(\vec{R}) = i \langle u_n(\vec{R}) | \frac{\partial}{\partial \vec{R}} | u_n(\vec{R}) \rangle$ .

Calculation of Berry connection  $\vec{\Lambda}_n(\vec{R})$ :

Suppose  $\gamma_n(t) = \int_0^t \nu_n(t') dt'$  ; where  $\nu_n(t) = i \langle u_n | \frac{d}{dt} | u_n \rangle$  (x)

$$\begin{aligned} \frac{d}{dt} u_n(\vec{R}(t)) &= \frac{d}{dt} u_n(R_1(t), R_2(t), \dots, R_N(t)) \\ \text{Now,} \quad &= \frac{\partial u_n}{\partial R_1} \frac{dR_1}{dt} + \frac{\partial u_n}{\partial R_2} \frac{dR_2}{dt} + \dots + \frac{\partial u_n}{\partial R_N} \frac{dR_N}{dt} \\ &= \nabla_{\vec{R}} u_n \cdot \frac{d\vec{R}}{dt} \end{aligned}$$

From the equation,

$$\begin{aligned}\nu_n(t') &= i \langle u_n \vec{R}(t') | \frac{d}{dt} | u_n \vec{R}(t') \rangle \\ &= i \langle u_n \vec{R}(t') | \nabla_{\vec{R}} | u_n \vec{R}(t') \rangle \cdot \frac{d\vec{R}}{dt'}\end{aligned}$$

From the above equation, we can write

$$\begin{aligned}\gamma_n(t) &= \int_0^t i \langle u_n \vec{R}(t') | \nabla_{\vec{R}} | u_n \vec{R}(t') \rangle \cdot \frac{d\vec{R}}{dt'} \cdot dt' \\ \Leftrightarrow \gamma_n(\Gamma) &= \int_{\Gamma} i \langle u_n \vec{R}(t) | \nabla_{\vec{R}} | u_n \vec{R}(t) \rangle \cdot d\vec{R}\end{aligned}$$

Therefore,  $\vec{\Lambda}_n(\vec{R}) = i \langle u_n(\vec{R}(t)) | \frac{\partial}{\partial \vec{R}} | u_n(\vec{R}(t)) \rangle$ . The Berry connection is gauge- dependent,

transforming as  $\tilde{\vec{\Lambda}}_n(\vec{R}) = \vec{\Lambda}_n(\vec{R}) + \nabla_{\vec{R}} \beta(\vec{R})$  to a new set of states differ from the original ones only by an  $\vec{R}$  - dependent phase vector. This modifies the open-path Berry phase to be  $\tilde{\gamma}_n(t) = \gamma_n(t) + \beta(t) - \beta(0)$ . So, for a closed path, continuity requires that  $\beta(t) - \beta(0) = 2\pi m$  ( $m$  an integer), and it follows that  $\gamma_n$  is a gauge-invariant physical quantity, modulo  $2\pi$ , now known as the Berry phase or geometric phase in general; it is given by

$$\gamma_n = \oint_C \vec{\Lambda}_n(\vec{R}) \cdot d\vec{R} \quad (\text{xi})$$

For a closed path  $C$  that forms the boundary of a surface  $S$ , the line integral can be written using Stokes' theorem as

$$\begin{aligned}\oint_C \vec{\Lambda}_n(\vec{R}) \cdot d\vec{R} &= \oiint_S \nabla_{\vec{R}} \times \vec{\Lambda}_n(\vec{R}) \cdot d\vec{S} \\ &= \oiint_S \nabla_{\vec{R}} \times \vec{\Lambda}_n(\vec{R}) d^2 R \\ &= \oiint_S \Omega_n(\vec{R}) d^2 R\end{aligned}$$

where  $\Omega_n(\vec{k}) = \nabla_{\vec{k}} \times \vec{\Lambda}_n(\vec{k})$  is known as Berry curvature in  $k$  space, and  $\nabla_{\vec{k}} = (\partial_{k_x}, \partial_{k_y})$ .

Now, we explore the topology of the valley in the observed anisotropic band structure. After obtaining the dispersion relation  $\omega = \omega(k)$  and displacement vector field  $u(\vec{k})$ , we characterize the topology of valley phononic band of the unit cell by calculating the Berry curvature using the discrete method.

For our two-dimensional system, we consider a clockwise path around a certain point  $A(k_x, k_y)$  consisting of  $\vec{k}_1(k_x - \frac{\delta k_x}{2}, k_y - \delta k_y/2)$ ,  $\vec{k}_2(k_x - \frac{\delta k_x}{2}, k_y + \delta k_y/2)$ ,  $\vec{k}_3(k_x + \frac{\delta k_x}{2}, k_y + \delta k_y/2)$ , and  $\vec{k}_4(k_x + \frac{\delta k_x}{2}, k_y - \delta k_y/2)$ . Since we consider the continuous Brillouin zone as numerous small patches, for each path  $\delta k_x \times \delta k_y$ , we estimate the Berry curvature as below:

$$\Omega(\vec{k}) = \frac{-\text{Im}[\langle u(\vec{k}_1) | u(\vec{k}_2) \rangle + \langle u(\vec{k}_2) | u(\vec{k}_3) \rangle + \langle u(\vec{k}_3) | u(\vec{k}_4) \rangle + \langle u(\vec{k}_4) | u(\vec{k}_1) \rangle]}{\delta k_x \times \delta k_y}$$

(xii)



## Chapter 2

### Modeling and characterization

#### 2.1 Introduction

The topological properties of the band structure, that is, electronic bands in quantum mechanics or dispersion surfaces in photonic, acoustic and mechanical systems can be exploited to achieve unique and exciting functionalities [1]. The exploration of such properties has motivated the development of classification schemes for the various types of topological phases that are available [2-3]. One very significant aspect that accompanies the Berry phase in affecting optical and electronic as well as acoustic properties of solid crystal materials is the symmetry. In photonics, symmetry has been used to study the bandgaps and passbands of Photonic Crystals (PhC) as well as the confined eigen-modes of PhC defect cavities [4]. The role of symmetry in circular cavities has also been studied and various applications have been proposed [5-7]. A periodic structure possesses a higher symmetry when the unit cell coincides with itself after more than one linear or angular translation or reflection [8-11]. These studies uncovered the profound impact that higher symmetries have on the propagation properties of periodic structures: to reduce or even eliminate the dispersion of the lowest mode [12] and to remove band gaps at the Brillouin zone boundary [13-14]. The modern formalism of the intrinsic anomalous Hall conductivity (AHC) provides profound insight into the anomalous Hall effect (AHE) of being closely related with the topology of one-electron energy bands [15-17]. It is the source of anomalous velocity [18], and also plays a role in topological insulators [19], and other fields [20]. Therefore, the determination of the Berry curvature is of fundamental importance to condensed matter physics but has so far only been accessible to numerical calculations [21-23] or measurements in optical lattice [24-25]. In this chapter, Firstly, we explained the model equations in pressure acoustic frequency domain. We calculate the Bloch's dispersion relation between wave vector and angular frequency to characterize the  $C_{3v}$  symmetric and breaking symmetric topological phase of the mode in the Brillouin zone of periodic unit cell structure. We also evaluate the Berry curvature for the upper and lower band to explain the

band topology phase transition through the unit cell. The results demonstrate that the band topology phase transition is controlled by Berry curvature.

## 2.2 Model Equations

The governing equations of our 2D model can be written as

$$\begin{aligned} \nabla \cdot \left( -\frac{1}{\rho_c} \right) (\nabla p_t - \vec{q}_d) - \frac{k_{eq}^2 p_t}{\rho_c} &= Q_m \\ p_t &= p + p_b \\ k_{eq}^2 &= \left( \frac{\omega}{c_c} \right)^2 - k_z^2 \end{aligned} \quad (\text{A})$$

where  $\vec{q}_d$  is the dipole domain source;  $Q_m$  is the monopole domain source;  $\rho_c$  is the density;  $p$  is the pressure;  $p_t$  is the total pressure field; and  $p_b$  is the background (incident) pressure field; and  $c_c$  is the speed of sound.

The first Brillouin zone path vary  $\Gamma \rightarrow K \rightarrow M \rightarrow \Gamma$ . The component of the wave vector  $kx$  and  $ky$  of the hexagonal unit cell can be expressed by the following way

$$\begin{cases} \text{if } k < 1, (kx, ky) = \left( \frac{4\pi}{3a} k, 0 \right) \\ \text{if } k < 2, (kx, ky) = \left( \frac{4\pi}{3a} - \frac{(k-1)}{3a} \pi, \frac{(k-1)}{\sqrt{3}a} \pi \right) \\ \text{if } k < 3, (kx, ky) = \left( \frac{(3-k)}{a} \pi, \frac{(3-k)}{\sqrt{3}a} \pi \right) \end{cases} \quad (\text{B})$$

As far as we know the smallest volume of space within the Brillouin zone that completely characterizes the periodic structure is known irreducible Brillouin zone (IBZ). The irreducible Brillouin zone  $\Gamma \rightarrow K \rightarrow M$  of hexagonal lattice is defined as  $\Gamma(kx, ky) = (0,0)$ ,  $K(kx, ky) = \left( \frac{4\pi}{3a}, 0 \right)$  and  $M(kx, ky) = \left( \frac{\pi}{a}, \frac{\pi}{\sqrt{3}a} \right)$  respectively.

The geometry of two-dimensional phononic crystal comprises usually parallel inclusions infinite along the z-direction and arranged periodically in the  $xy$  plane.

We preferred the hexagonal unit cell structure as the model geometry of my research, because it can cover the entire area of a two-dimensional plane with equal -sized cells while minimizing the overlap between the neighboring cells. i.e., no gap remains between the

graphical region. Moreover, the hexagonal structure improves the stability than any other traditional design (as for example: square).

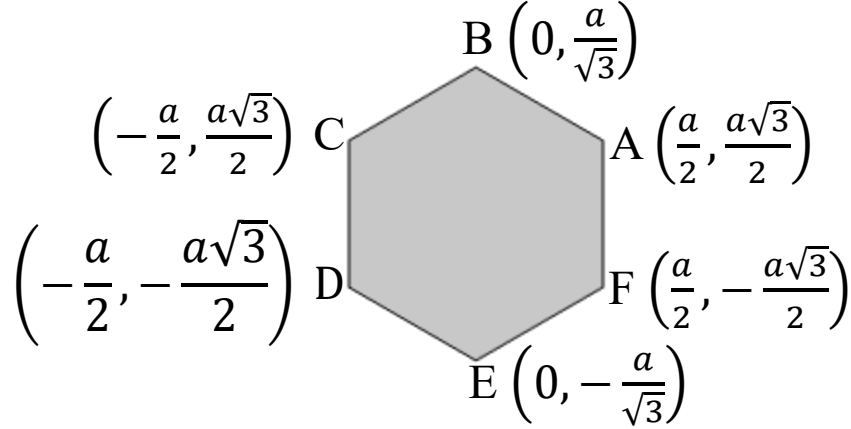


**Fig.(viii):** Two dimensional (2D) Hexagonal structure.

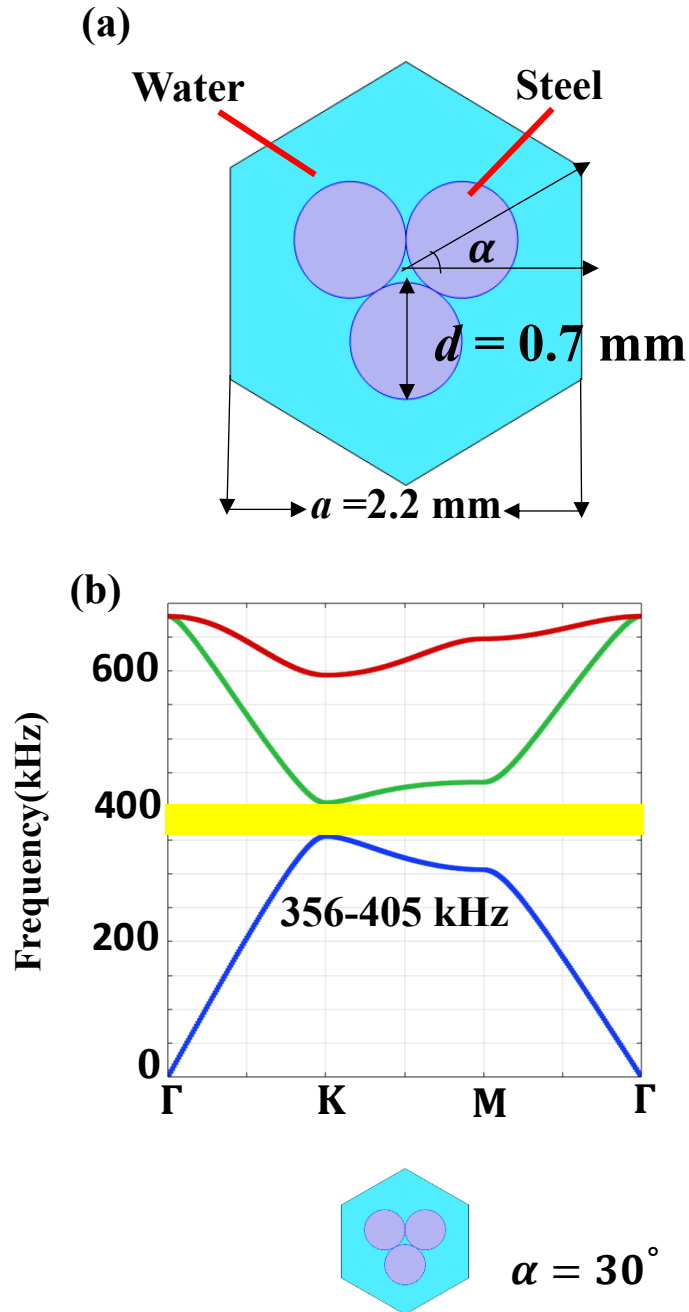
The six vertices of the proposed two-dimensional hexagonal unit cell structure with lattice constant  $a = 2.2$  mm are given in the following table 1:

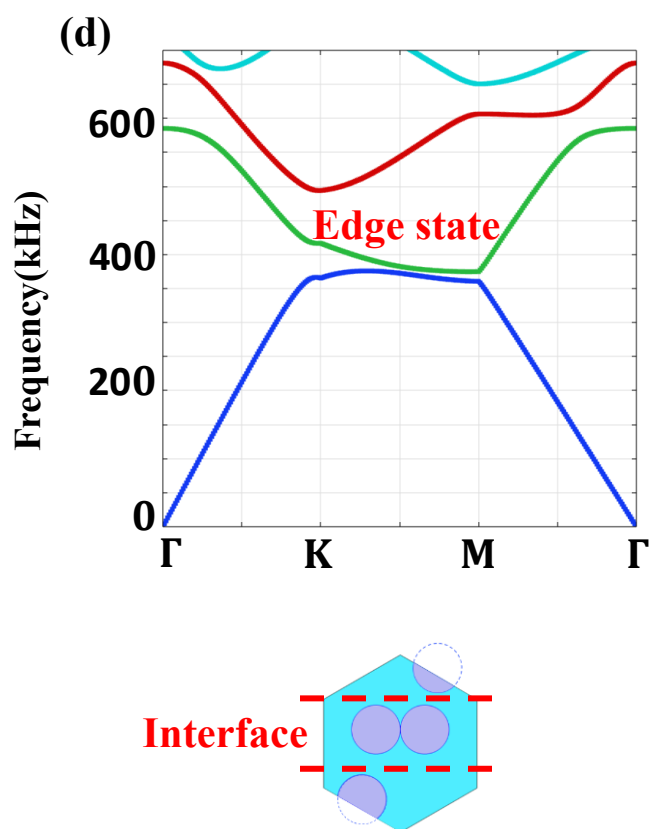
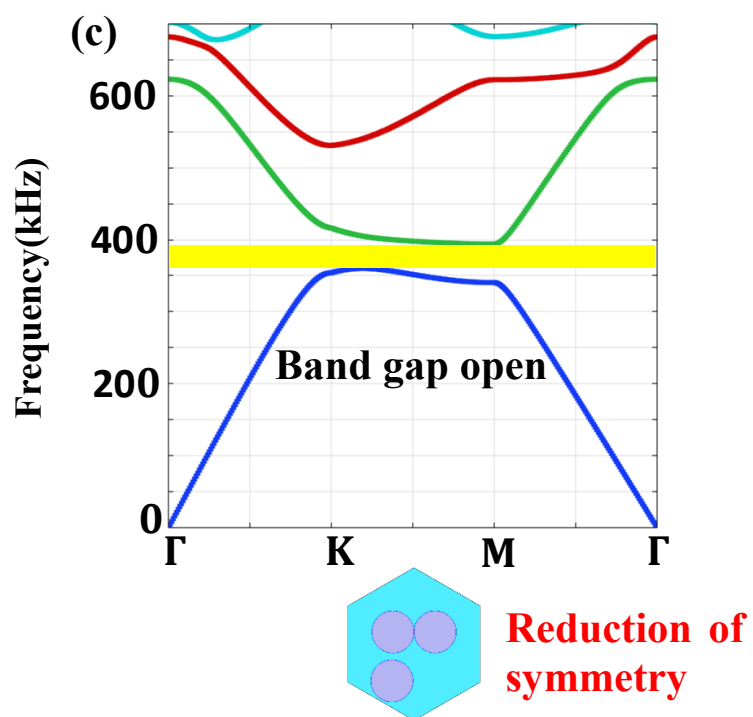
Name of the coordinate point of six vertices	Horizontal value $X_i$ ( $i = 1$ to $i = 6$ )	Vertical value $Y_j$ ( $j = 1$ to $j = 6$ )
A ( $X_1, Y_1$ )	$\frac{a}{2}$	$\frac{a\sqrt{3}}{2}$
B ( $X_2, Y_2$ )	0	$\frac{a}{\sqrt{3}}$
C ( $X_3, Y_3$ )	$-\frac{a}{2}$	$\frac{a\sqrt{3}}{2}$
D ( $X_4, Y_4$ )	$-\frac{a}{2}$	$-\frac{a\sqrt{3}}{2}$
E ( $X_5, Y_5$ )	0	$-\frac{a}{\sqrt{3}}$
F ( $X_6, Y_6$ )	$\frac{a}{2}$	$-\frac{a\sqrt{3}}{2}$

### 2.3 Phononic Band Analysis

In our model, the unit cell structure is composed of three circular rods of solid material (stainless steel) arranged in a hexagonal lattice embedded in water, as shown in **Fig. 1(a)**, which was proposed by Okuno et al. [26] by considering the ease of fabrication. We set the

lattice constant  $a = 2.2$  mm and the diameter of each circular rod  $d = 0.7$  mm, which defines the radius of each circular rod as  $r = d/2 = 0.35$  mm. The speed of sound and mass density are 1490 m/s and 1000 kg/m<sup>3</sup> for water, and 5780 m/s and 7800 kg/m<sup>3</sup> for stainless-steel rods, respectively. The relative orientation ( $\alpha$ ) of the rod array in the hexagonal lattice characterizes the symmetry of the structure.





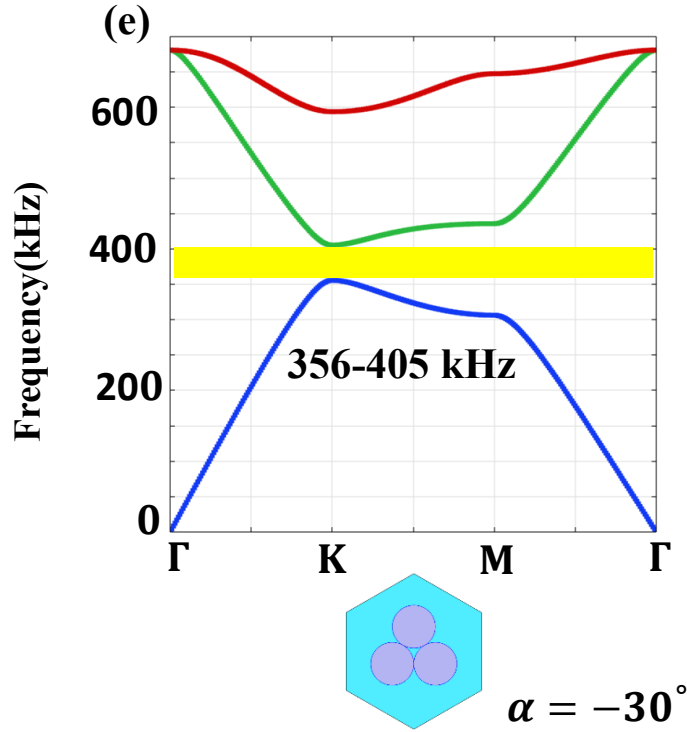


**Fig.1:** (a) Hexagonal unit cell with  $C_{3v}$  symmetry, and band structures (b) for the unit cell with  $\alpha = 30^\circ$ , (c) for the unit cell with partially shifted rod, (d) for the unit cell with intermediate shift, and (e) for the unit cell with  $\alpha = -30^\circ$  (Adopted from M.S. Ali et al. *Jpn. J. Appl. Phys*, 2023).

At the angle  $\alpha = 30^\circ$ , the unit cell structure illustrated in **Fig. 1(b)**, the band structure shows valley-type dispersion at the K point, and the band gap opens around the frequency of 356–405 kHz, whereas the flipped band is observed for the unit cell structure with  $\alpha = -30^\circ$ , as depicted in **Fig. 1(c)**. Instead of a continuous change in  $\alpha$ , the rotation of the rod array, a structural transformation between the structures, illustrated in **Figs. 1(b)** and **1(e)** can also be undertaken by translational shifts, as proposed in the previous section and is illustrated in **Fig. 1**. The symmetry breaking of the unit cell by the translation of a rod leads to the reduction in the symmetry, and it generates another band structure where the gap still opens, as shown in **Figs. 1(c)** and **1(d)**.

Nevertheless, we show in the following section that the interface between the PnC with and without translation creates an edge mode. This implies that band gap closing alone cannot be the definitive measure to identify the bulk bands that lead to the emergence of an edge state after constructing interfaces. Instead, topologically invariant quantities are required for identification. We highlighted the Berry curvature approach through the unit cell associated with both the upper and lower bands around the band gap to identify the topological phase for each phononic band.

## 2.4 Topological Phase Transition via Application of Berry Curvature

The Berry phase of the  $n$ -th band along a closed path  $C$  is defined as

$$\gamma_n = \oint_C \vec{A}_n(\vec{k}) \cdot d\vec{k} = \oint_S \Omega_n(\vec{k}) d^2k ,$$

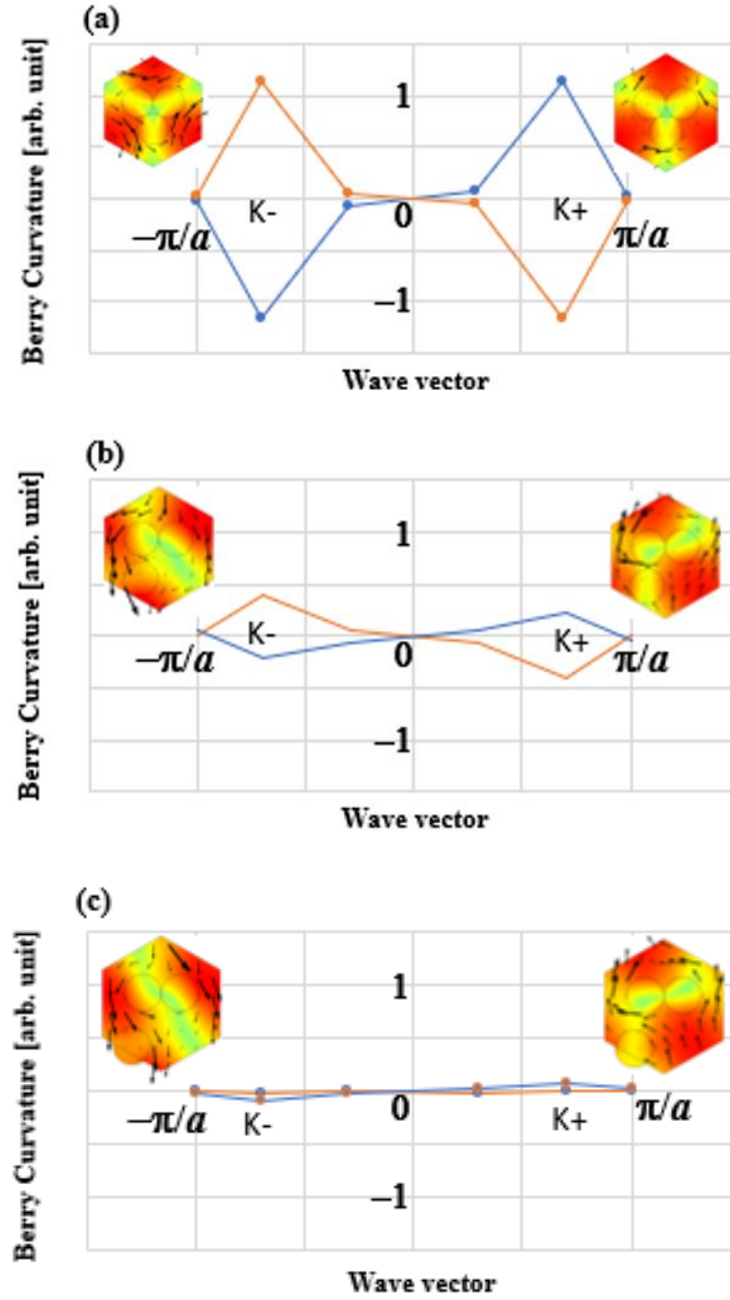
where  $\vec{A}_n(\vec{k})$  is the Berry connection and  $\vec{A}_n(\vec{k}) \equiv \langle u_n(\vec{k}) | i \nabla_{\vec{k}} | u_n(\vec{k}) \rangle$  and  $\Omega_n(\vec{k}) = \nabla_{\vec{k}} \times \vec{A}_n(\vec{k})$  is the Berry curvature [19].

In our calculation, the Berry curvature at a certain point  $(k_x, k_y)$  in  $k$  space is expressed as [28]

$$\Omega(\vec{k}) = \frac{-\text{Im}[\langle u(\vec{k}_1) | u(\vec{k}_2) \rangle + \langle u(\vec{k}_2) | u(\vec{k}_3) \rangle + \langle u(\vec{k}_3) | u(\vec{k}_4) \rangle + \langle u(\vec{k}_4) | u(\vec{k}_1) \rangle]}{\delta k_x \times \delta k_y} ,$$

where  $\vec{k}_j (j = 1, 2, 3, 4)$  are four points of the rectangle surrounding a point in  $k$  space, creating a counterclockwise path:  $\vec{k}_1 \left( k_x - \frac{\delta k_x}{2}, k_y - \delta k_y/2 \right)$ ,  $\vec{k}_2 \left( k_x - \frac{\delta k_x}{2}, k_y + \delta k_y/2 \right)$ ,  $\vec{k}_3 \left( k_x + \frac{\delta k_x}{2}, k_y + \delta k_y/2 \right)$ , and  $\vec{k}_4 \left( k_x + \frac{\delta k_x}{2}, k_y - \delta k_y/2 \right)$ . The displacement vector field term  $u_n(\vec{k})$  for the two-dimensional Eigen mode. In our numerical calculation, all Eigen modes were normalized with respect to the integration of  $\langle u_n(\vec{k}) | u_n(\vec{k}) \rangle$  over the surface of the unit cell. Figures **2(a)** to **2(d)** show the Berry curvature distributions along the path (highlighted by arrow line with red color in **Fig.2(e)**) in the Brillouin zone depicted in the inset of the figure for the unit-cell structures during the translational shifting of a rod. These figures reveal that each sign of the Berry curvature around the  $K^+$  and  $K^-$  points for the upper

and lower bands are continuously flipped during the translational shift. The insets in the figure also show the pressure fields and the acoustic-intensity distributions at indicates  $K+$  and  $K-$  points indicating that the chiral state of each band was also continuously flipped by the translational shift.





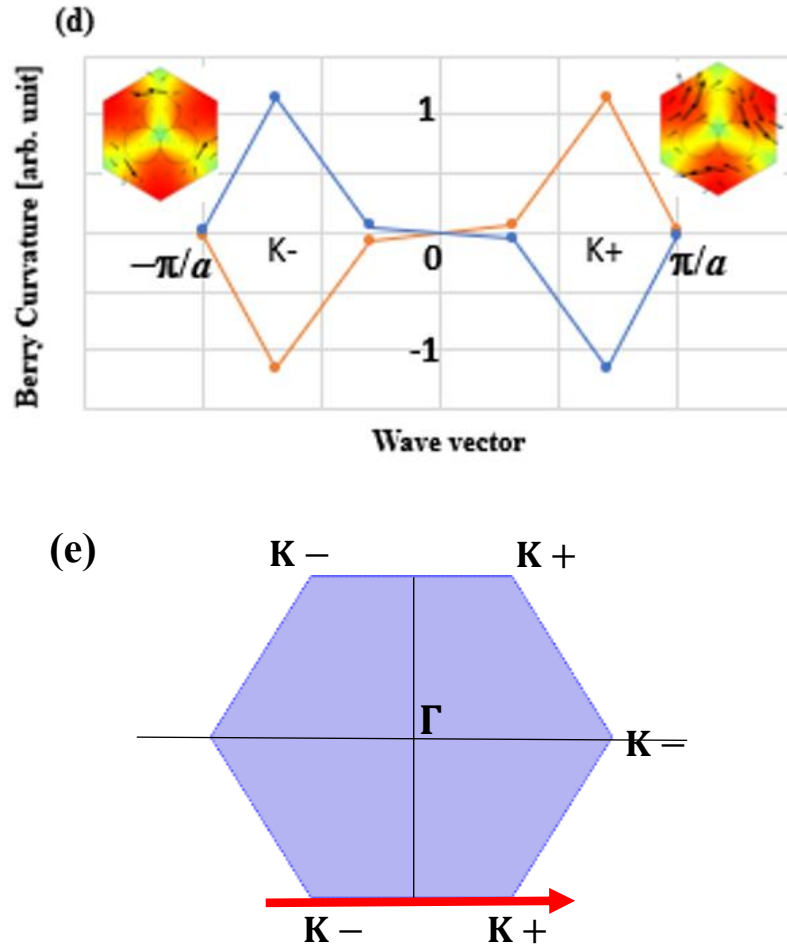


**Fig.2:** Berry curvatures of the lower and upper bands in the reciprocal space near the  $K+$  and  $K-$  valleys (a) for the unit cell with  $\alpha = 30^\circ$ , (b) for the unit cell with partially shifted rod array, (c) for the unit cell with intermediate shift, (d) for the unit cell with  $\alpha = -30^\circ$ . Insets show pressure fields (color) and acoustic-intensity distributions (arrow) of the mode at  $K+$  and  $K-$  points, and (e) Hexagonal Brillouin zone, where the arrow line (highlighted by red color) represents the direction of the path of  $K-$  to  $K+$  points (**Adopted from M.S. Ali et al. Jpn. J. Appl. Phys, 2023**).

## Chapter 3

### **Theoretical Approach for Topological Phononic $C_{3v}$ Symmetric Supercell and Reconfigurable Waveguide Design**

#### **3.1. Introduction**

A better topological acoustic waveguide is fundamental requirement to control wave propagation along the edge state, by taking the advantage of topological protection. The acoustic structure with periodic arrangement has an importance in the field of topological physics because of their inherent properties. Recently, interesting topological phenomena, such as topological interface and edge states have been observed in acoustic systems [1-2]. Actually, the achievement of topological protected edge is a fundamental criterion for acoustic wave propagation in which only two-fold degeneracy at the Dirac cone is necessary before opening a topological band gap [3-4]. On the other hand, the concept of directional waveguides in metamaterials is a widely researched topic [5-6]. The acoustic waves that can propagate through the edges are called topological protected edge waves [7]. A key feature of TIs is the existence of topologically protected edge states at the interface between two materials with distinct topological invariants, which are immune to backscattering and robust against impurities and defects, providing possibilities for developing novel topological devices [8]. Conventional TIs enable the transmission of edge modes at the interface between trivial and non-trivial photonic topological insulators (PTIs) without backscattering effect which can be allows for integrated topological apparatus, such as topological circuits [9-10] and topological photonic chips [11-12]. On the other hand, analogous to quantum Hall effect (QHE), topologically protected transport by breaking time reversal (T) symmetry is possible in photonic crystals [13]. Wang et al., [14] and Nash et al., [15] introduced gyroscopic inertial effects in phononic lattices to break the T-symmetry, and realize phononic edge states that are chiral, unidirectional waveguides, and are not affected by disorders. In this chapter, we first describe the translational shift of the rod array from a uniform  $C_{3v}$  crystals to construct

the reconfigured structure. Secondly, we focused on the interface band in valley supercell structure with two different orientations  $\alpha = 30^\circ$  and  $\alpha = -30^\circ$ , respectively. Then, we prepared a reconfigurable supercell from a uniform  $C_{3v}$  symmetry crystal structure, and compare band behavior with others supercell. Finally, based on these supercell structure, we designed both straight and Z-shaped reconfigurable waveguide to observe the transmission efficiency around the topological edge state of valley waveguides.

### **3.2 Symmetry, and Different Type of Symmetry**

The terms crystal and symmetry are obviously connected together. The concept of symmetry describes the repetition of crystal structural features. There are mainly two general types of symmetry exist, and known as (i) internal or translational symmetry, and (ii) external or point symmetry.

#### **Translational Symmetry**

Translational symmetry of an object is defined as the invariance of a system for which that object remains unchanged. Actually, it describes the periodic repetition of a crystal structural feature across a length or through an area or volume. This particular translation changes the location only of an object but the distances, angles, size and shape between points within the figure will not change.

#### **Point Symmetry**

Point symmetry is another type of symmetry that also describes the periodic repetition of a crystal structural feature around a point. Reflection, rotation, and inversion are all known as point symmetries.

#### **Mirror Symmetry**

A mirror symmetry operation is an imaginary operation that can be performed to reproduce an object. The operation is done by imagining that a person cut the object in half, then place a mirror next to one of the halves of the object along the cut. If the reflection in the mirror reproduces the other half of the object, then the object is said to have mirror symmetry. The plane of the mirror is an element of symmetry referred to as a mirror plane.

## **Inversion**

An inversion is one kind of operation where each line is drawn from all points on the object through a point in the center of the object (known as symmetry center). The lines each have lengths that are equidistant from the original points. When the ends of the lines are connected, the original object is reproduced inverted from its original appearance.

### **3.3 Topological Phononic Waveguide, and Reconfigurable Waveguide**

#### **Topological Waveguide**

Topological phononic waveguide is a new class of architected structures that exploits the symmetry and topology of their dispersion surfaces to support modes that are immune to defects, to imperfections, and do not suffer from the scattering losses. This immunity arises as a consequence of topological properties, and hence, these waves are called topologically protected.

#### **Reconfigurable Waveguide**

Acoustic waveguide is necessary to be more efficient and robust against defects and bending as well as reconfigurable toward application to highly integrated switchable device. We presented design of a novel reconfigurable topological waveguide based on the translational shift of metallic rod array, which ensure us even there was the localized mode present in the path of reconfigured waveguide interface, the acoustic wave can still propagate robustly.

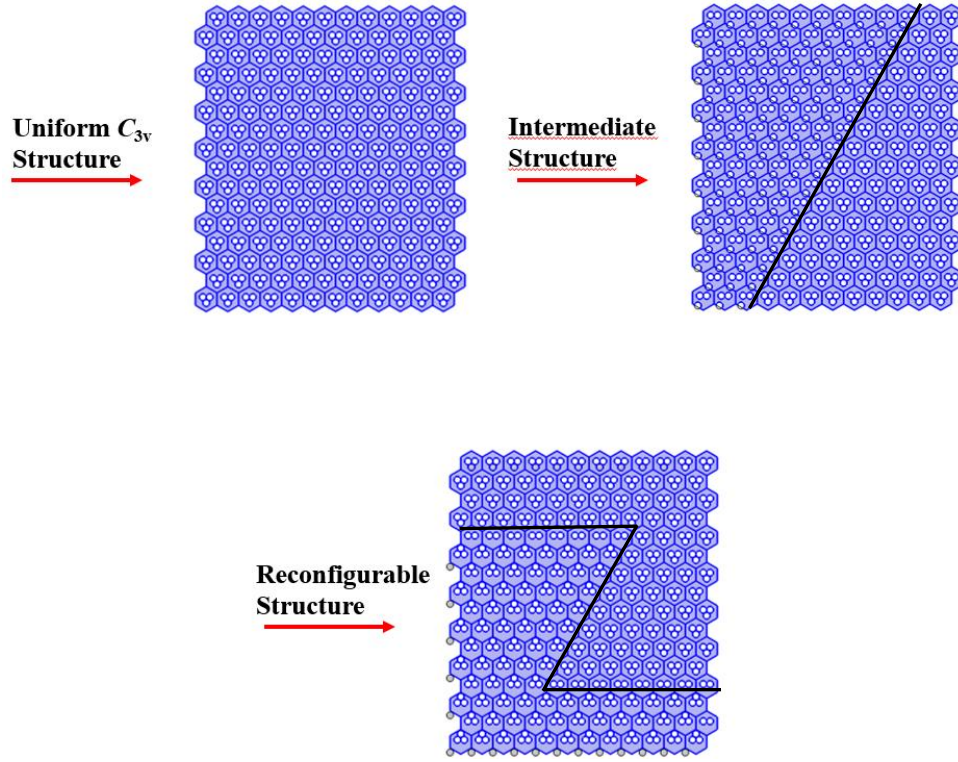


**Fig.3:** Schematic arrangement of reconfigurable structure from a uniform crystal  $C_{3v}$  symmetry structure.

### 3.4 Transmission Coefficient, and Transmission Loss

#### Transmission Coefficient

The transmission coefficient is defined as the ratio of the transmitted particle current and the incident particle current, and will depend on the incident energy (**Source: Semiconductors and Semimetals, 1994**).

or the transmission coefficient represents the probability flux of the transmitted wave relative to that of the incident wave. We apply 1 Pa incident pressure (input) at the left portion to observe the total transmission (output) along the valley and reconfigurable waveguide interface at right portion.

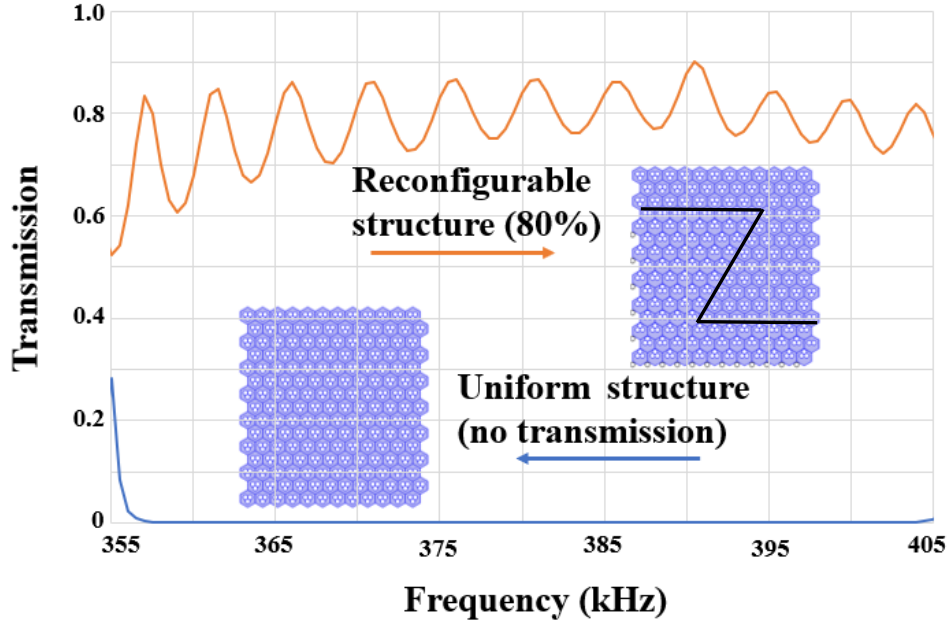


**Fig.4:** Transmission efficiency of reconfigurable structure from a crystal  $C_{3v}$  symmetry structure.

### Transmission Loss

Transmission loss (TL) in general describes the accumulated decrease in intensity of a waveform energy as a wave propagate outwards from a source, or it propagates through a certain area or through a certain type of structure. It is a terminology frequently used in optics and acoustics. Measures of transmission loss are very important in the industry of acoustic devices such as mufflers and sonars. The transmission curve of the above reconfigurable shows almost 10 % loss around 390 kHz because of backscattering length of two corners.

### 3.5 Translational Shift of Rod Array for Symmetry Transformation

Initially, we constructed a uniform  $C_{3v}$  symmetric structure of an array of the unit cell with orientation  $\alpha = 30^\circ$ . Then, we shifted one rod from all layers below the interface to construct  $\alpha = -30^\circ$  oriented rod array in the lower layer using continuous translation  $\vec{T}$ . As a result, the uniform phononic structure is shown to be reconfigured with an interface between the

upward and downward convex with  $C_{3v}$  symmetric structure ( $\alpha = 30^\circ$  in the upper layer and  $\alpha = -30^\circ$  in the lower layer). The continuous translation of the rod leaves a dimer array in the path of the reconfigured interface, as shown in **Figs. 5(a)**, and **5(b)**. The translation vector for shifting rod from the original position to another in a neighboring hexagonal unit cell of the reconfigurable structure can be expressed as  $\vec{T} = \left(-\frac{1}{2}a, -\frac{\sqrt{3}}{2}a + 2\sqrt{3}r\right)$ , where  $r$  is the radius of each circular rod.

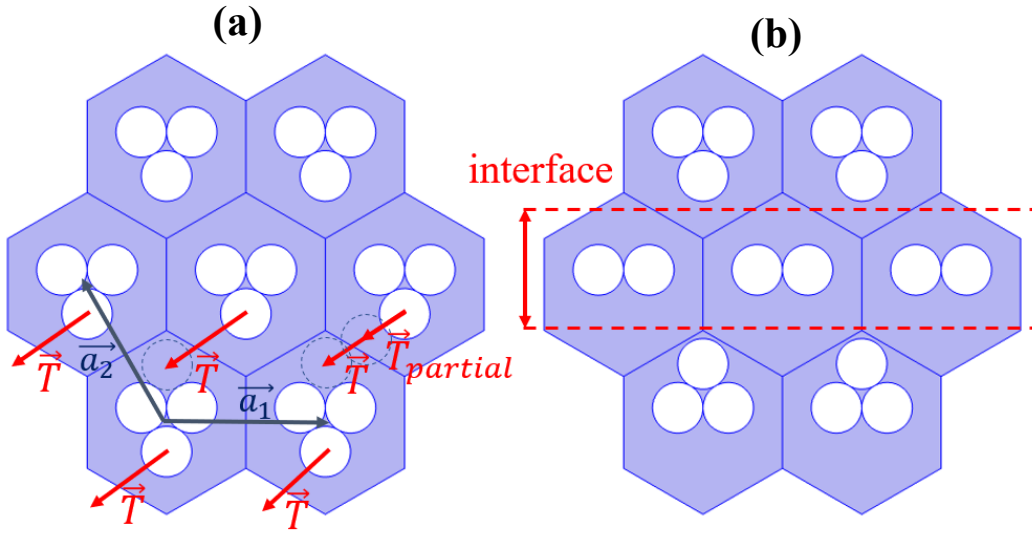


**Fig.5:** (a) Schematic of continuous translation of a rod array in a single phononic crystal, and (b) waveguide structure constructed after the transformation illustrated in (a). (Adopted from M.S. Ali et al. *Jpn. J. Appl. Phys*, 2023)

### 3.6 Interface Band Properties of Supercell

**Figure 6(a)** illustrates supercells with valley PnCs, in which each unit cell is composed of three circular rods in a  $C_{3v}$  symmetry structure with  $\alpha = 30^\circ$  and  $\alpha = -30^\circ$ , as well as their band structure  $k_x$ . The width and height of the supercells are defined as  $a$ , and  $\frac{30a}{\sqrt{3}}$  respectively. The wave vector  $\mathbf{k}$  and angular frequency  $\omega$  gives the dispersion relation for

supercell valley band gap. The wave vector  $\mathbf{k}$  of the dispersion relation in a rectangular two-dimensional supercell can be represented as

$$\begin{cases} \text{if } k < 1, (kx, ky) = \left(\frac{\pi}{a}k, 0\right) \\ \text{if } k < 2, (kx, ky) = \left(\frac{\pi}{a}, \frac{(k-1)}{a}\pi\right) \\ \text{if } k < 3, (kx, ky) = \left(\frac{(3-k)}{a}\pi, \frac{(3-k)}{a}\pi\right) \end{cases} \quad (\text{C})$$

where the irreducible Brillouin zone  $\Gamma \rightarrow X \rightarrow M$  of hexagonal lattice is defined as  $\Gamma(kx, ky) = (0,0)$ ,  $X(kx, ky) = \left(\frac{\pi}{a}, 0\right)$  and  $M(kx, ky) = \left(\frac{\pi}{a}, \frac{\pi}{a}\right)$  respectively.

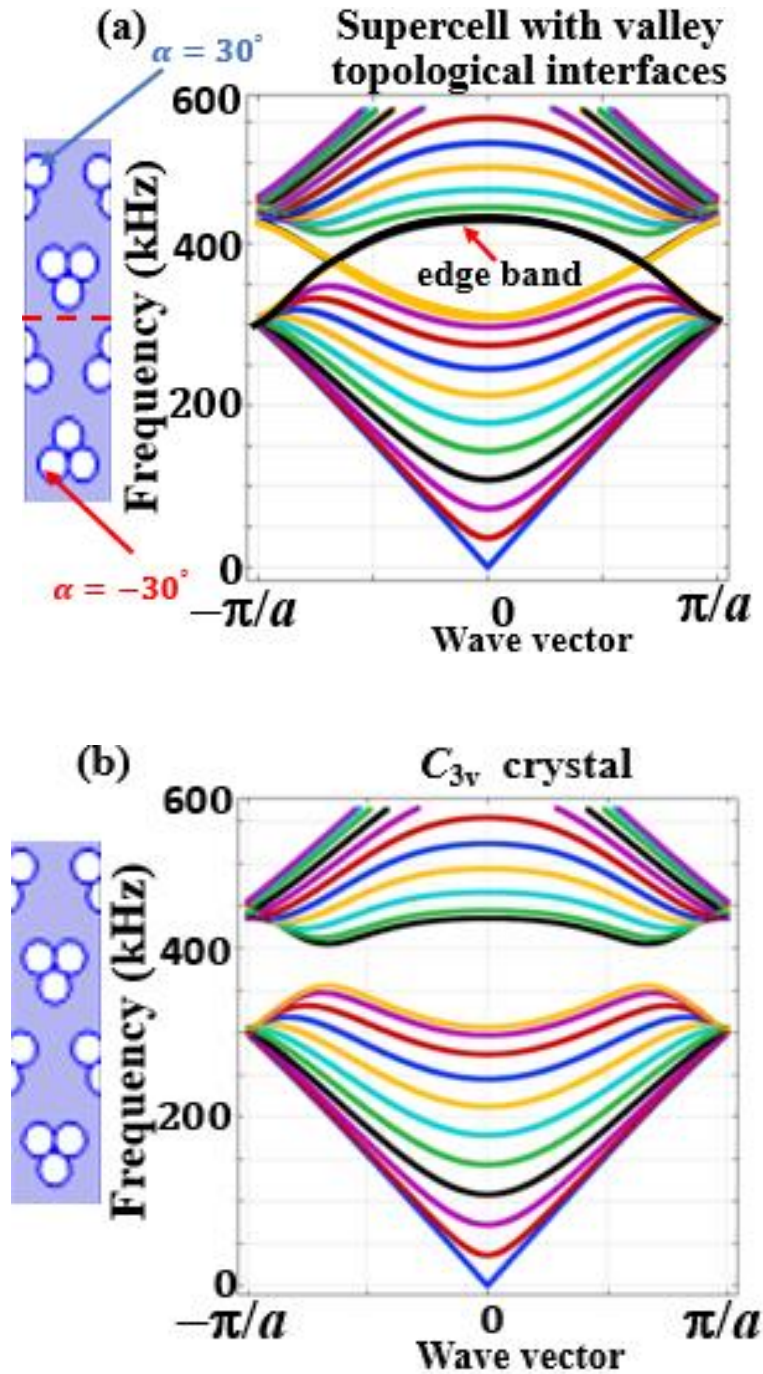
The upper and lower layers, with differently oriented unit cells, were separated by a topological interface. **Figure 6(a)** shows an edge mode around 310–430 kHz where the two pseudo-spin modes appear at the  $K^+$  and  $K^-$  points (near the  $K$  points in the Brillouin zone of a supercell), as expected from the Berry curvature analysis described in the previous section.

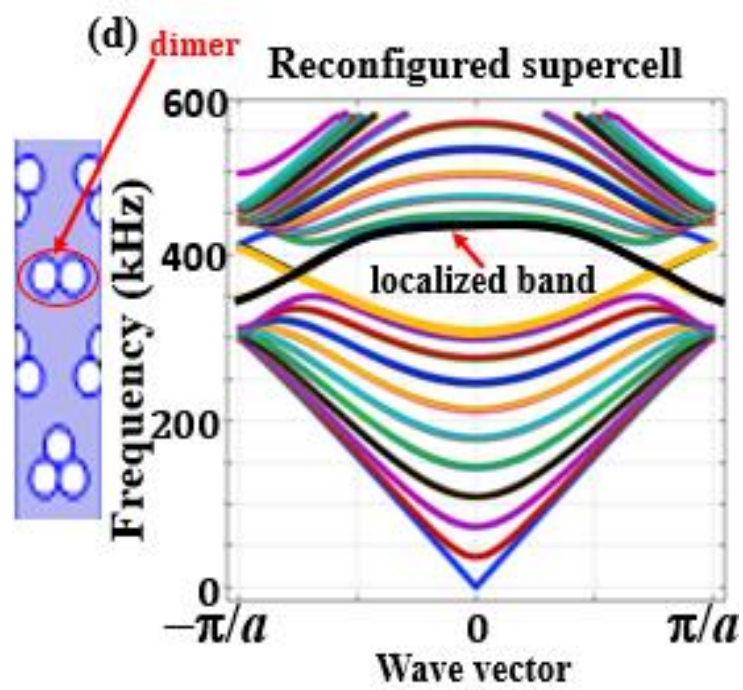
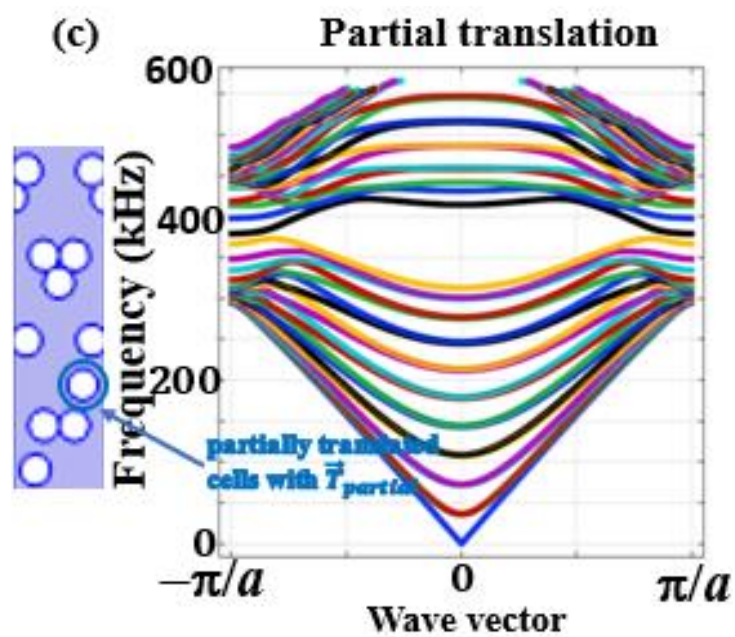
For comparison, the supercell of a single crystal in  $C_{3v}$  symmetry with orientation  $\alpha = 30^\circ$ , as shown in **Fig. 6(b)**, is prepared, where the band gap appears around 356–405 kHz. **Figure 6(c)** depicts a supercell with partially shifted rods in the unit cell, where one rod was shifted in all the unit cells below the interface with translation vector  $\vec{T}_{\text{partial}} = \left(-\frac{a}{4}, -\frac{\sqrt{3}}{2}a + \frac{5\sqrt{3}}{2}r\right)$ , where  $r$  is the radius of each circular rod. A pressure field analysis on each band in **Fig. 6(c)** reveals that modes in the upper and lower band than the narrow band gap around 375–380 kHz is localized around the interface between two PnCs.

Further continuous translation to  $\delta\vec{T} = \left(-\frac{1}{4}a, -\frac{\sqrt{3}}{2}r\right)$  leads to a structural transformation from the original PnC with  $\alpha = 30^\circ$  to the one with  $\alpha = -30^\circ$  in the lower layer, as depicted in **Fig. 6(d)**. We found that the band above 380 kHz near the  $K$  points is regarded as a bulk band, whereas the lower band than the frequency near the  $K$  points corresponds to a localized mode attributed to the presence of a dimer array at the interface. This can impact not only the wave transmission because of the localization of the mode, but also the band topology. Continuous translation breaks the local  $C_{3v}$  symmetry and creates a band gap, but the edge



state may not necessarily appear around this frequency. Additionally, the continuous translation of the rods leaves a dimer array at the interface, creating a localized/defect mode and resulting in less energy transfer in the reconfigurable waveguide.





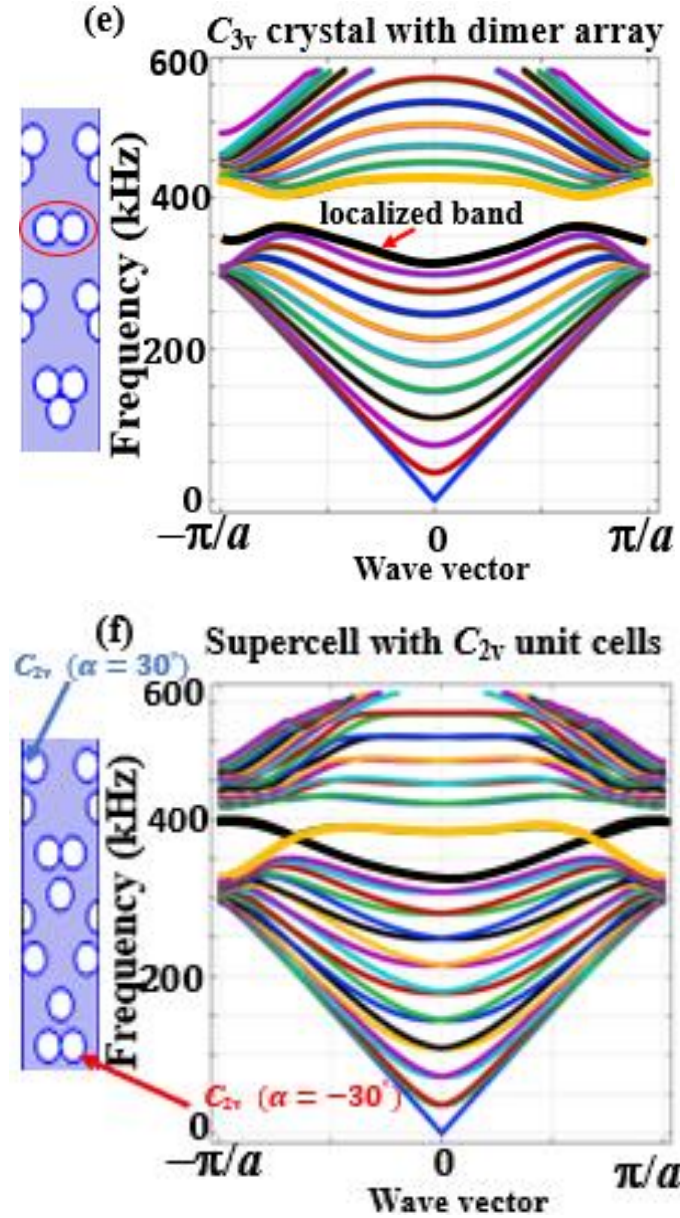
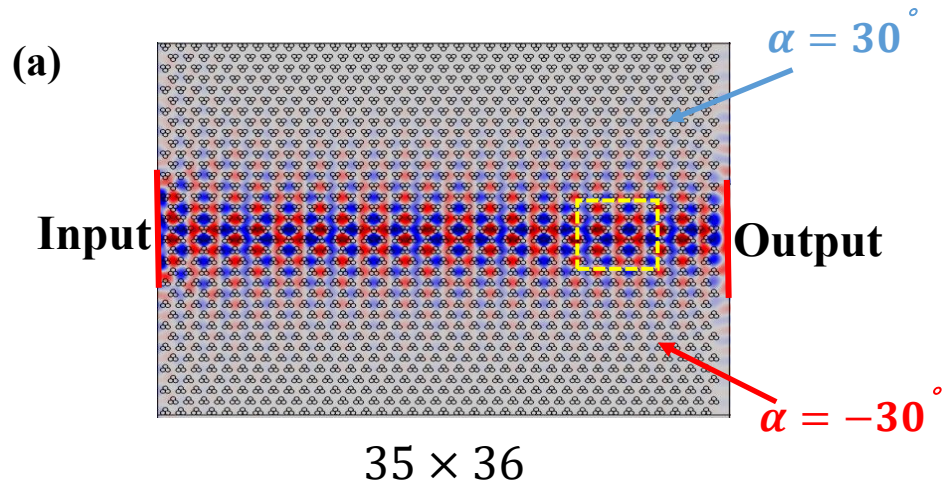


**Fig.6:** (a) Supercell structure and band diagrams of (a) a valley PnC with  $\alpha = 30^\circ$  and  $\alpha = -30^\circ$ , (b) a PnC of uniform  $C_{3v}$  unit cells with  $\alpha = 30^\circ$ , (c) supercell structure with partially shifted unit cells, (d) supercell with an interface between  $\alpha = 30^\circ$  and  $\alpha = -30^\circ$  reconfigured from the structure in (b) leaving a dimer array, (e) a PnC of uniform  $C_{3v}$  unit cells with  $\alpha = 30^\circ$  with dimer array inserted, and (f) supercell with an interface between two oppositely oriented ( $\alpha = 30^\circ$  and  $-30^\circ$ )  $C_{2v}$  unit cells (generated by vertical shift with 0.3 mm) (Adopted from M.S. Ali et al. *Jpn. J. Appl. Phys*, 2023).

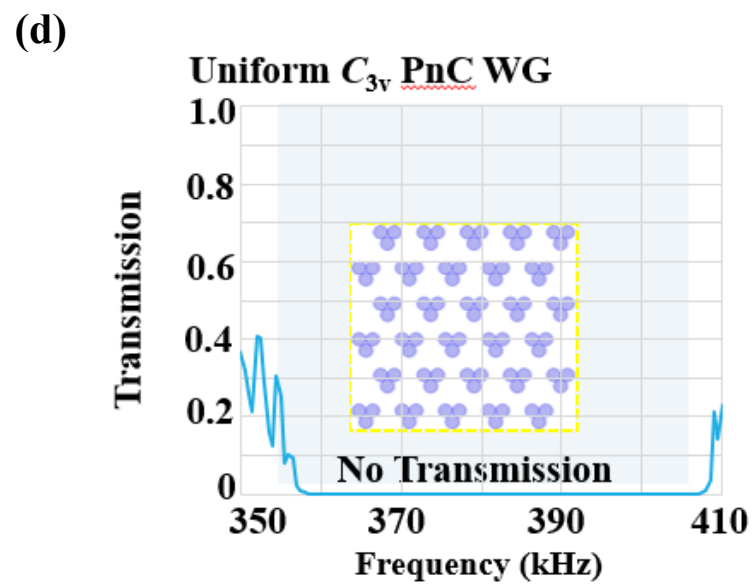
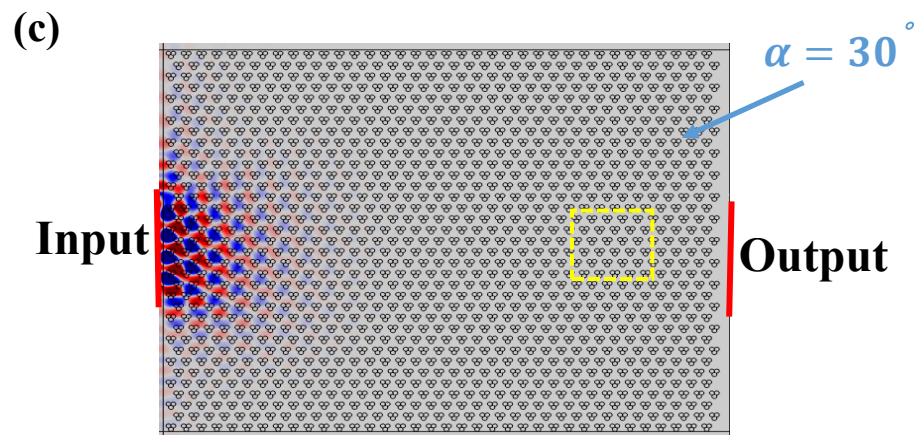
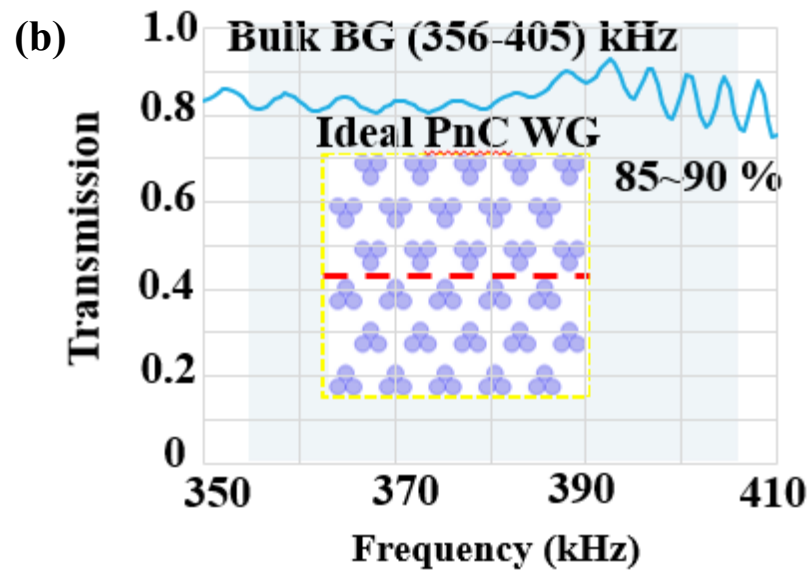
In **Fig. 6(e)**, we show another supercell structure with  $\alpha = 30^\circ$  with one dimer array inserted into the structure to eliminate this localized mode effect. The nature of the flat band depicted at approximately 350 kHz near the K points in **Fig. 6(e)** corresponds to the mode localized around the interface. **Figure 6(f)** shows that the band gap appears when a circular stainless-steel rod is vertically shifted by 0.3 mm from each unit cell, and the local  $C_{3v}$  symmetry is reduced to  $C_{2v}$  symmetry. A pressure distribution analysis shows that the upper band at 380 kHz and lower band than the frequency near the K points are the localized band and bulk band, respectively. No edge state appears in the original gap frequency because the localized mode has a dominant effect in this frequency region. Based on these characterizations, we constructed valley phononic and reconfigurable phononic waveguides, which will be discussed in the following sections, to observe the robustness of wave propagations via the topologically protected edge state.

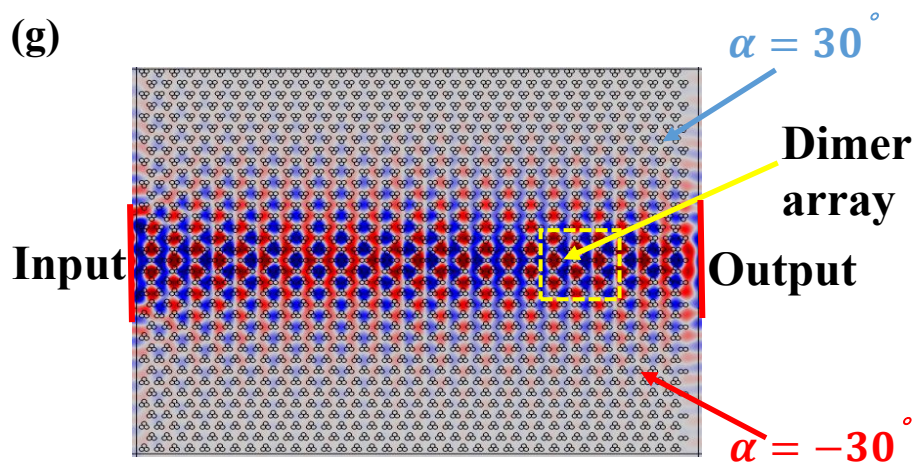
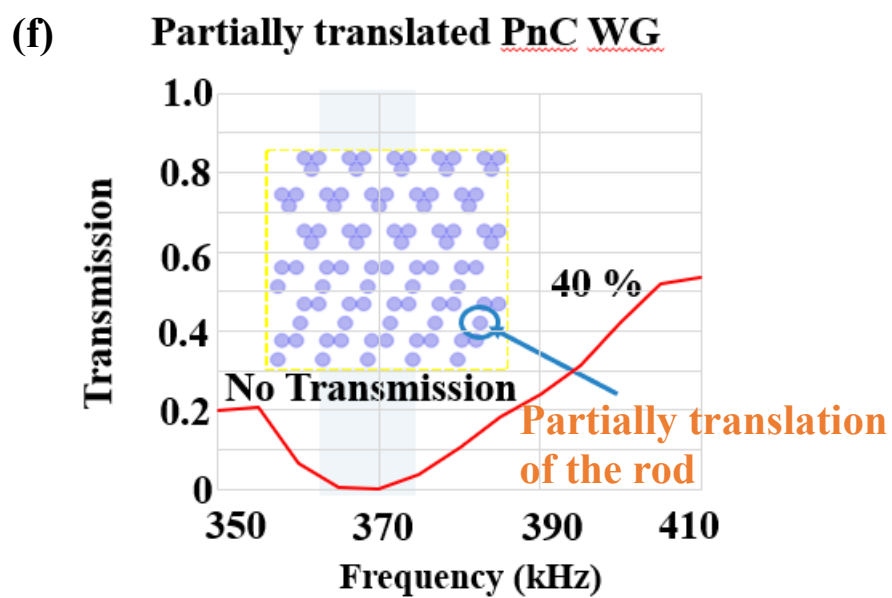
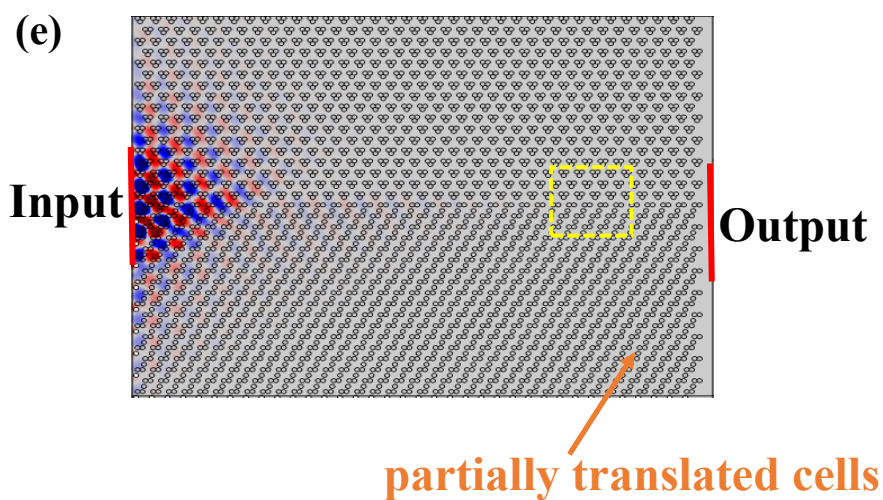
### 3.7 Transmission Properties of Topological Waveguide

One of the most important properties of topological wave devices is their robustness, as well as their ability to control the wave transmittance in the waveguide via the topological edge state. Based on the band structure design previously described, in this section, we examine the transmission properties of waveguides with various interface structures (**Fig. 7**) and the transmission spectra (**Fig. 8**).









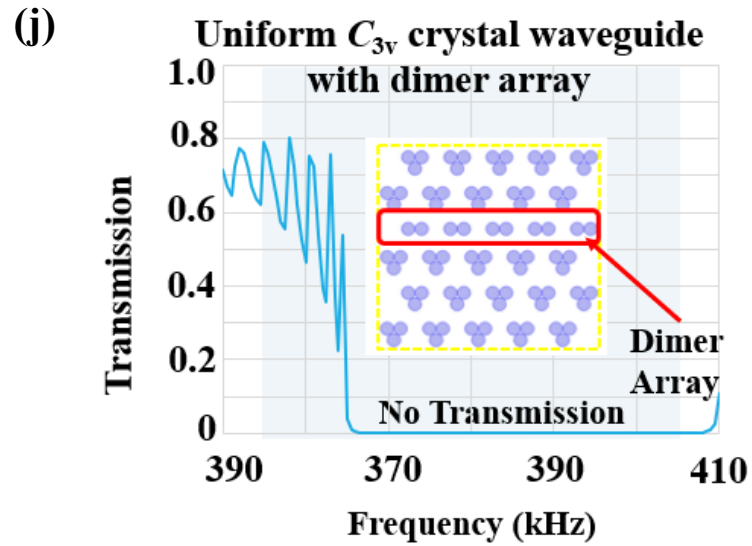
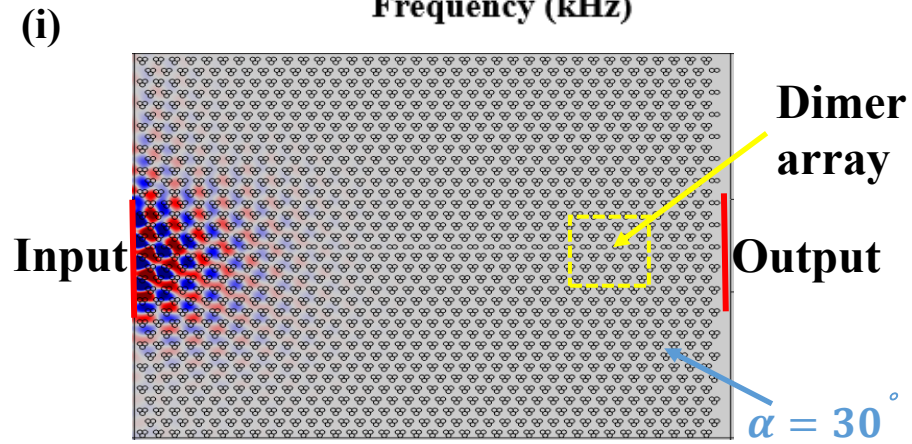
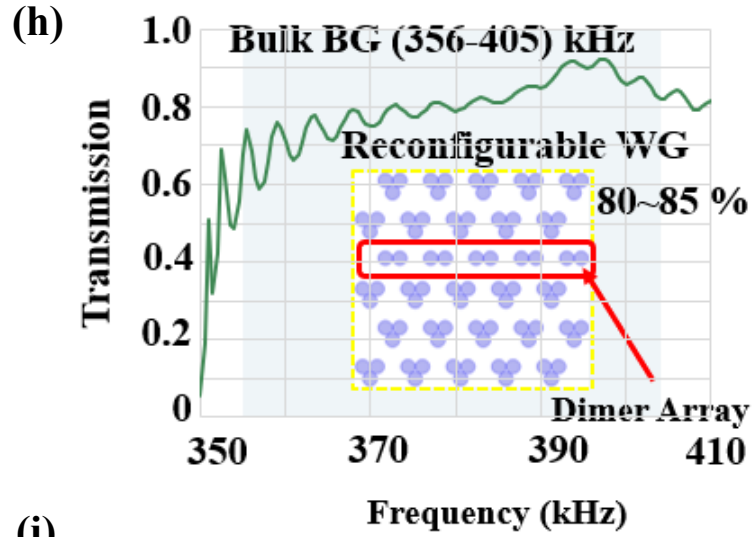


**Fig.7:** (a-b) Normalized pressure field and transmission in valley phononic straight waveguide, (c-d) Normalized pressure field at 400 kHz and transmission for a uniform phononic waveguide, (e-f) Normalized pressure field at 370 kHz and transmission for a  $C_{2v}$  breaking symmetric (partial translation) waveguide, (g-h) Normalized pressure field at 400 kHz and transmission in reconfigurable phononic waveguide, and (i-j) Normalized pressure field at 400 kHz and transmission for a uniform structure waveguide due to localized mode effect (Adopted from M.S. Ali et al. Jpn. J. Appl. Phys, 2023).

### 3.8 Straight Waveguide

First, we prepared a valley topological straight waveguide with  $35 \times 36$  rectangular arrays of unit cells in  $C_{3v}$  symmetry with two different orientations,  $\alpha = 30^\circ$  and  $\alpha = -30^\circ$ , respectively, and immersed in water. We used two integration operators to determine the average pressure at the left and right side of this waveguide. At the left and right portion, the input (incident, 1 Pa) background pressure field and the output pressure field were defined. The total output pressure field exists if and only if the background pressure field become zero. We were set Floquet periodic boundary conditions on the top and bottom portion of the waveguide. The wave vector  $k_x$  and  $k_y$  in x and y direction can be expressed as

$$\begin{cases} k_x = 2\pi f_{\max}/c_w \\ k_y = 0 \end{cases} \quad (D)$$

where  $f_{\max}$ , and  $c_w$  represents the derived frequency and water speed of sound, respectively.

Also, we defined the height of perfectly match layer for both left and right side. We have used the following variable to represent the transmission coefficient, and transmission loss

Table 2: The variable parameters for input and output pressure field

Name	Expression	Description
T	$\text{aveop2}(\text{abs}(\text{acpr.p}_t)^2)^{0.5}/\text{aveop1}(\text{abs}(\text{acpr.p}_b)^2)^{0.5}$	Transmission coefficient
TL	$-20 \cdot \log_{10}(\text{abs}(T))$	Transmission Loss



where aveop1, aveop2, acpr\_t, and acpr\_b represents the average over a boundary at left and right portion, total acoustic pressure field, and background pressure field, respectively. To define the pressure field region, we have used two polygons with the following coordinate values.

Table (3): polygon 1 (Input/background pressure field)

x(m)	y(m)
-0.0396	0.008
-0.0433	0.008
-0.0433	-0.008
-0.0396	-0.008

Table (4): polygon 2 (output pressure field)

x(m)	y(m)
0.0418	0.008
0.0455	0.008
0.0455	-0.008
0.0418	-0.008

Then, we observe the transmittance and total pressure field of the  $C_{3v}$  symmetric straight waveguide along the interface. **Figure 7(a)** shows the waveguide structure along with the pressure field distribution when an incident acoustic wave of 1 Pa at 400 kHz was input from the left port region and the transmittance was measured at the right (output). In **Fig. 7(b)**, the curve clearly shows that efficient wave transmission is realized around the bulk band-gap frequency range of 356–405 kHz, based on the band structure design in the previous section.

### 3.9 Reconfigurable Straight Waveguide

First, we prepared  $35 \times 36$  rectangular arrays of uniform phononic  $C_{3v}$  crystal structures with a single orientation  $\alpha = 30$  to show that a topological waveguide can also be constructed by the continuous translation of the rod arrays proposed in the previous section. We observed the pressure field along this uniform waveguide, as illustrated in **Fig. 7(c)** at 400 kHz. No transmission is observed in this frequency range of 356–405 kHz, because no edge state appears, as depicted by the curve in **Fig. 7(d)**.

We partially shifted one rod from each unit cell in all below layers using continuous translation  $\vec{T}_{\text{partial}}$ . Consequently, a symmetry-broken waveguide was constructed at the interface between the layers with and without partial translations. If we apply 1 Pa incident pressure at left portion, then the partial shifted waveguide shows scattered propagation at the right portion, as shown in **Fig. 7(e)**, at 400 kHz. Also, the curve in **Fig. 7(f)** shows very low transmission in the frequency range of 365–375 kHz.

The PnC layer with  $\alpha = -30^\circ$  oriented array is constructed by further continuous translation of the rod with  $\delta\vec{T}$  from below the interface. Thus, the uniform phononic structure is reconfigured to a waveguide with an interface between upward and downward convex with  $C_{3v}$  symmetric structure ( $\alpha = 30^\circ$  in the upper layer and  $\alpha = -30^\circ$  in the lower layer). The total translation vector for one shifted stainless-steel rod from the initial position to the reconfigured position was  $\vec{T}$  defined in Sec. 2.1. It should be noted that the continuous translation of rod leaves a dimer array with  $C_{2v}$  local symmetry in the waveguide, as illustrated in **Fig. 1(b)**. **Figure 7(g)** depicts the reconfigured waveguide along with the pressure field distribution in the case where an incident acoustic wave at 400 kHz is input from the left port, and the transmittance is measured at the output port at the right exit of the waveguide. We observed almost the same transmission of the reconfigured interface as that of the original valley topological waveguide, as depicted by the blue curve in **Fig. 7(h)**.

We constructed  $35 \times 36$  rectangular arrays of stainless-steel rod unit cells with  $C_{3v}$  symmetry structure with  $\alpha = 30^\circ$  orientation, as shown in **Fig. 7(i)**, to determine the effect of the localized mode (defect) because of the dimer array left after the translational shift. No transmission was observed along this interface region of the  $C_{3v}$  crystal with the dimer array waveguide, as shown by the red curve in **Fig. 7(j)**, revealing that the presence of the dimer array alone cannot generate a localized mode that contributes to the transmission observed in the reconfigured waveguide in **Fig. 7(h)**.

### 3.10 Transformation to $C_{2v}$ Symmetric Interface

In this section, we examine the effect of another translation on transmission properties. The position of a stainless-steel rod in the original  $C_{3v}$  unit cell was vertically shifted by  $\delta y = -0.3$

mm from its original position. Subsequently, the original symmetry  $C_{3v}$  in the unit cell is reduced to  $C_{2v}$ . The above ( $\alpha = 30^\circ$ ) and below ( $\alpha = -30^\circ$ ) layers with  $C_{2v}$  symmetry were separated by a straight interface. Therefore, another type of phononic waveguide is constructed, as shown in **Fig. 8(a)**. We observed the output pressure field and the transmittance with respect to the incident wave at 400 kHz. In **Fig. 8(b)**, no transmission occurs in the frequency range 390–430 kHz, indicating that no edge state is observed within the frequency range.

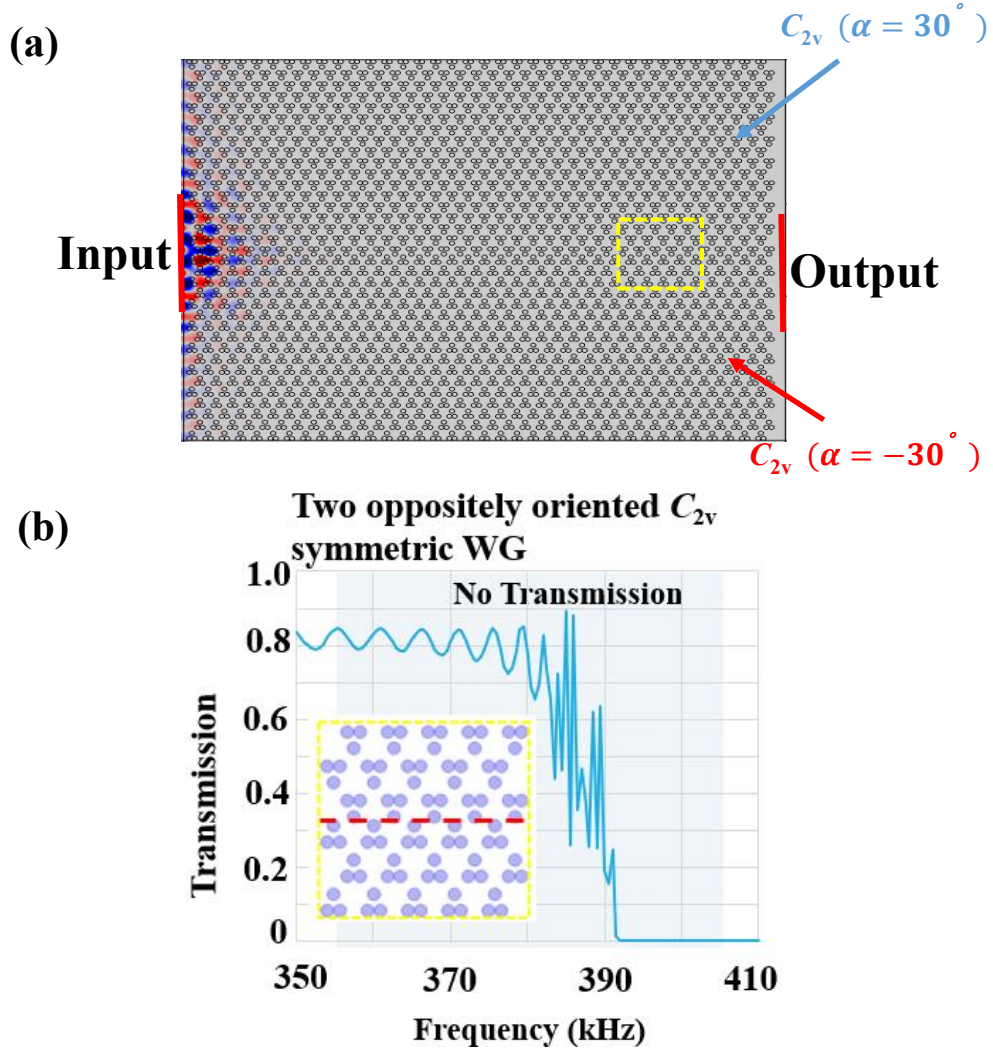


**Fig.8:** (a) Normalized pressure field at 400 kHz, and (b) transmission for broken  $C_{2v}$  symmetry (when  $\alpha = 30^\circ$  and  $\alpha = -30^\circ$ ) waveguide (Adopted from M.S. Ali et al. Jpn. J. Appl. Phys, 2023).

### 3.11 Z- Shaped Waveguide

We examined the transmission analysis for a Z-shaped waveguide that involves two corners, in which a large portion of transmission loss can be attributed to the propagation path, to demonstrate that the robustness can also be preserved by the present scheme of reconfiguration [39]. We arranged  $27 \times 18$  rectangular array of unit cells with  $C_{3v}$  symmetry with two differently oriented rod arrays,  $\alpha = 30^\circ$  and  $\alpha = -30^\circ$ , respectively, in a two-dimensional hexagonal lattice and embedded in water. Then, we constructed a Z-shaped interface, as shown in Fig. 9(a), which is indicated by the white dotted lines. The lengths of both the upper and lower horizontal interfaces were  $10 \times a = 22$  mm and  $-10 \times a = -22$  mm, respectively, whereas the length of the oblique interface was  $\frac{12 \times a}{\sqrt{3}} = 15.242$  mm. We highlighted again the input (incident, 1 Pa) background pressure field at left portion. The output pressure field was defined at the right portion. The interface region has defined with the help of two polygons. The interface region has defined with the help of two polygons. The interface region is given in the below table 4 and 5.

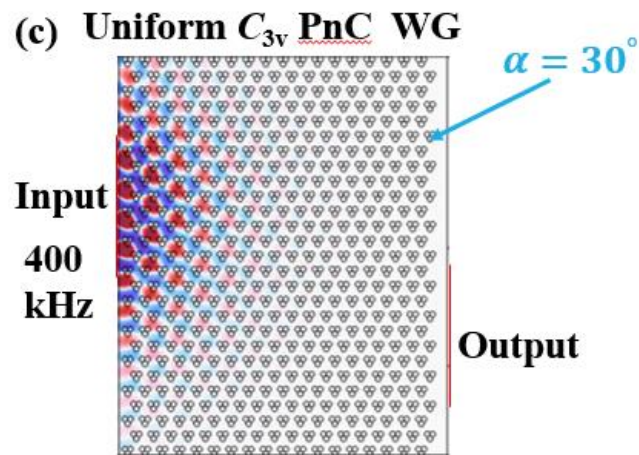
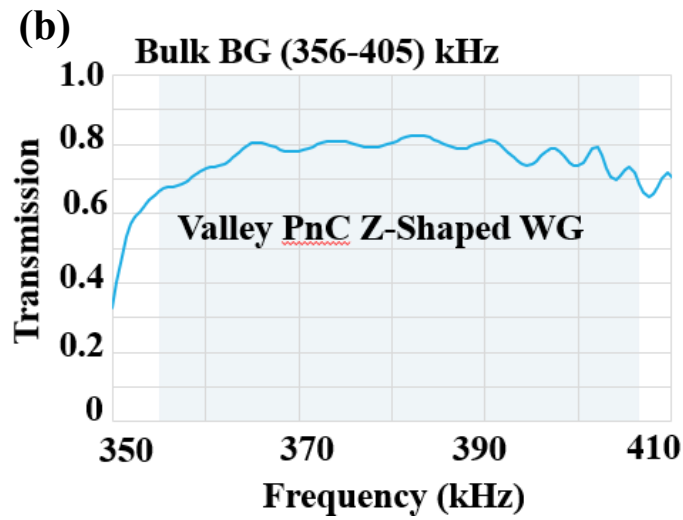
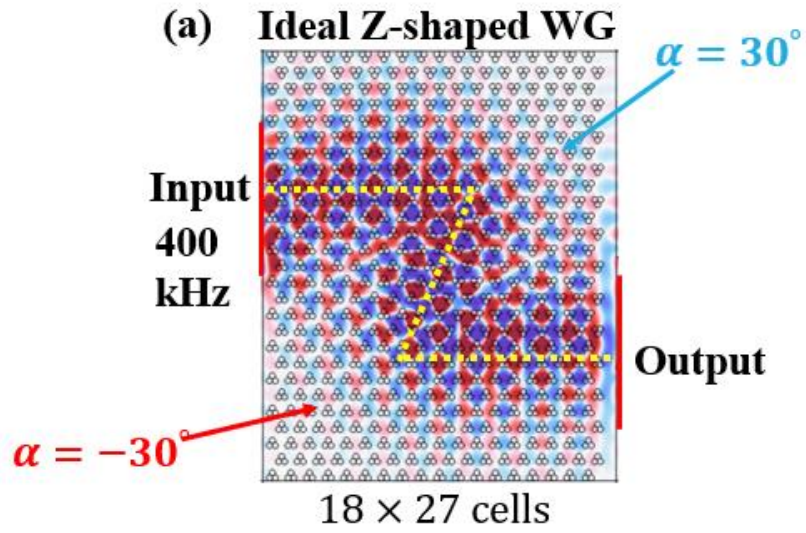
Table (4): polygon 1 (left portion of the interface)

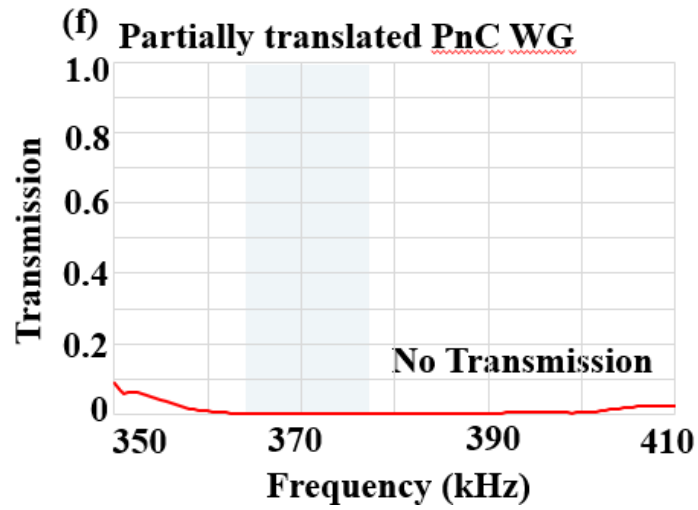
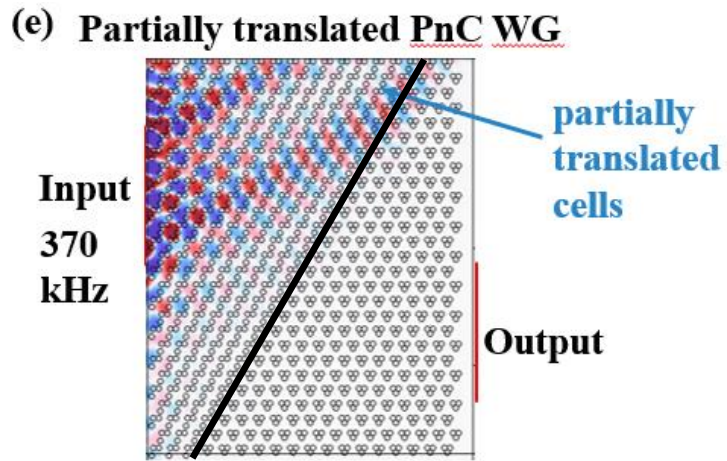
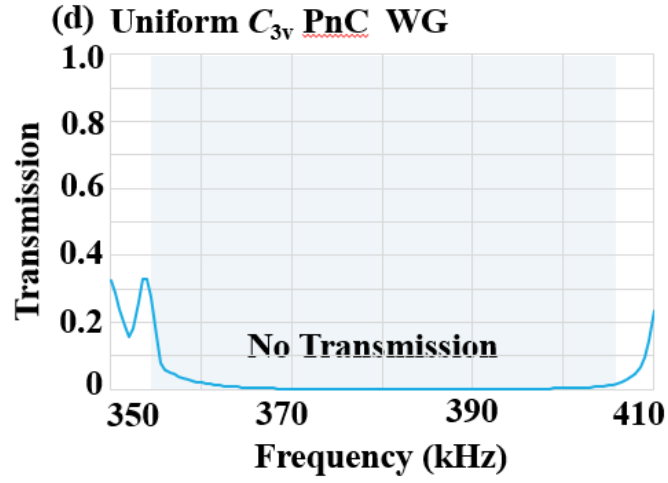
x(m)	y(m)
-0.0198	0.014
-0.0226	0.014
-0.0226	-0.001
-0.0198	-0.001

Table (5): polygon 2 (right portion of the interface)

x(m)	y(m)
0.0220	0.001
0.0248	0.001
0.0248	-0.014
0.0220	-0.014

The waveguide structure and the pressure field distribution for an incident acoustic wave at 400 kHz are shown in **Fig. 9(a)**. It exhibits efficient wave transmission ( $\sim 80\%$ ) within the frequency range of 356–405 kHz, as denoted by the curve in **Fig. 9(b)**.





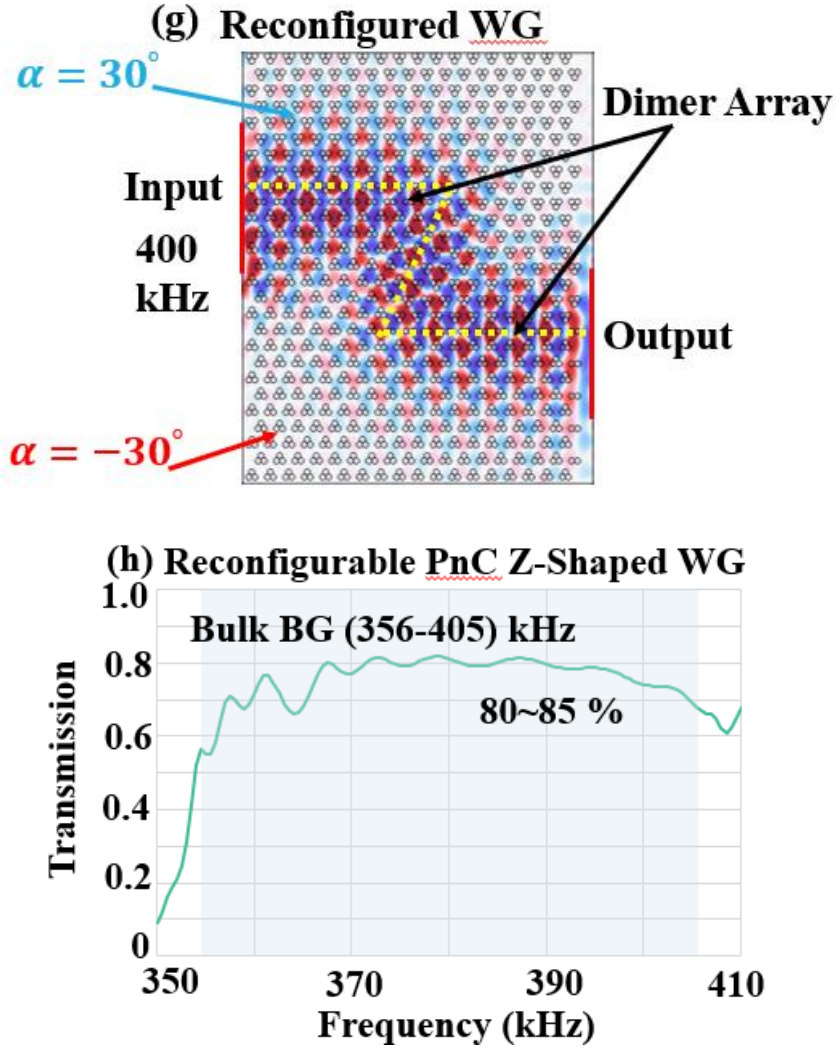


**Fig.9:** (a) Normalized pressure fields in a valley phononic Z-shape waveguide (WG), (b) transmission spectrum in valley phononic Z-shaped, (c-d) Normalized pressure fields and transmission spectrum in uniform phononic crystal WG at 400 kHz, and (e-f) Normalized pressure fields and transmission spectrum for partially translation of rod waveguide, and (g-h) Normalized pressure fields and transmission spectrum in reconfigured Z-shaped WG (Adopted from M.S. Ali et al. Jpn. J. Appl. Phys, 2023).

### 3.12 Z- Shaped Reconfigurable Waveguide

We also constructed a Z-shaped waveguide in a reconfigurable manner, as discussed in

Section 2.2. Initially, we constructed a  $27 \times 18$  rectangular array of unit cells with a uniform  $C_{3v}$  symmetric structure and  $\alpha = 30^\circ$  orientation and immersed them in water. We see no propagation occurs along the edge state, as depicted in the **Fig.9(c-d)**. Then, we shift one rod partially  $\vec{T}_{partial}$  for all the layers at the left portion of the waveguide (as an intermediate state). But still wave cannot propagate along the edge state frequency, as shown in the **Fig.9(e-f)**. Further continuous translation of the rod, the  $C_{3v}$  symmetric unit cell with  $\alpha = -30^\circ$  is created and separated from  $\alpha = 30^\circ$  in the right-half layer by an oblique interface. We changed the current position of the top nine layers by translating  $-\vec{T}$  to construct an  $\alpha = 30^\circ$  oriented unit cell. In addition, we also changed the current position of the bottom nine layers with  $\vec{T}$ . Consequently, the uniform valley phononic structure with  $C_{3v}$  symmetry was reconfigured to a Z-shaped waveguide, as shown in **Fig.9(g)**. We observed the pressure field and the same wave transmittance along this interface region in the reconfigured Z-shaped waveguide. It is worth noting that the continuous translation of the rod leaves a dimer array, breaks the local symmetry, and slightly degrades the pressure field intensity in the Z-shaped path, as denoted by the orange curve in **Fig. 9(h)**.



## Chapter 4

### **Active Control of Localized Mode and Transmission in Valley Z-Shaped Topological Phononic Waveguides by Non-Hermitian Modulation**

#### **4.1 Introduction**

This chapter lies at one such theoretical (numerical) frontier, the analyses of novel approach of phononic lattices with air lossy beyond the Hermite system. In recent years, non-Hermitian systems have shown great interest due to their intriguing dynamical and topological properties [1-8] within both classical and quantum physics [9-14]. A number of insights and concepts originally developed for quantum wave functions have been fruitfully applied to electromagnetic fields; examples include, but are not limited to, the invention of photonic crystals as electromagnetic analogs of electronic band insulators [15-16]; the development of parity/time reversal (PT) symmetric photonics based on a hypothetical non-energy-conserving formulation of quantum mechanics [17]; and the development of photonic devices that mimic topological insulators and other topological phases of matter [18-19]. Moreover, parity- time (PT) symmetry, one of the major discoveries in non-Hermitian quantum physics, claims that a class of non-Hermitian Hamiltonians with PT symmetry can still have real spectra [20]. On the other hand, many researchers have been a lot of efforts in constructing topological states in non-Hermitian systems [21-24]. Although the topology of band structure concept was originally formulated for Hermitian system, but recently the band topology in non-Hermitian system has been the focus of much attention. In the 2000s, researchers began investigating the properties of non-Hermitian band structures in earnest, starting with the study of PT symmetric optical waveguide arrays [25-29], and continuing into lattices obeying other non-Hermitian symmetries [30]. The concept of topological phases has been extended to non -Hermitian system in which the interplay between band topology and non-Hermiticity leads to rich topological features with no Hermitian counterpart [31-34]. Non-Hermitian modulated metamaterials exhibit asymmetric transmission and reflection scattering phenomena [35-37]. Besides, given that the realization of gain is more challenging

to achieve than that of loss, passive non-Hermite systems without gain have been proposed; these systems can exhibit similar physical, extreme asymmetric absorption phenomena [38-39]. Essentially, we need to active control of the amount of degradation of the robustness in a waveguide interface. Recently, such degradation of robustness in the presence of corner has been quantitatively evaluated in terms of the “backscattering length” in valley photonic waveguides [40-42]. However, we proposed an opposite way: By increasing losses rather extremely, we demonstrate that the transmission losses mainly due to the localized modes can be effectively extinct.

We prepared two-dimensional hexagonal structure, composed of three circular holes filled by air, and embedded in polydimethylsiloxane (PDMS). PDMS is an elastomeric polymer with interesting mechanical properties and excellent optical transparency that can be easily fabricated at very low pressures. In terms of mechanical properties, PDMS can also be regarded as an ideal isotropic and homogeneous material (with a sound velocity closer to that of water and smaller shear stresses than those of solids) that can stably sustain holes filled by gaseous matter. Thus, we used a model system with PDMS, assuming that the longitudinal acoustic modes could be separated distinctly and excited independently from other transverse modes, thus simplifying our examination by focusing only on the pressure acoustics for wave-mechanical analyses. The numerical result shows the localized modes within the phononic band gaps in Hermitian system, whereas the strong loss effect in non-Hermitian can lead to vanish these modes. We also analysed the interface band property in a super cell with the large loss effects of the non-Hermitian modulation. We observed the total output pressure field as well as transmission along a Z-shaped waveguide constructed by the interface between two oppositely oriented phononic crystals for both Hermite, and non-Hermite regimes.

## 4.2 Hermitian System, and non-Hermitian System

The longitudinal pressure acoustic equation in Hermitian system is

$$\nabla \cdot \left( -\frac{1}{\rho} \nabla p \right) - \frac{1}{\rho} \left( \frac{\omega}{c} \right)^2 p = Q$$

where the parameter  $\mathbf{c}$  represents the speed of sound of the material. For the air material, the speed of sound in the above equation represents as  $\mathbf{c} = c_{air}$ . As a result, the above equation can be written as

$$\nabla \cdot \left( -\frac{1}{\rho} \nabla p \right) - \frac{1}{\rho} \left( \frac{\omega}{c_{air}} \right)^2 p = Q$$

To implement the loss effects on fluidic materials filled in the circular hole, we adapted a model in which the speed of sound ( $c_{air}$ ) was replaced by the complex parameter  $c_l = c_{air}(1 + i\gamma)$ ; where  $\gamma$  represents the non-Hermitian modulation.

Then, the above equation with lossy air (in non-Hermitian system) will take the following form

$$\nabla \cdot \left( -\frac{1}{\rho} \nabla p \right) - \frac{1}{\rho} \left( \frac{\omega}{c_l} \right)^2 p = Q$$

$$\text{or, } \nabla \cdot \left( -\frac{1}{\rho} \nabla p \right) - \frac{1}{\rho} \left( \frac{\omega}{c_{air}(1 + i\gamma)} \right)^2 p = Q \quad (\text{E})$$

We can simplify,

$$\begin{aligned} \left( \frac{\omega}{c_{air}(1 + i\gamma)} \right)^2 &= \left( \frac{\omega}{c_{air}} \right)^2 \left[ \frac{-2i\gamma + (1 - \gamma^2)}{(1 - \gamma^2)^2 + 4\gamma^2} \right] \\ &= -i \left( \frac{\omega}{c_{air}} \right)^2 \left\{ \frac{2\gamma}{(1 - \gamma^2)^2 + 4\gamma^2} \right\} + \left( \frac{\omega}{c_{air}} \right)^2 \left\{ \frac{(1 - \gamma^2)}{(1 - \gamma^2)^2 + 4\gamma^2} \right\} \end{aligned}$$

Therefore,

$$\nabla \cdot \left( -\frac{1}{\rho} \nabla p \right) - \frac{1}{\rho} \left[ -i \left( \frac{\omega}{c_{air}} \right)^2 \left\{ \frac{2\gamma}{(1 - \gamma^2)^2 + 4\gamma^2} \right\} + \left( \frac{\omega}{c_{air}} \right)^2 \left\{ \frac{(1 - \gamma^2)}{(1 - \gamma^2)^2 + 4\gamma^2} \right\} \right] p = Q$$

This is desired non-Hermitian lossy eigenvalue problem. The second term in the above equation clearly shows the eigenvalue in non-Hermitian lossy system is complex.

Based on this non-Hermiticity lossy parameter  $\gamma$ , we described the Hermitian and non-Hermitian system. The  $2 \times 2$  order matrix of the following form

$$H = \begin{pmatrix} \alpha & \gamma \\ \gamma^* & \alpha \end{pmatrix}$$

that guarantees the existence of real eigenvalues and an orthonormal set of eigenvectors. The steady states in closed system where the energy and probability of a Hamiltonian are conserved (Hamiltonian are Hermitian), called Hermitian system.

On the other hand, the following  $2 \times 2$  order matrix

$$H' = \begin{pmatrix} \alpha & \gamma \\ \gamma' & \alpha \end{pmatrix}; \text{ where } \gamma' \neq \gamma^*$$

that guarantees the existence of complex eigenvalues and set of skewed eigenvectors. An open system where the Hamiltonian is non- conserved (Hamiltonians are not Hermitian), known as non-Hermitian system, balanced with gain and loss.

### **4.3 Parity-Time (PT) Symmetric, and Exponential Point (EP)**

#### **Parity-Time (PT) Symmetric**

Symmetries are essential for understanding and describing the physical world [43]; they give rise to the conservation laws of physics, lead to degeneracies, control the structure of matter, and dictate interactions. Parity-time symmetric is identified as a form of pseudo-Hermiticity with a Hamiltonian that satisfies the condition  $(PT)H(PT)^{-1} = H^t$ , where P and T are respectively the parity and time-reversal operators.

#### **Exponential Point (EP)**

An exceptional point are spectral singularities in the parameter space of a system in which two or more eigenvalues, and their corresponding eigenvectors, simultaneously coalesce. Such degeneracies are peculiar features of non-conservative system, where gain and loss can be perfectly balanced.

### **4.4 Evanescent Waves**

"Evanescent" means "tending to vanish", which is appropriate because the intensity of evanescent waves decay exponentially (rather than sinusoidally) with distance from the interface at which they are formed. According to Dr. Rüdiger Paschotta (an expert in

photonics technology, Switzerland), evanescent waves are waves with a rapidly decaying amplitude and no transport of energy. Evanescent wave occurs in various situation, and have a range of applications in photonics, phononics as well as acoustic.

#### 4.5 Dispersion Relation and Topological Transition

Initially, we prepared two-dimensional hexagonal unit cell structure based on valley topological phononic crystals, which is composed of three circular holes, filled by air and periodically embedded in PDMS, as illustrated in **Fig.10(a)**. We set the following parameter  $a = 2.2$  mm and  $d = 0.7$  mm that defines the lattice constant and diameter of each hole respectively. The speed of sound and mass density of air are 343 m/s and 1.293 kg/m<sup>3</sup>, respectively. Also, we define the speed of sound 1000 m/s and density 1030 kg/m<sup>3</sup> for PDMS. The relative orientation ( $\alpha$ ) of the rod array in the hexagonal lattice characterizes the symmetry of the structure. At the angle  $\alpha = -30^\circ$ , the unit cell band structure in Hermite regime ( $\gamma = 0$ ) illustrated in **Fig.10(b)**, shows two non-trivial dispersive propagating bands (the red lines) whose valley Chern indices [44] at the K point are estimated to be  $\pm 1/2$ , as shown in the **Fig.10(e)** [45-46]. The band gap, which lies in the frequency range of 438–545 kHz, is between the upper and lower dispersive bands. As  $\alpha$  changes to flip the crystal orientation, the band shape is also observed to flipped at  $\alpha = 30^\circ$ , as depicted in **Fig.10(c)**, whereas the gap closes with  $\alpha = 0^\circ$  as shown in **Fig.10(d)**.

Simultaneously, three flat bands appear at 476.5 kHz, 494.42 kHz, and 505.25 kHz. The modal shapes of these flat bands show localized nature of the modes near the circular holes, as highlighted in Fig. 1(c) by the black arrows, in contrast to the topologically non-trivial bands indicating non-localized characters of the pressure distributions as highlighted in Fig. 1(c) by the red arrows. These modes are shown to couple with each other when the edge mode generated from the non-trivial modes crosses the flat bands.

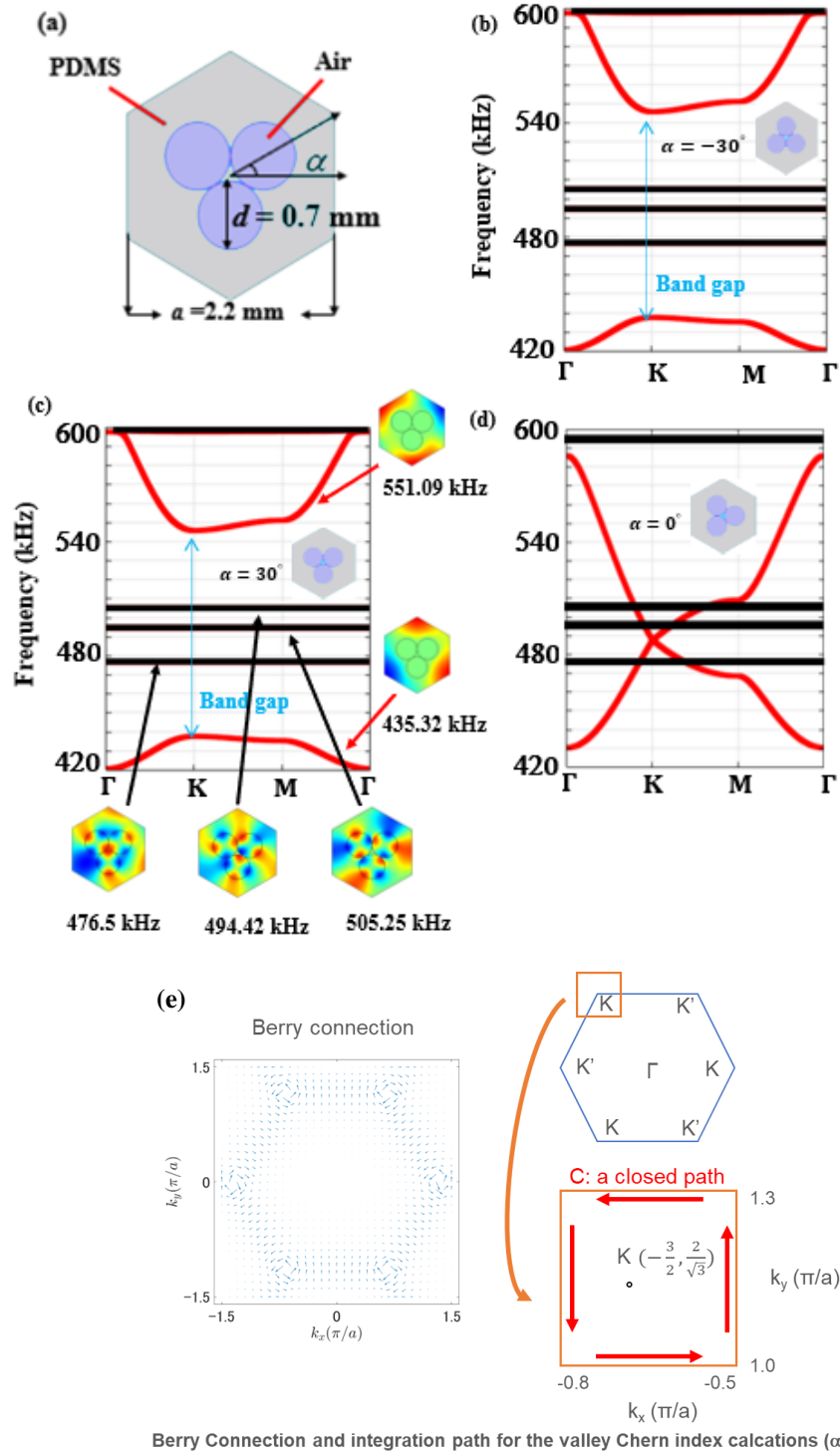


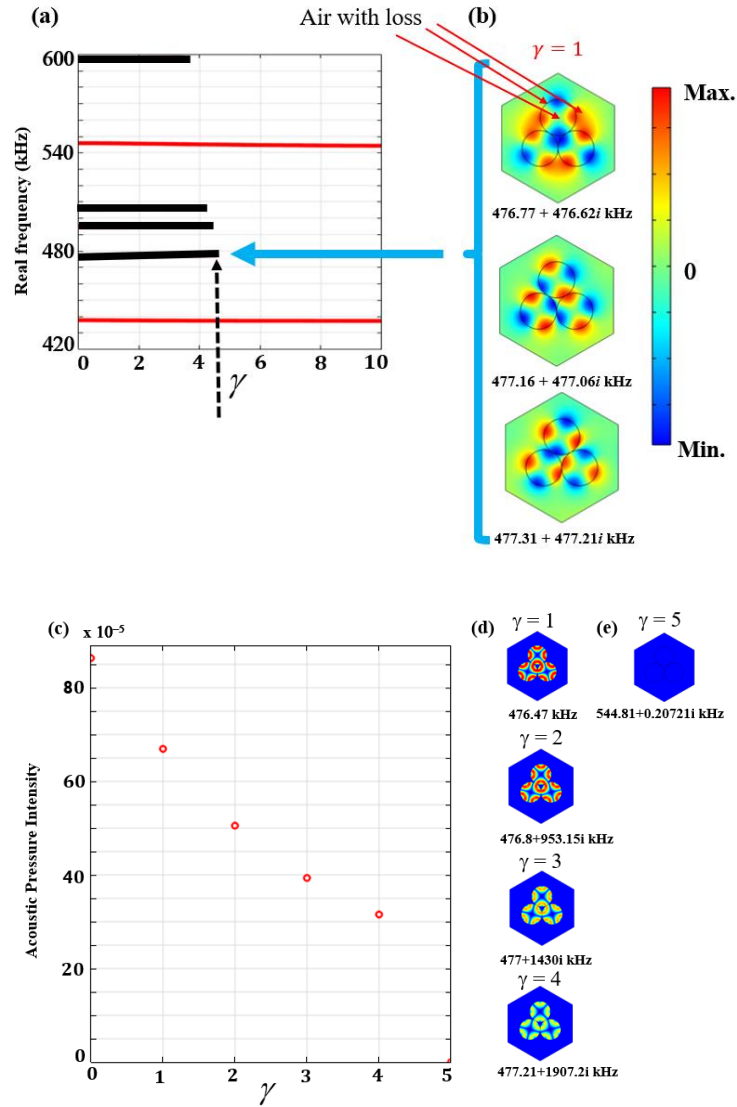
**Fig.10:** (a) Hexagonal unit cell at the orientation  $\alpha = 30^\circ$ . Phononic band gap for Hermitian system at the orientations (b)  $\alpha = -30^\circ$ , (c)  $\alpha = 30^\circ$ , (d)  $\alpha = 0^\circ$ . The pressure field

distributoins indicated by the red arrows show propagating dispersive modes at 435.32 kHz, and 551.09 kHz, respectively, and those indicated by black arrows depict localized modes at 476.5 kHz, 494.42 kHz, and 505.25 kHz, respectively, and (e) the Berry connection and integration of path for the valley Chern index (**Adopted from M.S. Ali et al. Applied Physics Express, 2023**).

#### 4.6 Extinction of Lossy Localized States in Unit Cell

In this section, we introduce the non-Hermite modulation into the system via a loss parameter to observe the mode characteristic as a function of the parameter in the oriented unit cell ( $\alpha = 30^\circ$ ). To implement the loss effects to the fluidic materials filled in the circular hole, we adapted a model where the speed of sound ( $c_{air}$ ) was replaced by a complex parameter simply as  $c_l = c_{air}(1 + i\gamma)$ . **Fig.11(a)** shows the real parts of the eigenfrequencies at a point along  $\Gamma$ -K in the Brillouin zone. This reveals that the localized mode (highlighted by black lines) appears for non-Hermite modulation  $\gamma < 4.5$ . Each of the three degenerate localized modes has the three-fold symmetry corresponding to the shape of the unit cell, and the respective complex (lossy) eigenfrequency 476.77+476.62i kHz, 477.16+477.06i kHz, and 477.31+477.21i kHz, respectively, at  $\gamma=1$ , as depicted in **Fig.11(b)**. Conversely, the localized mode (highlighted in black color) vanishes for the non-Hermite modulation when  $\gamma > +4.5$ . i.e., larger values of the non-Hermiticity parameter in conjunction with its imaginary parts lead to a certain type of extinction of the real eigenvalues. For more clarification, we calculate the acoustic pressure intensity with respect to non-Hermitian modulation  $\gamma$ , as shown in the **Fig.11(c)**. The circular shape (red color) clarify that the localized mode appears for certain value of  $\gamma < 4.5$ , as shown in the **Fig.11(d)** (with eigenfrequency 476.47 kHz, 476.8+953.15i kHz, 477+1430i kHz, and 477.21+1907.2i kHz, respectively). But the localized mode disappears for  $\gamma > 4.5$  as depicted in the **Fig.11(e)** (with eigenfrequency 544.81+0.20721i kHz). We also check the phononic band through the unit cell, where the circular hole filled with air lossy. If we set  $\gamma = 2$ , then the localized modes appear in the bulk band gap frequency for both unit cell structure with orientation  $\alpha = -30^\circ$ , and  $\alpha = 0^\circ$ , respectively, as shown in the **Fig.11(f-g)**. But, if we set the large variation

of non-Hermitian modulation (like as  $\gamma = 10$ ), then we observe the localized mode disappears, as depicted in the **Fig.11(h-i)**. The same event will happen if we set  $\gamma = 2$  for the unit cell structure  $\alpha = 30^\circ$ . From above examinations, we conclude that the non-Hermitite modulation can control a switching of the localized modes within the band gap.





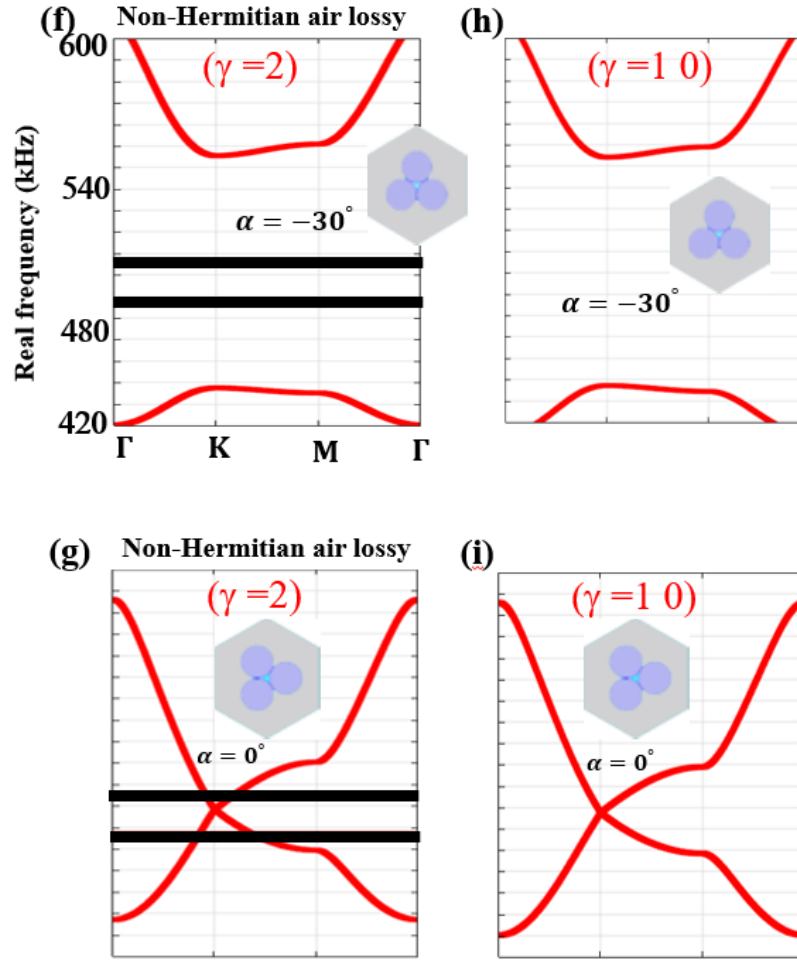


**Fig.11:** (a) The variation of the real eigenfrequency as a function of  $\gamma$ , where the localized mode highlighted by black color, (b) The pressure field of three symmetric localized mode (when  $\gamma = +1$ ) with complex eigenfrequency  $476.77+476.62i$  kHz, and  $477.16+477.06i$  kHz, and  $477.31+477.21i$  kHz, respectively, (c) the acoustic pressure intensity via the non-Hermitian modulation, (d) the corresponding pressure field of (c) with complex eigenfrequency that indicating the localized mode appears near the holes, (e) localized mode disappears for  $\gamma = 5$ , and (f-g) the localized mode appears in the bulk band gap frequency through unit cell when non-Hermitian lossy  $\gamma = 2$ , and (h-i) the localized mode disappears in the bulk band gap frequency through unit cell when non-Hermitian lossy  $\gamma = 10$  (**Adopted from M.S. Ali et al. Applied Physics Express, 2023**).

## 4.7 Extinction of Lossy Localized States in Interface Supercell

Herein, we evaluated the band property of valley phononic supercell, where all of the unit cell is composed of circular holes in a  $C_{3v}$  symmetry structure with two orientations  $\alpha = 30^\circ$  and  $\alpha = -30^\circ$ , as schematic illustrates in **Fig.12(a)**. The width and height of this supercell structure are  $a$ , and  $\frac{30a}{\sqrt{3}}$  respectively. The interfaces between upper  $\alpha = 30^\circ$  and lower  $\alpha = -30^\circ$  oriented layers generate topologically protected edge states. **Figure 12(b)** shows an edge state around 438–490 kHz in Hermitian system ( $\gamma = 0$ ), where the two pseudo-spin modes (highlighted by red color) appear at the  $K^+$  and  $K^-$  points (near the  $K$  points in the Brillouin zone of this supercell). Also, the localized mode (highlighted by black color) appears between upper and lower bulk modes (highlighted by blue color), as like valley phononic band through unit cell  $\alpha = 0^\circ$ . We then introduce the non-Hermiticity, where each circular hole filled by a lossy air. **Fig. 12(b)** also shows the localized modes are extinct ( $\gamma = 10$ ). Such a phenomenon, which is in contrast to an ordinary materials loss effect, can be understood as analogous to the bound-to-unbound transition of quantum states via the non-Hermitian parameter ( $\gamma$ ) [47]. As an analogy of the effects of the non-Hermiticity on the quantum bound state, the present model exhibits that strongly localized mode at a real frequency cannot be sustained for  $\gamma$  greater than a certain value, and the eigen frequency with pure imaginary components can only survive.

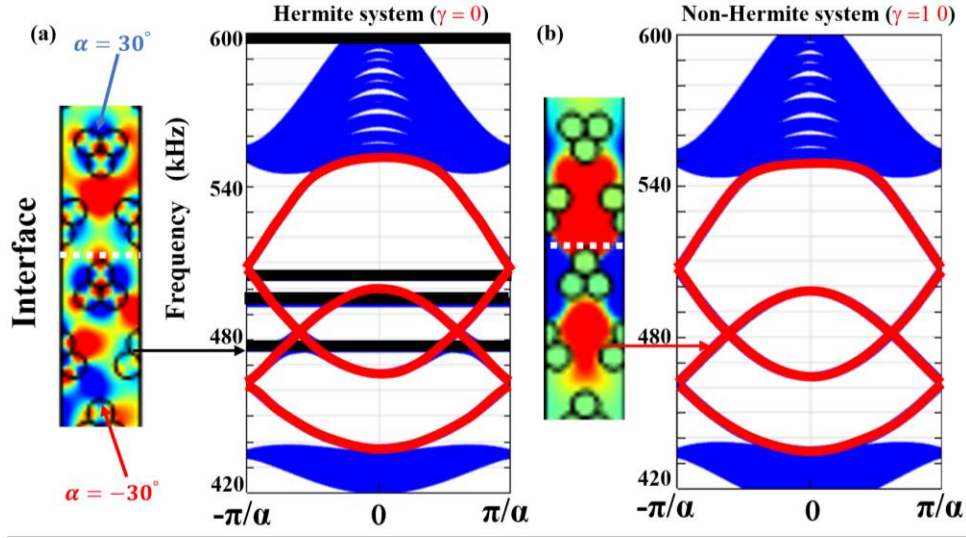


**Fig.12:** The pressure field distributions and the valley interface band diagrams of  $C_{3v}$  symmetric supercell structure with different orientations ( $\alpha = 30^\circ$  and  $\alpha = -30^\circ$ ) of the unit-cell layers for (a) Hermitian and (b) non-Hermitian lossy systems, respectively (Adopted from M.S. Ali et al. *Applied Physics Express*, 2023).

#### 4.8 Switching On/Off of Loss Effects on Z-Shaped Waveguides

Based on the above analyses, we performed the wave transmission simulations in Z-shaped waveguide constructed by a topological interface. Topologically protected edge-mode excitation as well as efficient wave transmission became a promising approach to observe the acoustic phenomenon. The edge-mode excitation and wave propagation in a Z-shaped waveguide interface have been examined in a solid substrate. Following the application of a 1 Pa incident pressure field in Hermitian system ( $\gamma = 0$ ), we observed strong edge-mode excitation along the Z-shaped waveguide interface at 476 kHz, as depicted in **Fig.13(a)**.

We then introduce the non-Hermiticity such that the circular hole was filled with lossy air. When we set  $\gamma = 2$ , then we observed relatively weak edge-mode excitation at the frequency 476 kHz, as shown in **Fig.13(b)**. This is because the excited edge-mode is coupled with the

localized mode excitation that appears in the bulk band gap frequency for  $\gamma = 2$ . If we increase the value of non-Hermitian modulation up to a value near 2.5, the degradation of the edge-mode propagations can be identified. If we further increase the value to  $\gamma = 10$ , then we can observe the recovery of an edge-mode excitation similar to the case in which  $\gamma = 0$ , as highlighted in the **Fig.13(c)**, because the localized mode is extinct for a large value of  $\gamma$ . The first figure of **Fig.13(d)** clearly shows that shorter wavelength modulation of the pressure field inside the holes, implying that the localized mode appears at  $\gamma = 2$ , whereas the second figure reveals the pressure fields are dominated mostly by the fields outside the holes, indicating the extinction of localized mode for  $\gamma = 10$ .

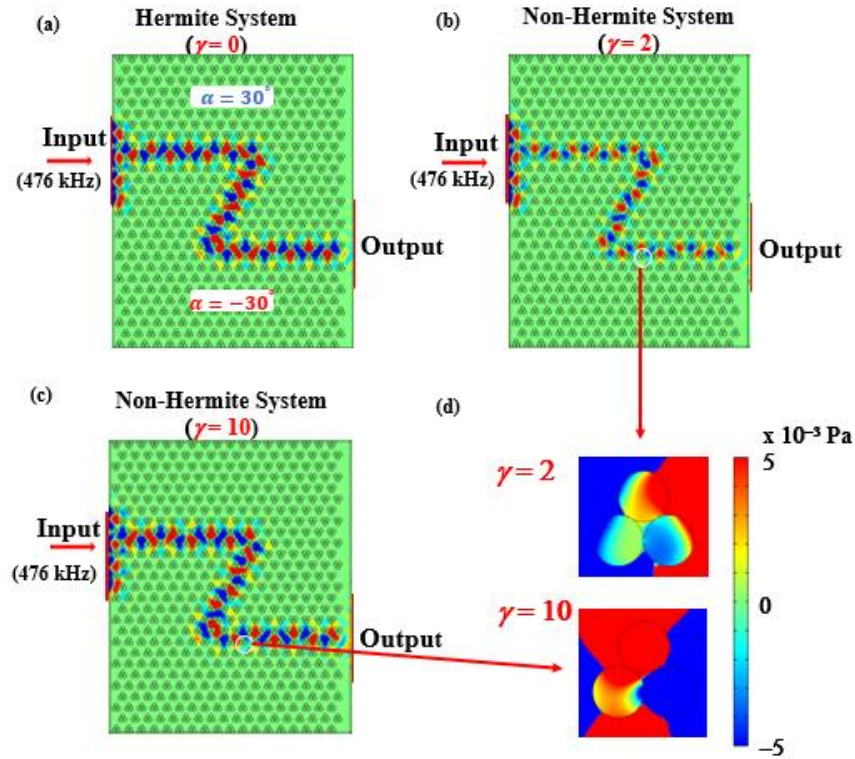


**Fig.13:** Normalized total acoustic pressure in a Z-shaped waveguide interface at 476 kHz in (a) Hermitian ( $\gamma = 0$ ) and non-Hermitian lossy systems with (b)  $\gamma = 2$  and (c)  $\gamma = 10$ . (d) Pressure distribution (enlarge) of the Z-shaped waveguide depicted in (b) and (c). (White circles in (b) and (c) highlight the positions of the circular holes depicted in (d)) (**Adopted from M.S. Ali et al. Applied Physics Express, 2023**).

## 4.9 Transmission Spectrum of Z-Shaped Waveguides

The transmission spectrum of the total output pressure along the Z-shaped waveguide interface was calculated as shown in the lower portion of **Fig. 14**. The small circular shapes with different colors on the dashed vertical black line at upper portion represent the peak positions at 476 kHz. We observed efficient transmission for  $\gamma = 0$  (Hermitian) (as highlighted by the blue circle) at 476 kHz. Although we can observe the lower transmission peak at  $\gamma = 2$  (orange circle) owing to the effect of the coupled localized mode, we can also observe a higher transmission peak at  $\gamma = 10$  (the black circle). This finding is comparable with the Hermitian system in which  $\gamma = 0$ . Because the localized mode disappears when  $\gamma = 10$ , the incident pressure field can excite the edge mode without losing energy due to the coupling with the lossy localized modes.

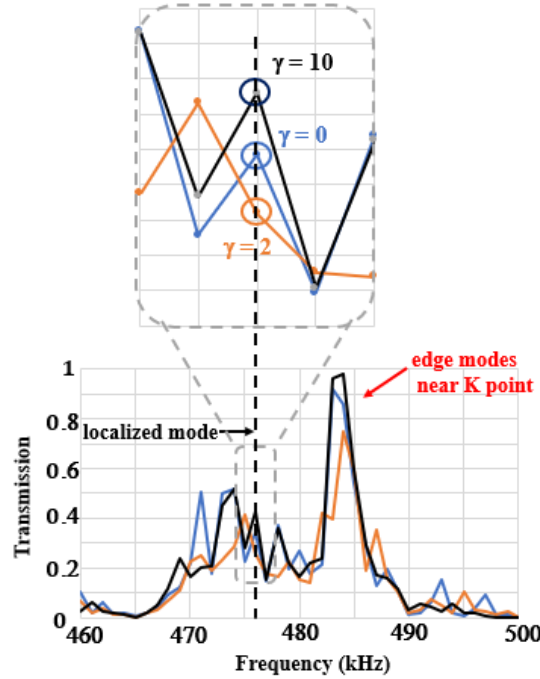


**Fig.14:** The transmission spectrum of the Z-shaped waveguide interface in Fig.13(a-c) (the lower graph) and its magnified view (the upper graph) in the vicinity of the localized mode frequency (476kHz) indicated by the dashed vertical black line (**Adopted from M.S. Ali et al. Applied Physics Express, 2023**).

## 4.10 Evanescent Wave Transmission

### 4.10.1 Uniform Structure

The topologically protected edge mode excitation became a promising approach to observing the acoustic phenomenon. To explain the transmission behavior with the effect of  $\gamma$ , firstly, we construct a uniform waveguide where each unit cell  $\alpha = 30^\circ$  is oriented, as schematically illustrated in the **Fig.15(a)**. The circular hole of each unit cell is filled by air only. If we set  $\gamma = 0$  (Hermitian), then the **Fig.15(a)** shows no transmission at 476 kHz frequency, because the incident pressure (1 Pa) can not excite the edge mode. Later, we introduce non-Hermiticity, where each circular holes filled by air gain, and air loss, respectively, as depicted in the **Fig.15(b)**. If we set  $\gamma = 10$ , then we also observe no transmission. Because the incident pressure cannot excite the edge state for this small non-Hermitian modulation. Then, we increase again the value of non-Hermitian modulation. If we introduce the non-Hermiticity again and set  $\gamma = 50$ , then **Fig.15(c)** shows almost the same behavior, whereas the evanescent sensitivity has decreased for a large penetrating area for  $\gamma = 100$ . As a result, we see wave propagation, as shown in the **Fig.15(d)**. Further increasing the value of non-Hermitian modulation, one will observe very weak evanescent sensitivity at 476 kHz. The above analysis clarifies that the magnitude of non-Hermite parameter  $\gamma$  has an effect on active control of evanescent waves in topological waveguides, balanced with gain and loss, respectively.

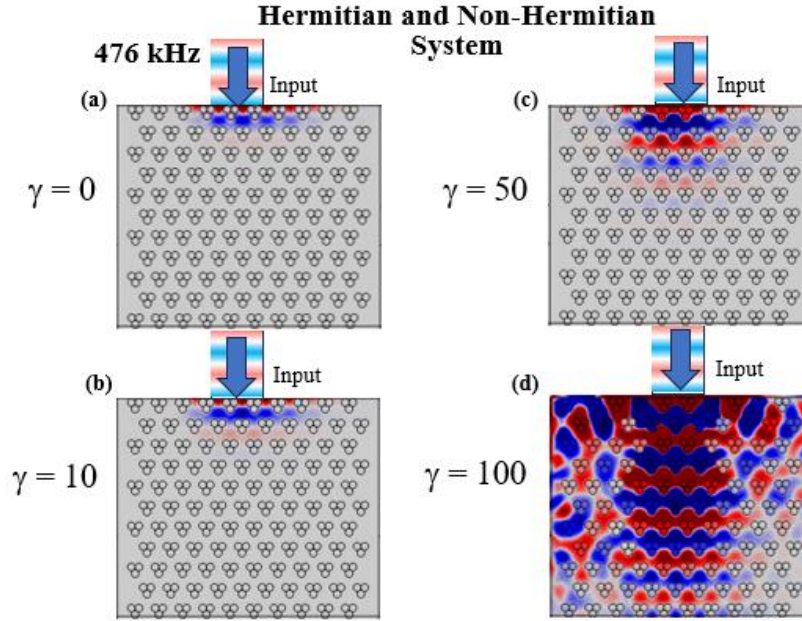


**Fig.15:** The normalized total acoustic pressure in a uniform waveguide at 476 kHz (a) Hermitian regime, when  $\gamma = 0$ , and non-Hermitian regime (b) when  $\gamma = 10$ , (c) when  $\gamma = 50$ , and (d) when  $\gamma = 100$ , respectively.

#### 4.10.2 Straight Waveguide

In this section, we prepared the straight waveguide interface by using the previous uniform waveguide (**Fig.15(a)**) with two differently oriented circular hole arrays,  $\alpha = 30^\circ$  and  $\alpha = -30^\circ$ , respectively, as depicted in **Fig.16(a)**. Then, we observe edge mode excitation as well as evanescent transmission at the frequency of 476 kHz. We arranged our system in the following three cases: **Case (I):** We rotate nine layers of  $\alpha = 30^\circ$  oriented unit cells to create  $\alpha = -30^\circ$  oriented unit cells below the interface. We keep two layers of  $\alpha = 30^\circ$  oriented unit cells unchanged above the interface. The dashed horizontal line (highlighted by white color) indicates the current location of the interface, where all the lines are placed very close to the input channel in the **Fig.16(b)-Fig.16(d)**, respectively. **Case (II):** We rotate five layers of  $\alpha = 30^\circ$  oriented unit cells to create  $\alpha = -30^\circ$  oriented unit cells below the interface. The dashed horizontal line (highlighted by yellow color) indicates the current location of the

interface where all the lines are placed at the center in the **Fig.16(a)**, and **Fig.16(e)-Fig.16(g)**, respectively. and **Case (III)**: we rotate two layers of  $\alpha = 30^\circ$  oriented unit cell to make  $\alpha = -30^\circ$  oriented unit cells below the interface. We keep nine layers of  $\alpha = 30^\circ$  oriented unit cells unchanged above the interface. The dashed horizontal line (highlighted by blue color) indicates the current location of the interface, where all the lines are placed very far away from the input channel in the **Fig.16(h)-Fig.16(j)**, respectively. If we apply 1 Pa incident pressure as an input in the Hermitian regime ( $\gamma = 0$ ), then **Fig.16(a)** shows the incident pressure field through the channel cannot excite the edge mode because of strong evanescence occurs for a large penetrating area, and as a result, waves cannot propagate along this waveguide interface. Later, we introduce non-Hermiticity, where both air gain and air loss work consecutively in the circular hole of each unit cell. We defined the variables  $d$ ,  $d_1$ ,  $d_2$ , and  $d_3$ , respectively, for the distance of the input channel from the center, closer/near, and far location of the interface. If we set  $\gamma = 0.5$ , then we found only weak edge mode excitation in **Fig.16(b)**, where the location of the interface is closer to the input channel, but no edge mode excitation was observed from the waveguide as shown in **Fig.16(f)**, and **Fig.16(j)**, because the location of interface is at the center, and far distance from the input channel. In a similar way, if we set  $\gamma = 50$ , then we observed the edge mode excitation in both the waveguide and the waveguide. as depicted in **Fig.16(c)**, and **Fig.16(g)**, respectively. Because the evanescent sensitivity has monotonically decreased with large variations of non-Hermitian modulation. But no edge mode excitation happens in **Fig.16(k)**, because of the same reason as well as **Fig. 16 (a)**. Finally, if we set  $\gamma = 100$ , then we see very low evanescent sensitivity. So, the strong edge mode excitation occurs, and we observed efficient transmission from all the waveguides, as highlighted in the **Fig.16(d)**, **Fig.16(h)**, and **Fig.16(i)**, respectively. This behavior proves the evanescent wave propagation depends on the non-Hermiticity parameter  $\gamma$ , because the edge-mode excitation can be attributed to how deeply the incident wave can propagate into the bulk region to reach the interface location.



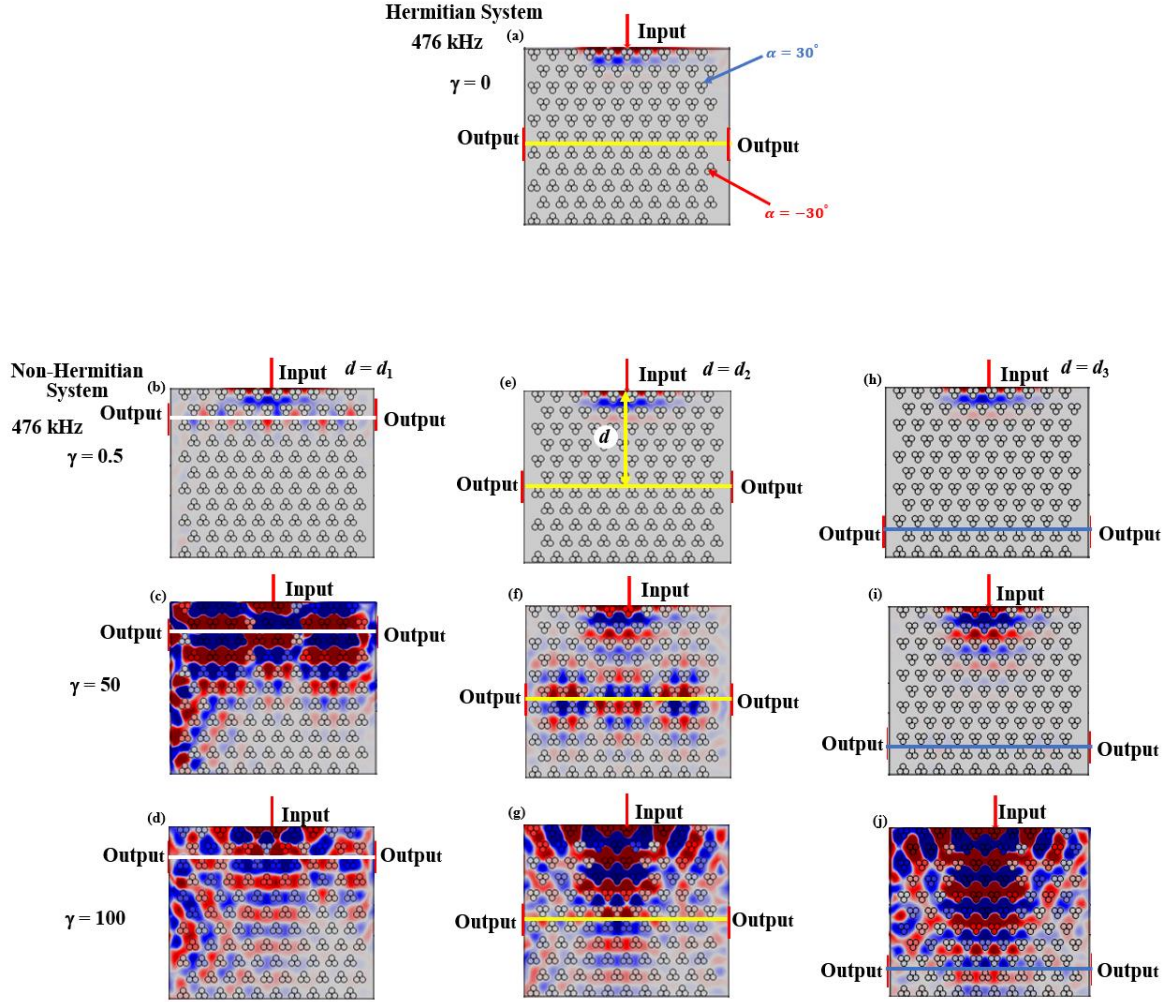


**Fig.16:** The normalized total acoustic pressure in a valley straight phononic waveguide with differently oriented  $C_{3v}$  symmetry unit cell  $\alpha = 30^\circ$  and  $\alpha = -30^\circ$  respectively, and separated by an interface (the dashed horizontal line highlighted by yellow color) (a) in Hermitian system. Comparisons of the normalized total acoustic pressure in non-Hermitian system with  $\gamma = 0.5, 50$ , and  $100$  respectively, (b-d) when the location of interface is very closer from the input channel (the dashed horizontal line highlighted by white color) (e-g) when the location of interface is center, (h-j) when the location of interface is far away from the input channel (the dashed horizontal line highlighted by blue color).

### 4.10.3 Z-Shaped Waveguide

We also examined edge mode excitation as well as transmission analysis in a Z-shaped waveguide in Hermitian, and non-Hermitian systems, when the interface location was at center. The edge mode excitation was absent in the Hermitian regime ( $\gamma = 0$ ). As a result, no wave propagation occurs at 476 kHz, as highlighted in the **Fig.17(a)**. If we set  $\gamma = 0.5$ , then the incident pressure field can not excite the bulk mode, and no propagation occurs, as shown in the **Fig.17(b)**. On the other hand, edge mode excitation was observed in the non-Hermitian regime with the values of  $\gamma = 50$ , and 100, respectively. The waveguide as depicted in **Fig.17(c)**, and **Fig.17(d)** shows the low evanescent sensitivity as well as efficient wave transmission at 476 kHz frequency in the non-Hermitian regime.

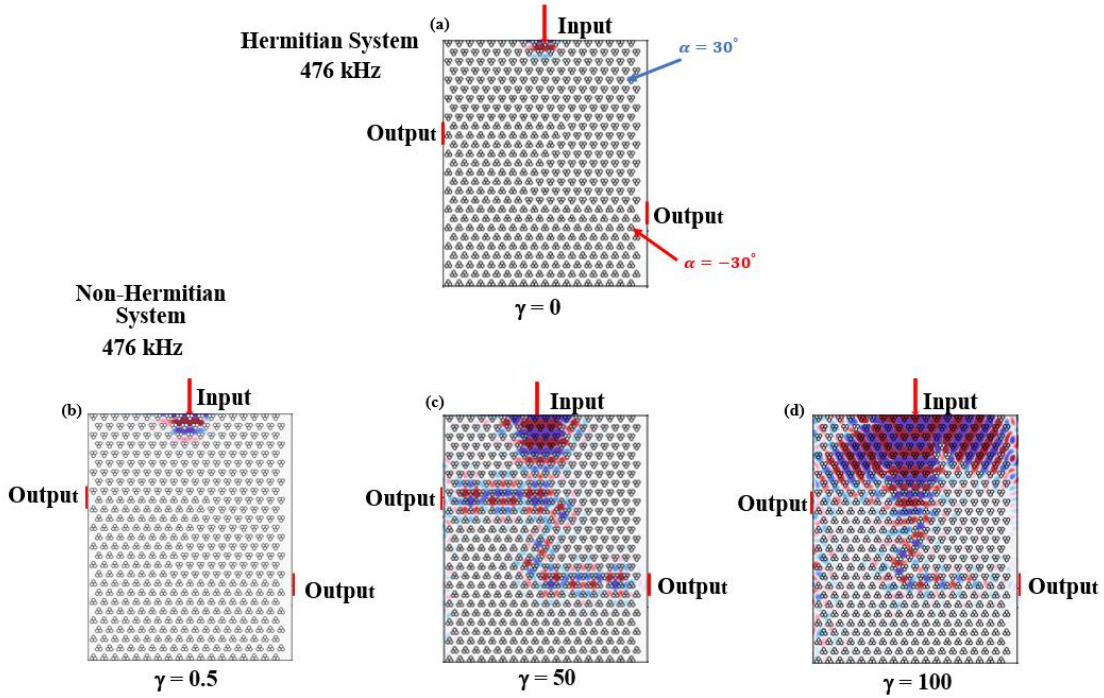


**Fig.17:** Comparisons of the total acoustic pressure at 476 kHz in valley phononic Z-shaped waveguide (a) in Harmitian system, and (b-d) in non-Hermitian system (balanced with air loss, and air gain) with  $\gamma = 0.5$ , 50, and 100, respectively, where the location of interface is at center.

## Chapter 5

### Conclusion and Future Work

Topological acoustic waveguides are the fundamental requirement for active control of efficient wave propagation by taking advantages of topological protection. The first part of this thesis mainly introduced the translational shift of the metallic rod array in both reconfigurable straight and Z-shaped acoustic waveguides to observe the robust transmission phenomena along the topological edge state. Actually, efficient transmission along the path of waveguide interface is a challenging issue because various types of defects (such as cavities, disorder, and bending etc.) has already shown significant backscattering. As a result, we generally achieve very low transmission from a defective waveguide. With proper modeling and artificial arrangement, we can construct a new class of architected topological acoustic waveguide that will be immune to defects (immunization of backscattering), imperfections, and scattering losses. In this point of view, we proposed a design of the novel reconfigurable topological waveguide interface from a uniform  $C_{3v}$  symmetry crystal structure with orientation  $\alpha = 30^\circ$ , where the opposite orientation arrays  $\alpha = -30^\circ$  were formed by the translational shift of metallic steel-rod towards the application of dynamical adjustability, and reconfigurability is highly desired for an integrated switchable acoustic device. Our results demonstrated that the band topology phase transition of the localized mode for symmetric breaking can be identified by observing the signs and distribution of the Berry curvature in the Brillouin zone. Also, the continuous translation of the rod breaks the local  $C_{3v}$  symmetry, which can also be applied for switching on and off the band gap opening. It is worth noting that the localized mode corresponding to the dimer array slightly degrades the pressure field in the path of the reconfigured waveguide interface. However, even when a localized mode is present in the reconfigured waveguide interface, the acoustic wave can still robustly propagate, which is comparable to an ideal valley phononic waveguide. Therefore, the valley support transport of acoustic energy can be controlled by designing a robust reconfigurable waveguide interface by shifting the rod array to the topologically protected edge state. This can be used as a new approach to designing a cavity free robust switchable acoustic device with high reconfigurability.

On the other hand, the second part demonstrates the switchable behavioral differences between lossy and nearly lossless edge-mode propagation by non-Hermitian modulation. We found that the large variation of non-Hermiticity in a 2D acoustic system led to active control of the localized mode as well as waveguide transmission at 476 kHz. The complex eigenfrequency with a certain value of non-Hermitian modulation shows the exponential decay behavior of propagation because the non-trivial propagating modes are coupled with localized modes at the bulk band gap frequency. But, if the wavelength becomes smaller than the diameter of the circular rod, both the large variation of non-Hermiticity and eigenfrequency with imaginary parts lead to the disappearance of real eigenvalues. As a result, strong edge mode excitation recovers again, that confirming efficient transmission comparable with the Hermitian system. Actually, the proper choice of non-Hermiticity parameter ( $\gamma$ ) with gain or loss or balanced with gain and loss is practically important for unified real application in non-Hermitian topological acoustic systems. Moreover, the evanescent sensitivity can be attributed to how deeply the incident wave can propagate into the bulk region to reach the interface location. The present results can be utilized to fabricate topological acoustic devices in non-energy-conserving systems based on valley phononic crystals.

In the future, we will focus on the experimental setup of the proposed reconfigurable design as a switchable integrated circuit device, such as field programmable gate arrays (FPGAs), which could serve broadband functionality that is essential to understanding the mechanical signal processors. For experimental realization, a piezoelectric microelectromechanical systems (MEMS) acoustic sensor with our configured structure should be a suitable candidate [1]. We may dedicate a switch to the proposed MEMS design to control the translational shift of the metallic rod array of the supercells, as well as reconfigurable waveguides. On the other hand, if we introduce the stream or gas-saturated (carbon) in the air, then it should work as a lossy material [2]. The loss factor gamma (non-Hermiticity parameter) can be controlled to obtain the non-Hermitian material property (like density) for which one will observe the strong or weak edge mode excitation as well as wave propagation in a waveguide.

Also, we will construct new geometry and structure to observe exotic properties (like exceptional points, skin modes, etc.) for active control of unidirectional wave propagation in an integrated switchable acoustic device beyond the Hermite system.

## References

### Abstract

- [1] J.-C. Hsu and T.-T. Wu, Phys. Rev. B **74**, 144303 (2006).
- [2] M.S. Kushwaha, P. Halevi, L. Dobrzynski, and Djafari-Rouhani, B. Phys. Rev. Lett. **71**, 2022 (1993).
- [3] A. Khelif, A. Choujaa, S. Benchabane, B. Djafari-Rouhani, and V. Laude, Appl. Phys. Lett. **84**, 4400 (2004).
- [4] Y. Pennec, B. Djafari-Rouhani, J.O. Vasseur, A. Khelif, and P.A. Deymier, Phys. Rev. E **69**, 046608 (2004).
- [5] Sun, J.-H.; Wu, T.-T. Phys. Rev. B **71**, 174303 (2005).
- [6] O. Matsuda, O.B. Wright, A. Khelif, A. Adibi (Eds.), Springer: New York, NY, USA, p. 191 (2016).
- [7] L.-Y. Wu, L.-W. Chen, and C.-M. Liu, Appl. Phys. Lett. **96**, 013506 (2009).
- [8] Z. Liu, X. Zhang, Y. Mao, Y.Y. Zhu, Z. Yang, C.T. Chan, and P. Sheng, Science **289**, 1734 (2000).
- [9] D. Zhao, Y. Ye, S. Xu, X. Zhu, and L. Yi, Appl. Phys. Lett. **104**, 043503 (2014).
- [10] D. Hatanaka, H. Yamaguchi, APL Mater. **9**, 071110 (2021).
- [11] T.B. Workie, T. Wu, J.-F. Bao, and K. Hashimoto, Jpn. J. Appl. Phys. **60**, SDDA03 (2021).
- [12] R. Hikata, K. Tsuruta, A. Ishikawa, K. Fujimori, Jpn. J. Appl. Phys. **54**, 07HB07 (2015).
- [13] X. Li, and Z. Liu, Phys. Lett. A **338**, 413 (2005).
- [14] K. Manabe, A. Ishikawa, K. Yamamoto, T. Kanda, K. Tsuruta, Proc. 2018 IEEE International Ultrasonics Symposium (IUS), 8580129 (2018).
- [15] Y. Deng, H. Ge, Y. Tian, M. Lu, and Y. Jing, Phys. Rev. B **96**, 184305 (2017).
- [16] Z. Zhang, Y. Tian, Y. Chen, Q. Wei, X. Liu, and J. Christensen, Phys. Rev. Appl. **9**, 034032 (2018).

- [17] M.S. Ali, M. Kataoka, M. Misawa, and K. Tsuruta, Jpn. J. Appl. Phys. **62**, SJ1002 (2023).
- [18] M.S. Ali, Y. Hata, M. Kataoka, M. Misawa, and K. Tsuruta, Mater. Sci. Forum (Proc. Thermec2023, Internatn'l Conf. Proc. Manufact. Adv. Mat.)
- [19] A. Krasnok, N. Nefedkin and A. Alù, IEEE Antennas and Propagation Magazine **63**, 110-121(2021).
- [20] M. Kataoka, M. Misawa, and K. Tsuruta, Symmetry **14**, 2133 (2022).
- [21] M.S. Ali, Y. Hata, and K. Tsuruta, Appl. Phys. Express, August 18 (2023);  
DOI 10.35848/1882-0786/acf1ef

## Chapter 1

- [1] Z. Wang, Y. Chong, J.D. Joannopoulos, and M. Soljacic, Nature **461**, 772 (2009).
- [2] Z. Wang and S. Fan, Appl. Phys. B **81**, 369 (2005).
- [3] R. Fleury, D. L. Sounas, C. F. Sieck, M. R. Haberman, and A. Alù, Science **343**, 516 (2014).
- [4] A. Khelif, B. Aoubiza, S. Mohammadi, A. Adibi, and V. Laude, Phys. Rev. E **74**, 046610 (2006).
- [5] H. Zhu and F. Semperlotti, AIP Adv. **3**, 092121 (2013).
- [6] B. Rostami-Dogolsara, M. K. Moravvej-Farshi, and F. Nazari, Phys. Rev. B **93**, 014304 (2016).
- [7] H.-W. Dong, Y.-S. Wang, and C. Zhang, Ultrasonics **76**, 109 (2017).
- [8] T.-C. Wu, T.-T. Wu, and J.-C. Hsu, Phys. Rev. B **79**, 104306 (2009).
- [9] Y. Jin, N. Fernez, Y. Pennec, B. Bonello, R. P. Moiseyenko, S. Hémon, Y. Pan, and B. Djafari-Rouhani, Phys. Rev. B **93**, 054109 (2016).

- [10] R. Lucklum, M. Ke, and M. Zubtsov, *Sens. Actuators B* **171**, 271 (2012).
- [11] T.-X. Ma, Y.-S. Wang, C. Zhang, and X.-X. Su, *Sens. Actuators A* **242**, 123 (2016).
- [12] D. Jia, H.-X. Sun, J.-P. Xia, S.-Q. Yuan, X.-J. Liu, and C. Zhang, *New J. Phys.* **20**, 09302 (2018).
- [13] M. I. Shalaev, S. Desnavi, W. Walasik, and N. M. Litchinitser, *New J. Phys.* **20**, 023040 (2018).
- [14] T. Cao, L. Fang, Y. Cao, N. Li, Z. Fan, and Z.o Tao, *Sci. Bull.* **64**, 814 (2019).
- [15] A. Darabi and M. Leamy, *J. Acoust. Soc. Am.* **146**, 773 (2019).
- [16] Z. Tian, C. Shen, J. Le, E. Reit, H. Bachman, J. E.S. Socolar, S. A. Cummer, and T. J. Huang, *Nat. Commun.* **11**, 762 (2020).
- [17] X. Zhuang, C. Nguyen, S.S. Nanthakumar, L. Chamoin, Y. Jin, and T. Rabczuk, *Mater. Design*, **219**, 110760 (2022).
- [18] L.-Y. Feng, H.-B. Huang, J.-C. Zhang, X.-P. Xie, and J.-J. Chen, *Phys. Lett. A* **382**, 2880 (2018).
- [19] Y.-F. Wang, L. Yang, T. Wang, A.-L. Chen, and V. Laude, *Appl. Materials* **9**, 081110 (2021).
- [20] N. Gao, S. Qu, L. Si, J. Wang, and W. Chen, *Appl. Phys. Lett.* **118**, 063502 (2021).
- [21] Y. Hatsugai, *Phys. Rev. Lett.* **71**, 3697 (1993).
- [22] Y. Hatsugai, T. Fukui, and H. Aoki, *Phys. Rev. B* **74**, 205414 (2006).
- [23] A. B. Khanikaev, R. Fleury, S. H. Mousavi, and A. Alù, *Nat. Commun.* **6**, 8260 (2015).
- [24] Z. Yang, F. Gao, X. Shi, X. Lin, Z. Gao, Y.Chong, and B. Zhang, *Phys. Rev. Lett.* **114**, 114301 (2015).
- [25] Z. G. Chen and Y. Wu, *Phys. Rev. Appl.* **5**, 054021 (2016).



- [26] X. Ni, C. He, X. C. Sun, X. P. Liu, M. H. Lu, L. Feng, and Y. F. Chen, *New J. Phys.* **17**, 053016 (2015).
- [27] L. M. Nash, D. Kleckner, A. Read, V. Vitelli, A. M. Turner, and W. T. M. Irvine, *Proc. Natl. Acad. Sci.* **112**, 14495 (2015).
- [28] P. Wang, L. Lu, and K. Bertoldi, *Phys. Rev. Lett.* **115**, 104302 (2015).
- [29] R. Chaunsali, C. W. Chen, and J. Yang, *Phys. Rev. B* **97**, 054307 (2018).
- [30] S. Y. Yu, C. He, Z. Wang, F. K. Liu, X. C. Sun, Z. Li, H. Z. Lu, M. H. Lu, X. P. Liu, and Y. F. Chen, *Nat. Commun.* **9**, 3072 (2018).
- [31] C. Brendel, V. Peano, and F. Marquardt, *Phys. Rev. B* **97**, 020102(R) (2018).
- [32] J. Wang and J. Mei, *Appl. Phys. Express* **11**, 05702 (2018).
- [33] I. Kim, Y. Arakawa, and S. Iwamoto, *Appl. Phys. Express* **12**, 047001 (2019).
- [34] R. El-Ganainy, K. G. Makris, M. Khajavikhan, Z. H. Musslimani, S. Rotter, and D. N. Christodoulides, *Nat. Phys.* **14**, 11 (2018).
- [35] M.-A. Miri and A. Alu, *Science* **363**, eaar7709 (2019).
- [36] Y. Ashida, Z. Gong, and M. Ueda, *Adv. Phys.* **69**, 249 (2020).
- [37] Z. Gu, H. Gao, P.-C. Cao, T. Liu, X.-F. Zhu, and J. Zhu, *Phys. Rev. Appl.* **16**, 057001 (2021).
- [38] A. Krasnok, N. Nefedkin, and A. Alu, *IEEE Antennas Propag. Mag.* **63**, 110 (2021).
- [39] S. Longhi, *EPL* **120**, 64001 (2018).
- [40] A. Krasnok and A. Alù, *arXiv:2103.08135* (2021).
- [41] Makio Kawasaki, Ken Mochizuki, and Hideaki Obuse. *Phys. Rev. B* **106**, 035408 (2022).
- [42] H. Gao, H.R. Xue, Z.M. Gu, T. Liu, J. Zhu et al. *Nature Commun.* **12**, 1888 (2021).

- [43] B. Midya. *Annals Phys.* **421**, 168280 (2020).
- [44] S. Xia, D. Kaltsas, D. Song, I. Komis, J. Xu et al. *Science* **372**, 72 (2021).
- [45] H. Zhao, X. Qiao, T. Wu, B. Midya, S. Longhi et al. *Science* **365**, 1163 (2019).
- [46] Xiao, L., Zhan, X., Bian, Z. et al. *Nature Phys* **13**, 1117 (2017).
- [47] M.-A. Miri and A. Alu, *Science* **363**, eaar 7709 (2019). DOI: 10.1126/Science.aar7709.
- [48] W. Tang, X. Jiang, K. Ding, Y. X. Xiao, Z. Q. Zhang, C. T. Chan, and G. Ma, *Science* **370**, 1077 (2020).
- [49] V. Achilleos, G. Theocharis, O. Richoux, and V. Pagneux, *Phys. Rev. B* **95**, 144303 (2017).
- [50] N. J. R. K. Gerard and Y. Jing, *MRS Commun.* **10**, 32 (2020).
- [51] Y. Auregan and V. Pagneux, *Phys. Rev. Lett.* **118**, 174301 (2017).
- [52] R. Fleury, D. L. Sounas, and A. Alu, *IEEE J. Sel. Top. Quantum Electron* **22**, 121 (2016).
- [53] S. Puri, J. Ferdous, A. Shakeri, A. Basiri, M. Dubois, and H. Ramezani, *Phys. Rev. Appl.* **16**, 014012 (2021).
- [54] D. N. Maksimov, A. F. Sadreev, A. A. Lyapina, and A. S. Pilipchuk. *Wave Motion* **56**, 52 (2015).
- [55] Z. Gu, H. Gao, and P.-C. Cao, *PHYS. REV, APPLIED* **16**, 057001 (2021).
- [56] Md. S. Ali, M. Kataoka, M. Misawa, and K. Tsuruta, *Proc. Symp. on Ultrasonics Electronics Vol.* **43**, 1Pa1-3 (2022).
- [57] COMSOL Multiphysics®, v. 6.1. [www.comsol.com](http://www.comsol.com). COMSOL AB: Stockholm, Sweden, Available online: <https://www.comsol.jp/forum/thread/150662/Citing-COMSOL-in-publications> (accessed on 21 September 2022).

## Chapter 2

- [1] D.Z. Rocklin, B.G. Chen, M. Falk, V. Vitelli, and T.C. Lubensky, Phys. Rev. Lett. **116** 135503 (2016).
- [2] R. Süsstrunk and S.D. Huber, Proc. Natl Acad. Sci. **113** E4767 (2016).
- [3] S. Ryu, A.P. Schnyder, A. Furusaki and A.W.W. Ludwig, New J. Phys. **12** 065010 (2010)
- [4] K. Sakoda, Springer (2004).
- [5] Y. Chung, D. G. Kim, and N. Dagli, IEEE J. Lightwave Technol. **24**, 1865 (2006).
- [6] O. Schwelb, IEEE J. Lightwave Technol. **23**, 3931 (2005).
- [7] S. V. Boriskina, T. M. Benson, P. Sewell, and A. I. Nosich, IEEE J. Lightwave Technol. **20**, 1563 (2002).
- [8] A. Hessel, M. H. Chen, R.C.M. Li, and A.A. Oliner, Proc. IEEE **61**, 183 (1973).
- [9] P. J. Crepeau and P.R. McIsaac, Proc. IEEE **52**, 33 (1964).
- [10] R. Mittra and S. Laxpati, Can. J. Phys. **43**, 353 (1965).
- [11] R. Kieburtz and J. Impagliazzo, IEEE Trans. Antennas and Propag. **18**, 3 (1970).
- [12] O. Quevedo-Teruel, M. Ebrahimpouri, and M.N.M. Kehn, IEEE Antennas Wireless Propag. Lett. 484 (2016).
- [13] R. Quesada, D. Martn-Cano, F.J. Garca-Vidal, and J. Bravo-Abad, Opt. Lett. **39**, 2990 (2014).
- [14] M. Camacho, R. Mitchell-Thomas, A. Hibbins, J. Sambles, and O. Quevedo-Teruel, Opt. Lett. **42**, 3375 (2017).
- [15] Y. Taguchi, Science **291**, 2573 (2001).

- [16] N. Nagaosa, J. Sinova, S. Onoda, A. MacDonald, and N. Ong, *Rev. Mod. Phys.* **82**, 1539 (2010).
- [17] E. N. Adams and E.I. Blount, *J. Phys. Chem. Solids* **10**, 286 (1959).
- [18] M.Z. Hasan and C.L. Kane, Colloquium: *Rev. Mod. Phys.* **82**, 3045 (2010).
- [19] D. Xiao, M. C. Chang, and Q. Niu, *Rev. Mod. Phys.* **82**, 1959 (2010).
- [20] R. D. King-Smith and D. Vanderbilt, *Phys. Rev. B* **47**, 1651 (1993).
- [21] R. Resta, *J. Phys. Condens. Matter* **12**, R107–R143 (2000).
- [22] Y. Yao et al., *Phys. Rev. Lett.* **92**(3), 037204 (2004).
- [23] M. Gradhand et al. *J. Phys. Condens. Matter* **24**, 213202 (2012).
- [24] L. Duca et al., *Science* **347**, 288 (2015).
- [25] N. Flaschner et al., *Science* **352**, 1091 (2016).
- [26] K. Okuno and K. Tsuruta, *Jpn. J. Appl. Phys.* **59**, SKKA05 (2020).
- [27] T. Fukui, Y. Hatsugai, and H. Suzuki, *J. Phys. Soc. Jpn.* **74**, 1674 (2005).

### Chapter 3

- [1] M. Xiao, G.C. Ma, Z.Y. Yang, P. Sheng, Z.-Q. Zhang, and C.T. Chan, *Nat. Phys.* **11**, 240 (2015).
- [2] C. He et al., *Nat. Phys.* **12**, 1124 (2016).
- [3] J. Lu, C. Qiu, L. Ye, X. Fan, M. Ke, F. Zhang, and Z. Liu. *Nat. Phys.* **13**, 369 (2017).
- [4] R. K. Pal, M.I Schaeffer, and M. Ruzzene. *J. Appl. Phys.* **119**, (2016).
- [5] K. Zhang, P. Zhao, F. Hong, Y. Yu, and Z. Deng, *Smart Mater. Struct.* **29**, 015017 (2020).

- [6] K. Zhang, P. Zhao, C. Zhao, F. Hong, and Z. Deng, *Compos. Struct.* **238**, 111952 (2020).
- [7] Q. Zhang, Y. Chen, K. Zhang, and G. Hu, *Extreme Mech. Lett.* **28**, 76 (2019).
- [8] X.-L. Qi and S.-C. Zhang, *Rev. Mod. Phys.*, vol. **83**, no. 4, p. 1057, (2011).
- [9] Y. Wang, H. M. Price, B. Zhang, Y. D. Chong, *Nat. Commun.* **11**, 2356 (2020).
- [10] W. Bogaerts, D. Pérez, J. Capmany, D. A. B. Miller, J. Poon, D. Englund, F. Morichetti, A. Melloni, *Nature (London)* **586**, 207, (2020).
- [11] Y. Yang, Y. Yamagami, X. Yu, P. Pitchappa, J. Webber, B. Zhang, M. Fujita, T. Nagatsuma, R. Singh, *Nat. Photon.* **14**, 446 (2020).
- [12] Y. Wang, X. Pang, Y. Lu, J. Gao, Y. Chang, L. Qiao, Z. Jiao, H. Tang, X. Jin, *Optica* **6**, 955 (2019).
- [13] F. Raghu and D.M. Haldane. *Phys. Rev. A* **78**, 1(2008).
- [14] P. Wang, L. Lu, and K. Bertoldi, *Phys. Rev. Lett.* **115**,1 (2015).
- [15] L. M. Nash, D. Kleckner, A. Read, V. Vitelli, A. M. Turner, and W.T.M. Irvine. *Proc. the Nat. Academ. Sci. U.S.A.*, **112**,14495(2015).

## Chapter 4

- [1] T. Yoshida, R. Peters, N. Kawakami and Y. Hatsugai, *Prog. Theor. Exp. Phys.* **12**, A109 (2020).
- [2] E.J. Bergholtz, J.C. Budich and F.K. Kunst, *Rev. Mod. Phys.* **93** 015005 (2021).
- [3] A. Ghatak and T.J. Das, *J. Phys.: Condens. Matter* **31** 263001 (2019).
- [4] K. Yokomizo and S. Murakami, *Prog. Theor. Exp. Phys.* **12**, A102 (2020).
- [5] Y. Ashida, Z. Gong, and M. Ueda, *Adv. Phys.* **69**, 249 (2021).

- [6] R. El-Ganainy, K.G. Makris, M. Khajavikhan, Z.H. Musslimani, S. Rotter, and D.N. Christodoulides, *Nat. Phys.* **14**, 11 (2018).
- [7] V.V. Konotop, J. Yang, and D.A. Zezyulin, *Rev. Mod. Phys.* **88**, 035002 (2016).
- [8] V.M.M. Alvarez, J.E.B. Vargas, M. Berdakin, and L.E.F. Torres, *Eur. Phys. J. Spec. Top.* **227**, 1295 (2018).
- [9] L. Feng, R. El-Ganainy, and L. Ge, *Nat. Photonics* **11**, 752 (2017).
- [10] R. El-Ganainy, K. G. Makris, M. Khajavikhan, Z. H. Musslimani, S. Rotter, and D. N. Christodoulides, *Nat. Phys.* **14**, 11 (2018).
- [11] R. El-Ganainy, M. Khajavikhan, D. N. Christodoulides, and S. K. Ozdemir, *Commun. Phys.* **2**, 37 (2019).
- [12] S. K. Gupta, Y. Zou, X. Y. Zhu, M. H. Lu, L. J. Zhang, X. P. Liu, and Y. F. Chen, *Adv. Mater.* **32**, e1903639 (2020).
- [13] S. K. Ozdemir, S. Rotter, F. Nori, and L. Yang, *Nat. Mater.* **18**, 783 (2019).
- [14] N. Moiseyev, Cambridge University Press, Cambridge, (2011).
- [15] S. John, *Phys. Rev. Lett.* **58**, 2486 (1987).
- [16] E. Yablonovitch, *Phys. Rev. Lett.* **58**, 2059 (1987)
- [17] D. Christodoulides and J. Yang, Springer, Vol. **280**, (2018).
- [18] L. Lu, J. D. Joannopoulos, and M. Soljacic, *Nat. Photonics* **8**, 821–829 (2014).
- [19] T. Ozawa, H. M. Price, A. Amo, N. Goldman, M. Hafezi, L. Lu, M. C. Rechtsman, D. Schuster, J. Simon, O. Zilberberg, and I. Carusotto, *Rev. Mod. Phys.* **91**, 015006 (2019).
- [20] C. M. Bender and S. Boettcher, *Phys. Rev. Lett.* **80**, 5243 (1998).
- [21] E. J. Bergholtz, J. C. Budich, and F. K. Kunst, *Rev. Mod. Phys.* **93**, 015005 (2021).

- [22] F. Song, S. Yao, and Z. Wang, Phys. Rev. Lett. **123**, 170401 (2019).
- [23] S. Weidemann, M. Kremer, T. Helbig, T. Hofmann, A. Stegmaier, M. Greiter, R. Thomale, and A. Szameit, Science **368**, 311 (2020).
- [24] L. Zhang, Y. Yang, Y. Ge, Y.-J. Guan, Q. Chen, Q. Yan, F. Chen, R. Xi, Y. Li, D. Jia, S.-Q. Yuan, H.-X. Sun, H. Chen, and B. Zhang, Nat. Commun. **12**, 6297 (2021).
- [25] R. El-Ganainy, K. G. Makris, D. N. Christodoulides, and Z. H. Musslimani, Opt. Lett. **32**, 2632–2634 (2007).
- [26] K. G. Makris, R. El-Ganainy, D. Christodoulides, and Z. H. Musslimani, Phys. Rev. Lett. **100**, 103904 (2008).
- [27] S. Klaiman, U. Günther, and N. Moiseyev, “Phys. Rev. Lett. **101**, 080402 (2008).
- [28] S. Longhi, Phys. Rev. Lett. **103**, 123601 (2009).
- [29] H. Schomerus, Opt. Lett. **38**, 1912–1914 (2013).
- [30] C. M. Bender, Rep. Progr. Phys. **70**, 947 (2007).
- [31] B. Zhu, R. Lü, and S. Chen, Phys. Rev. A **89**, 062102 (2014)
- [32] Z. Gong, S. Higashikawa, and M. Ueda, Phys. Rev. Lett. **118**, 200401 (2017).
- [33] C. Li, X. Z. Zhang, G. Zhang, and Z. Song, Phys. Rev. B **97**, 115436 (2018).
- [34] S. Yao and Z. Wang, Phys. Rev. Lett. **121**, 086803 (2018).
- [35] R. Fleury, D. L. Sounas, and A. Alu, Phys. Rev. Lett. **113**, 023903 (2014).
- [36] J. Luo, J. Li, and Y. Lai, Phys. Rev. X **8**, 031035 (2018).
- [37] M. Lawrence, N. Xu, X. Zhang, Cong, J. Han, W. Zhang, and S. Zhang, Phys. Rev. Lett. **113**, 093901 (2014).
- [38] D. Li, S. Huang, Y. Cheng, and Y. Li, Sci. China. Phys. Mech. Astron. **64**, 1 (2021).
- [39] X. Wang, X. Fang, D. Mao, Y. Jing, and Y. Li, Phys. Rev. Lett. **123**, 214302 (2019).

- [40] B. Orazbayev, R. Fleury, *Nanophotonics* **8**, 1443 (2019).
- [41] G. Arregui, J. Comis-Bresco, C.M. Sotomayor-Torres, P.D. Garcia, *Phys. Rev. Lett.* **126**, 027493 (2021).
- [42] M. Patterson and S. Hughes, *Phys. Rev. Lett.* **102**, 253903 (2009).
- [43] Livio, M. Why symmetry matters. *Nature* **490**, 472–473 (2012).
- [44] S. Zheng, G. Duan, and B. Xia, *Appl. Sci.* **12**, 1987 (2022).
- [45] T. Fukui, Y. Hatsugai, and H. Suzuki, *J. Phys. Soc. Jpn.* **74** (2005) 1674.
- [46] The numerical estimation of the valley Chern index was performed by integrating the Berry connection with respected to the band along a closed path around the K point.
- [47] V. M. Kulkarni, A. Gupta, and N. S. Vidhyadhiraja, *Phys. Rev. B* **106**, 075113 (2023).

## Chapter 5

- [1] A. Nastro, M. Ferrari, L. Rufer, S. Basrour, V. Ferrari, *Micromachines* **13** (1), 96 (2022).
- [2] R. Venegas, G. Núñez, C. Boutin, O. Umnova, Q. Zhang, *Physics of Fluids* **34**, 017117 (2022).



## Biography

Mr. Md. Shuzon Ali was born in 1986 in Bangladesh. He has successfully completed his M.Sc. (Thesis) in the year 2010 (Exam held in 2011) and B.Sc. (Honors) in the year 2009 (Exam held in 2010) from the dept. of Applied Mathematics, under University of Rajshahi, Rajshahi, Bangladesh. Mr. Shuzon has obtained **First class First** (CGPA-4.00 out of 4.00) in M. Sc. (Thesis) examination, and **First class Second** in B. Sc. (CGPA-3.88 out of 4.00) position in the order of merit. He received Agrani Bank Gold Medal Award and Certificate (**Faculty First in Science, M.Sc. (Thesis), 87.13%**), and A. F. Mujibur Rahman Foundation Gold Medal Award and Talent Scholarship with Certificate (**First class First in position, M. Sc. (Thesis)**) for his academic excellence. He has obtained a position of Lecturer in 2014 & been working as an assistant professor from 2016 at the dept. of Mathematics at Bangabandhu Sheikh Mujibur Rahman Science & Technology University, Gopalganj, Dhaka, Bangladesh. He awarded the Japanese Govt. Scholarship (**MEXT**), to pursue his Ph.D. degree and working as a Ph.D. research student at Okayama University, Japan since October 2020. Mr. Ali is interested in “topological photonics, and phononics, non-Hermitian physics, and quantum physics”. His Ph.D. research title is “**Design of actively controllable two-dimensional phononic waveguides based on valley topological phononic band engineering**”. He has published about 12 research papers in international journals.